

THE ROLE OF OPTICALLY THIN LIQUID CLOUDS IN THE  
2012 GREENLAND ICE SHEET SURFACE MELT EVENT

by

Kyle A. Nelson

A thesis submitted in partial fulfillment of  
the requirements for the degree of

Master of Science

(Atmospheric and Oceanic Science)

at the

UNIVERSITY OF WISCONSIN-MADISON

2014

*Approved:* \_\_\_\_\_  
Steven A. Ackerman

Professor, Department of Atmospheric & Oceanic Sciences  
Director, Cooperative Institute for Meteorological Satellite Studies

Date: \_\_\_\_\_

*Approved:* \_\_\_\_\_  
Jeffrey R. Key

Adjunct Professor, Department of Atmospheric & Oceanic Sciences  
Branch Chief, Advanced Satellite Products Branch, NOAA

Date: \_\_\_\_\_

*Approved:* \_\_\_\_\_  
Grant W. Petty

Professor and Chair, Department of Atmospheric & Oceanic Sciences

Date: \_\_\_\_\_

*Approved:* \_\_\_\_\_  
Tristan S. L'Ecuyer

Professor, Department of Atmospheric & Oceanic Sciences

Date: \_\_\_\_\_

## **Acknowledgements**

This study would not have been possible without the generous assistance, contributions and expertise of fellow scientists and colleagues. First and foremost, I would like to recognize my advisors: Jeff Key for his guidance and assistance with this research endeavor and Steve Ackerman for his guidance, advice and encouragement as my academic advisor. Thanks to Ralf Bennartz for discussions on his work and providing ICECAPS data; Andy Heidinger for discussions regarding PATMOS-x and MODIS lookup tables; Andi Walther for discussions on MODIS lookup tables; Denis Botambekov for processing of MODIS/CALIOP/IIR matchup data; SSEC PEATE Group for providing MODIS/CALIOP/IIR matchups and MODIS Collections 5 and 6; and the PATMOS-x Team for technical discussion of the PATMOS-x dataset.

A special thanks to others on my thesis committee: Tristan L'Ecuyer for review of my thesis and technical discussion of CALIPSO, CALIOP and IIR, and to Grant Petty for his comments on my thesis. Last but not least, I would like to recognize Mark Kulie for his support and encouragement throughout my graduate career and Erik Gould for discussion of the CALIOP instrument.

This work was supported by the NOAA Climate Data Records Program.

## **Abstract**

Clouds play a fundamental role in the mass budget of the world's major ice sheets both as a source, via precipitation, and as a sink, via surface melt due to radiative forcing. To understand present and future effects of changes to the world's ice sheets requires a robust understanding of the macro and microphysical properties of polar cloud systems, including their radiative effects on the surface. For this study, the Moderate Resolution Imaging Spectroradiometer (Terra-MODIS) on NASA's Terra satellite is used to diagnose the spatial extent and frequency of occurrence of optically thin, liquid clouds over the Greenland Ice Sheet (GIS). Satellite data indicated a historically rare period of extended surface melting observed across the entire Greenland ice sheet in July 2012. A 2013 study using the Integrated Characterization of Energy, Clouds, Atmospheric State and Precipitation at Summit (ICECAPS) surface instrument data at Summit, Greenland and simple radiative transfer modeling, determined that thin, low-level liquid clouds played a key role in that melt event by helping to increase surface temperatures above freezing at Summit. The analysis of satellite data presented here confirm the presence of these clouds over much of the GIS and their warming effect on the surface. Furthermore, the satellite analyses show similar geographic coverage of thin, liquid clouds in both July 2011 and July 2012, though July 2011 did not experience a large-scale surface melt. A qualitative analysis of low-level warm air advection for both years helps explain why melting occurred over such a large area in July 2012 as compared to July 2011.

## Table of Contents

<b>1. Introduction .....</b>	<b>1</b>
<b>2. Methodology and Data .....</b>	<b>7</b>
<b>2.1. Radiative Transfer Modeling .....</b>	<b>7</b>
<b>2.2. Surface Radiative Forcing .....</b>	<b>8</b>
<b>2.3. Satellite Data .....</b>	<b>9</b>
2.3.1. MOD06 Collection 5 & 6 Standard Cloud Product .....	11
2.3.2. CALIPSO: CALIOP and IIR .....	12
2.3.3. MODIS/CALIOP/IIR Matchups .....	13
2.3.4. PATMOS-x & MOD02 1.6 $\mu\text{m}$ .....	14
2.3.5. Cloud Phase Determination .....	17
<b>2.4. ECMWF ERA Interim .....</b>	<b>21</b>
<b>3. Results .....</b>	<b>22</b>
<b>3.1. Theoretical Radiative Effects of Clouds on the Surface .....</b>	<b>22</b>
<b>3.2. Cloud Characteristics over the GIS .....</b>	<b>26</b>
3.2.1. MOD06 Collection 5 & 6 Standard Cloud Product .....	26
3.2.2. MODIS/CALIOP/IIR Matchups .....	34
3.2.3. PATMOS-x & MOD02 1.6 $\mu\text{m}$ .....	39
3.2.4. Cloud Phase Determination .....	48
<b>3.3. Low Level Temperature Advection in 2011 and 2012 .....</b>	<b>56</b>
<b>4. Summary and Conclusions .....</b>	<b>65</b>
<b>5. Future Work .....</b>	<b>67</b>

**References..... 69**

## List of Figures

Figure 1: Composite maps of melt extent from OS2, SSMIS, and MODIS satellite data for (a) 8 July, (b) 12 July, (c) 22 July and (d) 29 July 2012. In the red areas, two or more of the satellites detected melt while in the orange areas, only one satellite detected melt. No melt was detected in the white areas, black indicated insufficient data, green and dark grey show land, and light grey represents ocean. (From Nghiem et al. 2012) ..... 2

Figure 2: Observed and simulated temporal evolution of the July 2012 surface melting event at Summit. (a) Temporal evolution of the temperature 2 m above the surface ( $T_{2m}$ ) for July 2012; (b) expanded view of data from (a) for the extended GIS melting period (9-15 July 2012). In the top parts of (a) and (b), the black curve shows  $T_{2m}$  observed by the NOAA meteorological (met.) tower, the red curve shows the temperature observed by the radiosondes at 500 m above ground ( $T_{500m}$ ), the green curve shows the development of  $T_{2m}$  simulated using the surface energy balance model driven by observed radiative (obs. rad.) fluxes, and the yellow curve shows the development of  $T_{2m}$  simulated using the surface energy balance model driven by simulated radiative (sim. rad.) fluxes based on water vapor path (WVP) and liquid water path (LWP). Values of these two last quantities are shown in the lower parts of (a) and (b) with separate axes: blue (red) dots show LWP (WVP) values observed by an upward looking microwave radiometer. (c) Model sensitivity studies with respect to clouds and solar radiation. Yellow line, as in (a) and (b); turquoise curve,  $T_{2m}$  without solar radiation; blue curve,  $T_{2m}$  assuming a cloud-free atmosphere (LWP of  $0 \text{ gm}^{-2}$ ); purple curve,  $T_{2m}$  assuming an atmosphere with a very thick cloud with constant LWP of

- 500  $\text{gm}^{-2}$ . Inset, simulated maximum  $T_{2m}$  and LWP at a time of  $\pm 30$  min around the time of maximum surface temperature (error bars,  $\pm 1$  s.d.). (From Bennartz et al. 2013)..... 5
- Figure 3: Google Earth plot of Greenland showing the location of Summit (blue flag) and the five gridboxes (red) used to define the GIS. The PATMOS-x land/sea mask was used to exclude water pixels from the analysis. .... 15
- Figure 4: Satellite Channel Wavelengths in Micrometers ( $\mu\text{m}$ ), and Typical Reflectance Spectra for Snow and Clouds The 1.6 micron channel is highlighted. Note the strong reflectance from clouds (black line) when compared to minimal reflectance from snow (colored lines). (From nsidc.org)..... 16
- Figure 5: 1.6 $\mu\text{m}$  optical depth versus reflectance for a liquid water cloud. Solar zenith angle 65 degrees, sensor zenith angle 15 degrees. Red line: 10  $\mu\text{m}$  particle effective radius. Green line: 6.3  $\mu\text{m}$  particle effective radius. Blue line: 3.98  $\mu\text{m}$  particle effective radius. Data provided by A. Walther and A. Heidinger..... 18
- Figure 6: 3.7 $\mu\text{m}$  optical depth versus reflectance for a liquid water cloud. Solar zenith angle 65 degrees, sensor zenith angle 15 degrees. Red line: 10  $\mu\text{m}$  particle effective radius. Green line: 6.3  $\mu\text{m}$  particle effective radius. Blue line: 3.98  $\mu\text{m}$  particle effective radius. Data provided by A. Walther and A. Heidinger..... 19
- Figure 7: 3.7 $\mu\text{m}$  optical depth versus reflectance for an arctic ice cloud. Solar zenith angle 65 degrees, sensor zenith angle 15 degrees. Red line: 39.8  $\mu\text{m}$  particle effective radius. Green line: 25.1  $\mu\text{m}$  particle effective radius. Blue line: 15.8  $\mu\text{m}$  particle effective radius. Data provided by A. Walther and A. Heidinger..... 20

Figure 8: Surface radiative forcing (SRF) ( $\text{W}/\text{m}^2$ ) versus liquid water path (LWP) ( $\text{g}/\text{m}^2$ ) and cloud optical depth for solar zenith angles 50 degrees to 75 degrees. LWP values range from 6-64  $\text{g}/\text{m}^2$  corresponding to optical depths of 1.0 – 10.0 assuming a  $10\mu\text{m}$  effective particle radius. Single layer, liquid cloud, base height 1 km over a fresh snow surface with a visible albedo set at 0.9. Green line: LW SRF. Blue line: SW SRF. Red line: net (LW + SW) SRF. “BB alb” is broadband albedo scaled by the model based on the surface type and user-defined visible albedo. .... 23

Figure 9: Surface radiative forcing (SRF) ( $\text{W}/\text{m}^2$ ) versus liquid water path (LWP) ( $\text{g}/\text{m}^2$ ) and cloud optical depth for solar zenith angles 50 degrees to 75 degrees, zoomed in to the LWP and optical depth range of interest with LWP values from 10 – 40  $\text{g}/\text{m}^2$  corresponding to optical depths of 1.5 – 6.5 assuming a  $10\mu\text{m}$  effective particle radius. Single layer, liquid cloud, base height 1 km over a fresh snow surface with a visible albedo set at 0.9. Green line: LW SRF. Blue line: SW SRF. Red line: net (LW + SW) SRF. “BB alb” is broadband albedo scaled by the model based on the surface type and user-defined visible albedo. .... 24

Figure 10: Surface radiative forcing (SRF) ( $\text{W}/\text{m}^2$ ) versus liquid water path (LWP) ( $\text{g}/\text{m}^2$ ) and cloud optical depth for cloud base heights of 0.5 km to 3.0 km. Solar zenith angle is fixed at 65 degrees. Single layer, liquid cloud, base height 1 km over a fresh snow surface with a visible albedo set at 0.9. Green line: LW SRF. Blue line: SW SRF. Red line: net (LW + SW) SRF. .... 25

Figure 11: Frequency of liquid clouds as identified by MODIS cloud phase detection algorithm in the MOD06 product. Note the lack of detection of liquid clouds on the interior of Greenland. .... 28

- Figure 12: Frequency of optically thin ( $10 - 40 \text{ g/m}^2$ ) liquid clouds as identified by the MODIS cloud phase detection algorithm and MODIS liquid water path in the MOD06 product. Note the lack of detection of these clouds away from the coastline. .... 29
- Figure 13: Distribution of MODIS cloud optical depth across the GIS for July 2012 comparing the standard and  $1.6 \mu\text{m} / 2.1 \mu\text{m}$  retrievals. Data is plotted for each pixel that was determined to be cloudy, liquid phase with solar zenith angles less than 75 degrees. .... 31
- Figure 14: Distribution of MODIS liquid water path across the GIS for July 2012 comparing the standard and  $1.6 \mu\text{m} / 2.1 \mu\text{m}$  retrievals. Data is plotted for each pixel that was determined to be cloudy, liquid phase with solar zenith angles less than 75 degrees. 32
- Figure 15: Distribution of MODIS cloud optical depth in a  $2^\circ \times 2^\circ$  grid box centered over Summit for July 2012 comparing the standard and  $1.6 \mu\text{m} / 2.1 \mu\text{m}$  retrievals. Data is plotted for all pixels regardless of cloud phase, temperature or solar zenith angle. .... 33
- Figure 16: Distribution of MODIS liquid water path in a  $2^\circ \times 2^\circ$  grid box centered over Summit for July 2012 comparing the standard and  $1.6 \mu\text{m} / 2.1 \mu\text{m}$  retrievals. Data is plotted for all pixels regardless of cloud phase, temperature or solar zenith angle. .... 34
- Figure 17: Distribution of observed liquid water path values for all July 2012 as observed by the microwave radiometer (MWR) at Summit Station. Data are binned every  $5 \text{ g/m}^2$ . The left-most bar is  $0 - 5 \text{ g/m}^2$ , the second  $5 - 10 \text{ g/m}^2$ , then  $10 - 15 \text{ g/m}^2$ , ending with the rightmost bar as  $95 - 100 \text{ g/m}^2$ . MWR data provided by R. Bennartz. .... 35

Figure 18: MODIS versus CALIOP liquid water path across the GIS for July 2012 where a pixel was determined to be cloudy, liquid phase, single-layer cloud with sensor and solar zenith angles less than 75 degrees.....	36
Figure 19: MODIS versus IIR liquid water path across the GIS for July 2012 where a pixel was determined to be cloudy, liquid phase, single-layer cloud with sensor and solar zenith angles less than 75 degrees. ....	37
Figure 20: IIR versus CALIOP liquid water path across the GIS for July 2012 where a pixel was determined to be cloudy, liquid phase, single-layer cloud with sensor and solar zenith angles less than 75 degrees. ....	38
Figure 21: Total number of cloudy days per $0.1^\circ \times 0.1^\circ$ pixel for July 2011. Cloudy days were identified as where the PATMOS-x cloud mask classified a pixel as cloudy. All clouds (liquid, ice and all thicknesses) are included.....	41
Figure 22: Total number of cloudy days per $0.1^\circ \times 0.1^\circ$ pixel for July 2012. Cloudy days were identified as where the PATMOS-x cloud mask classified a pixel as cloudy. All clouds (liquid, ice and all thicknesses) are included.....	42
Figure 23: Percentage of cloudy pixels in a $2^\circ \times 2^\circ$ grid box centered over Summit for July 2011. Cloudy pixels were identified as where the PATMOS-x cloud mask classified a pixel as cloudy. All clouds (liquid, ice and all thicknesses) are included. ....	43
Figure 24: Percentage of cloudy pixels in a $2^\circ \times 2^\circ$ grid box centered over Summit for July 2012. Cloudy pixels were identified as where the PATMOS-x cloud mask classified a pixel as cloudy. All clouds (liquid, ice and all thicknesses) are included. ....	44
Figure 25: Percentage of pixels that were identified as having thin, liquid clouds versus any cloud in a $2^\circ \times 2^\circ$ grid box centered over Summit for July 2011 .....	46

Figure 26: Percentage of pixels that were identified as having thin, liquid clouds versus any cloud in a $2^\circ \times 2^\circ$ grid box centered over Summit for July 2012. ....	47
Figure 27: Frequency of liquid pixels versus cloudy pixels for July 2011. Liquid pixels were identified as where the $3.7 \mu\text{m}$ reflectance was greater than 0.07. ....	49
Figure 28: Frequency of liquid pixels versus cloudy pixels for July 2012. liquid pixels were identified as where the $3.7 \mu\text{m}$ reflectance was greater than 0.07. ....	50
Figure 29: Frequency of liquid pixels versus cloudy pixels for July 2011. Liquid pixels were identified as where the $3.7 \mu\text{m}$ reflectance was greater than 0.07 and cloud top temperature was greater than 243 K. ....	51
Figure 30: Frequency of liquid pixels versus cloudy pixels for July 2012. Liquid pixels were identified as where the $3.7 \mu\text{m}$ reflectance was greater than 0.07 and cloud top temperature was greater than 243 K. ....	52
Figure 31: Frequency of thin liquid cloud pixels versus cloudy pixels for July 2011. Liquid pixels were identified as where the $3.7 \mu\text{m}$ reflectance was greater than 0.07 and cloud top temperature was greater than 243 K. Optically thin pixels were identified where calculated LWP was between $10\text{-}40 \text{ g/m}^2$ using an assumed $6.3 \mu\text{m}$ particle radius. ....	54
Figure 32: Frequency of thin, liquid cloudy pixels versus cloudy pixels for July 2012. Liquid pixels were identified as where the $3.7 \mu\text{m}$ reflectance was greater than 0.07 and cloud top temperature was greater than 243 K. Optically thin pixels were identified where calculated LWP was between $10\text{-}40 \text{ g/m}^2$ using an assumed $6.3 \mu\text{m}$ particle radius. ....	55

Figure 33: ECMWF reanalysis of Temperature (shaded) and Geopotential Height (blue contoured) at 1000 hPa averaged over the month of July 2011.....	57
Figure 34: ECMWF reanalysis of Temperature (shaded) and Geopotential Height (blue contoured) at 1000 hPa averaged over the month of July 2012.....	58
Figure 35: ECMWF reanalysis of Temperature (shaded) and Geopotential Height (blue contoured) at 850 hPa averaged over the month of July 2011.....	59
Figure 36: ECMWF reanalysis of Temperature (shaded) and Geopotential Height (blue contoured) at 850 hPa averaged over the month of July 2012.....	60
Figure 37: ECMWF reanalysis of the u wind component (shaded; warm colors are positive u, cool colors are negative u) at 850 hPa averaged over the month of July 2011.....	61
Figure 38: ECMWF reanalysis of the u wind component (shaded; warm colors are positive u, cool colors are negative u) at 850 hPa averaged over the month of July 2012.....	62
Figure 39: ECMWF reanalysis of the v wind component (shaded; warm colors are positive v, cool colors are negative v) at 850 hPa averaged over the month of July 2011.....	63
Figure 40: ECMWF reanalysis of the v wind component (shaded; warm colors are positive v, cool colors are negative v) at 850 hPa averaged over the month of July 2012.....	64

## List of Abbreviations and Acronyms

AIRS	Atmospheric Infrared Sounder
AOS	Department of Atmospheric and Oceanic Sciences at UW-Madison
AVHRR	Advanced Very High Resolution Radiometer
CALIOP	Cloud-Aerosol Lidar with Orthogonal Polarization
CALIPSO	Cloud-Aerosol Lidar and Infrared Pathfinder Satellite Observations
CIMSS	Cooperative Institute for Meteorological Satellite Studies
ECMWF	European Centre for Medium Range Weather Forecasting
GIS	Greenland Ice Sheet
GOES	Geostationary Satellite
IASI	Infrared Atmospheric Sounding Interferometer
ICECAPS	Integrated Characterization of Energy, Clouds, Atmospheric State and Precipitation at Summit
IIR	Imaging Infrared Radiometer
LUT	Look Up Table
LW	Longwave
MODIS	Moderate Resolution Imaging Spectroradiometer
NCDC	National Climatic Data Center
NOAA	National Oceanic and Atmospheric Administration
NPOESS	National Polar-orbiting Operational Environmental Satellite System
NPP	NPOESS Preparatory Project
PATMOS-x	Pathfinder Atmospheres – Extended
PEATE	Product Evaluation and Algorithm Test Elements
SSEC	Space Science and Engineering Center
SRF	Surface Radiative Forcing
SW	Shortwave
UW-Madison	University of Wisconsin-Madison

## 1. Introduction

Clouds have a radiative warming effect on the surface most of the year in the Arctic north of 60°N (Intrieri et al. 2002; Schweiger and Key 1994; Stone 1997). In the summer, clouds warm the Arctic surface only over Greenland and the western part of the central Arctic (Wang and Key 2005). Over the Arctic as a whole, the strongest downwelling shortwave radiation at the surface occurs in June, while the largest downwelling and upwelling longwave radiation, as well as net all-wave radiation, occurs during the month of July (Wang and Key 2005). The effect of clouds on the surface radiation budget depends on several factors, namely the balance between shortwave and longwave budgets affected by the clouds. Cloud forcing is also influenced by surface conditions such as surface albedo and surface type, and by the vertical distribution of temperature and humidity (Wang and Key 2005).

Observations over the past decade reveal that liquid water clouds have the greatest radiative influence on the surface radiation budget in the Arctic (Meier et al., 2014), which controls in part the growth and melt of sea ice (Curry et al. 1996). However, global climate models tend to under-predict the formation of optically thin liquid clouds at super-cooled temperatures (Cesasa et al. 2012) which bias the Arctic surface energy balance predictions and may limit the ability of the models to accurately predict cloud feedback and response to Arctic climate change.

In July 2012, a new record for surface melt extent was set, with melting observed across almost the entire Greenland Ice Sheet (GIS) (Buis, A. & Cole, S. 2012, Nghiem, S. V. et al. 2012). Figure 1 shows the evolution and extent of surface melting in July 2012. This

melt episode raised questions about the frequency and spatial extent of such events. Bennartz et al. (2013) and Neff et al. (2014) suggest that in July 2012, advection of warm moist air at low levels over the ice sheet contributed to the melting. However, the surface melt observed at Summit cannot be attributed to only warm air advection, because surface temperature over the GIS is a product of radiative and turbulent heat fluxes (Bintanja, R. & van den Broeke, M. 1996) that are influenced by cloud and atmospheric properties. Shupe et al. (2013) states that an examination of surface cloud radiative forcing is necessary “to determine the extent to which clouds are a net source of heat to the surface.”

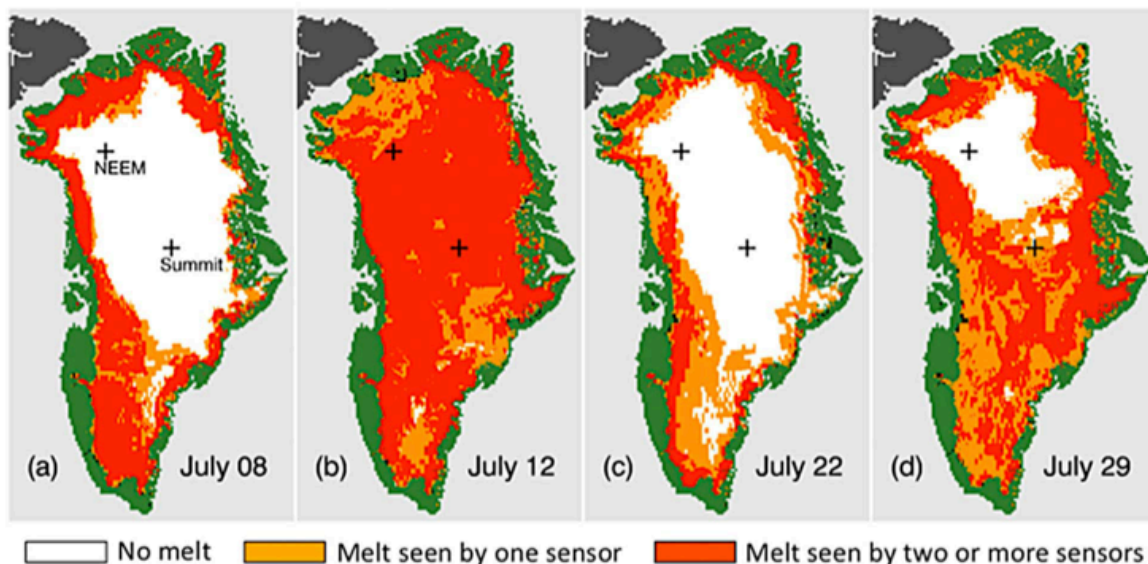


Figure 1: Composite maps of melt extent from OS2, SSMIS, and MODIS satellite data for (a) 8 July, (b) 12 July, (c) 22 July and (d) 29 July 2012. In the red areas, two or more of the satellites detected melt while in the orange areas, only one satellite detected melt. No melt was detected in the white areas, black indicated insufficient data, green and dark grey show land, and light grey represents ocean. (From Nghiem et al. 2012)

Bennartz et al. (2013) showed that low-level, optically-thin, liquid water clouds played a key role in the extended surface melting of the central GIS in July 2012. From a suite of surface instrumentation and observations from scientists at Summit Station (72.596N, 38.422W), a brief melting period was observed on 11 July 2012. Data from surface temperature instruments at Summit and model output from that study are shown in Figure 2. In Figure 2b, the black line shows the rise in observed 2 m temperature at Summit, going over 0° C on July 11. Figure 2c shows results of simulations by Bennartz et al. (2013) of 2 m air temperature under several conditions: an extremely thick cloud (LWP = 500 g/m<sup>2</sup>) and no cloud (LWP = 0 g/m<sup>2</sup>). In the cloud-free case, a strong diurnal cycle is evident but surface temperatures do not rise above -4° C. For the optically thick cloud, surface temperature does not exceed a value of -3° C.

Neither of these cases resulted in the modeled surface temperature rising above 0° C. The no cloud case shows that solar radiation alone was not sufficient and the thick cloud case shows that longwave radiation alone was also insufficient in warming the surface temperature above melting. The surface energy modeling results from Bennartz et al. (2013) indicate that surface temperatures above 0° C only occur for LWP values between 10 and 40 g/m<sup>2</sup> (Fig. 2c inset). Within this range, the liquid water cloud is optically thick enough to enhance the downwelling longwave radiation at the surface but still sufficiently optically thin to allow enough solar radiation to reach the surface. Thus, we must have a thin cloud with intermediate LWP values so that the longwave and shortwave radiative effects can combine help to warm the surface above 0° C (Bennartz et al. 2013).

The findings by Bennartz et al. (2013) are valid for a single point at Summit, Greenland, yet melting was observed over nearly the entire GIS. Are the findings at Summit

applicable in explaining melt on broader scale over entire GIS? Here it is demonstrated that optically thin liquid clouds, regardless of cloud base height, played a key role in this melt event by increasing surface temperatures not only at Summit but over the entire Greenland Ice Sheet (GIS). Additionally it is shown that for clouds in the lower troposphere, cloud base height plays a negligible role in modifying the magnitude of surface cloud radiative forcing.

This is accomplished using several methods including: analysis from a radiative transfer model to examine sensitivity of the surface radiation budget to various cloud properties; remote sensing data from several satellite platforms and instruments to estimate cloud properties over the entire GIS; and model reanalysis products to assess the large scale atmospheric circulation in the proximity of the GIS for July 2011 and July 2012. We extend the work of Bennartz et al. (2013) by expanding the study domain from a surface point observation at Summit to the entirety of Greenland by leveraging this data.

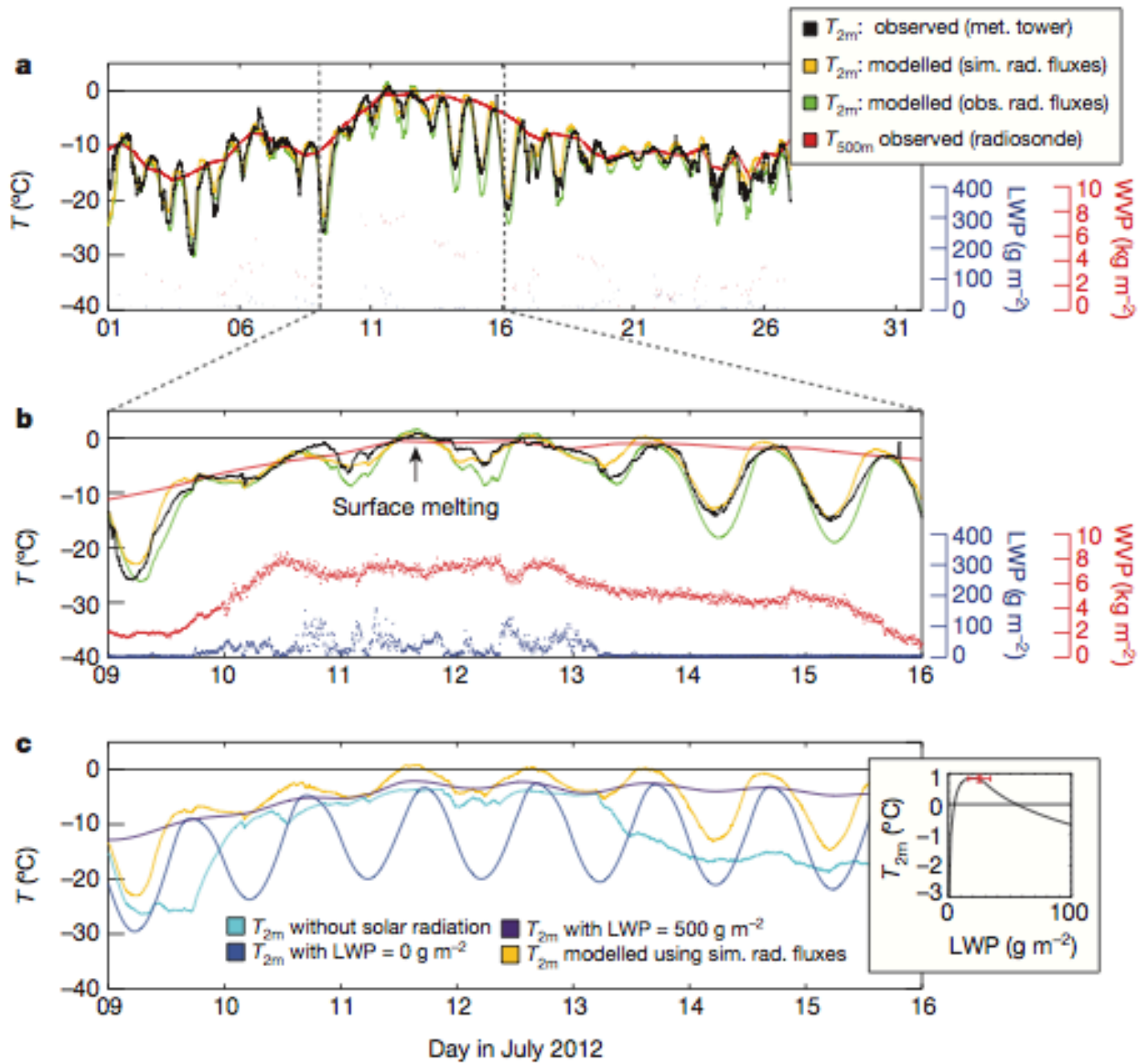


Figure 2: Observed and simulated temporal evolution of the July 2012 surface melting event at Summit. (a) Temporal evolution of the temperature 2 m above the surface ( $T_{2m}$ ) for July 2012; (b) expanded view of data from (a) for the extended GIS melting period (9-15 July 2012). In the top parts of (a) and (b), the black curve shows  $T_{2m}$  observed by the NOAA meteorological (met.) tower, the red curve shows the temperature observed by the radiosondes at 500 m above ground ( $T_{500m}$ ), the green curve shows the development of  $T_{2m}$  simulated using the surface energy balance model driven by observed radiative (obs. rad.) fluxes, and the yellow curve shows the development of  $T_{2m}$  simulated

using the surface energy balance model driven by simulated radiative (sim. rad.) fluxes based on water vapor path (WVP) and liquid water path (LWP). Values of these two last quantities are shown in the lower parts of (a) and (b) with separate axes: blue (red) dots show LWP (WVP) values observed by an upward looking microwave radiometer. (c) Model sensitivity studies with respect to clouds and solar radiation. Yellow line, as in (a) and (b); turquoise curve,  $T_{2m}$  without solar radiation; blue curve,  $T_{2m}$  assuming a cloud-free atmosphere (LWP of  $0 \text{ gm}^{-2}$ ); purple curve,  $T_{2m}$  assuming an atmosphere with a very thick cloud with constant LWP of  $500 \text{ gm}^{-2}$ . Inset, simulated maximum  $T_{2m}$  and LWP at a time of  $\pm 30$  min around the time of maximum surface temperature (error bars,  $\pm 1$  s.d.). (From Bennartz et al. 2013)

## 2. Methodology and Data

### 2.1. Radiative Transfer Modeling

A radiative transfer model was used to calculate, theoretically, the radiative effect of various types of clouds on the surface energy budget and temperature. This was done to determine the range of liquid cloud optical thicknesses over which a positive surface radiative forcing should occur. Input values for model cloud properties were taken from an analysis of in-situ surface data from Summit provided by R. Bennartz (pers. comm.). The radiative transfer model Streamer (Key and Schweiger 1998) was used to compute shortwave, longwave and broadband fluxes, and surface radiative forcing for a theoretical polar atmosphere.

Streamer calculates both intensities and fluxes for a wide variety of atmospheric and surface conditions. Upwelling and downwelling, shortwave, longwave and net fluxes, and heating rates can be computed over 24 shortwave and 105 longwave bands. Surface type, broadband albedo, cloud base height, total column water vapor were specified. A cloud was introduced as a perturbation to the clear sky profile. Standard ozone and carbon dioxide profiles for the Arctic were used in the computation. The height of the liquid cloud was varied from 0.5km to 3km, across zenith angles from 50-80 degrees to determine what effect, if any, the cloud base height had on surface radiative forcing. Surface radiative forcing is defined as the change in radiative flux at the surface that results from making a particular change to the atmosphere, in this case, introducing a cloud.

To test this approach, verification was performed using in-situ surface data from Summit. The coordinates for Summit station (72.596N, 38.422W) and date (July 12, 2012)

were input into the model for accurate determination of solar zenith angle. The solar zenith angle at Summit for July 2012 ranges from about 85° at local midnight and around 52° at local noon. The surface albedo in each spectral band was based on the internal database for each surface type in the scene. The surface type specified was fresh snow with an assumed visible albedo of 0.9, which was scaled to a broadband albedo based on surface type. The atmospheric profile was taken to be arctic summer. The cloud water concentration is set to 0.2 g/m<sup>3</sup> and cloud effective radius is set to 10 microns. Next, the Streamer model is run using the cloud and atmospheric parameters specified in the input file and calculations are performed to determine surface radiative forcing. Data is plotted for optical depths of 1.5-6.5, corresponding to a 10 - 40 g/m<sup>2</sup> liquid water path assuming a 10 micron particle radius and liquid water density of 1000 kg/m<sup>3</sup> using the equation

$$\tau^* \approx \frac{3L}{2\rho_l r}$$

where L is the liquid water path,  $\rho_l$  is the density of liquid water and r is the cloud droplet radius. This is done across all 129 bands. The 10 - 40 g/m<sup>2</sup> liquid water path range was identified by Bennartz et al. 2013 to have a positive radiative effect.

## 2.2. Surface Radiative Forcing

Clouds affect the surface energy budget by modifying the amount of downwelling shortwave and longwave radiation incident on the surface. The cloud radiative effect, or “forcing”, is the net radiation flux difference between the cloudy and clear conditions. More specifically, cloud forcing is the integrated partial derivative of the radiative flux with respect to the cloud fraction and is defined as

$$\begin{aligned}
F_{SW,net} &= F_{SW}^{\downarrow} - F_{SW}^{\uparrow} \\
F_{LW,net} &= F_{LW}^{\downarrow} - F_{LW}^{\uparrow} \\
F_{net} &= F_{SW,net} + F_{LW,net} \\
C_{SW} &= \int_0^{A_c} \frac{\partial F_{SW,net}}{\partial a} da \\
C_{LW} &= \int_0^{A_c} \frac{\partial F_{LW,net}}{\partial a} da \\
C_{net} &= C_{SW} + C_{LW}
\end{aligned}$$

where  $C_{SW}$ ,  $C_{LW}$  and  $C_{NET}$  are the shortwave, longwave, and net cloud forcing for the surface,  $F_{SW,net}$  and  $F_{LW,net}$  are the net shortwave and longwave fluxes at the surface,  $A_c$  is the total cloud amount and  $a$  is the cloud fraction (modified from Liu and Key (2014), and Shupe and Intrieri (2004)). Cloud forcing is defined as negative for surface cooling and positive for surface warming. The net cloud forcing is the sum of shortwave and longwave cloud forcing.

### 2.3. Satellite Data

Cloud properties were initially studied using standard data products from the Moderate Resolution Imaging Spectroradiometer (MODIS) onboard the NASA Aqua satellite and both the Cloud-Aerosol Lidar with Orthogonal Polarization (CALIOP) & Imaging Infrared Radiometer (IIR) onboard the Cloud-Aerosol Lidar and Infrared Pathfinder Satellite Observations (CALIPSO) satellite. Terra-MODIS was also employed.

The MOD06 standard cloud product (Platnick et al. 2003) from MODIS Collections 5 and 6 were obtained from the Atmospheric Product Evaluation and Algorithm Test Elements (PEATE) (peate.ssec.wisc.edu). MODIS cloud optical depth retrievals from Collections 5 and 6 were compared against one another and a cross-instrument comparison of cloud optical

depth was also conducted using MODIS/CALIOP/IIR matchup files provided by the PEATE. The 1.6  $\mu\text{m}$  and 3.7  $\mu\text{m}$  reflectance data from the Terra satellite were obtained from the PEATE. Look up tables (LUTs) for converting 1.6  $\mu\text{m}$  reflectance to optical depth were provided by Andy Heidinger and Andi Walther (A. Heidinger and A. Walther, pers. comm).

LUTs are created using radiative transfer calculations of reflectances at various wavelengths for a specific phase cloud with different cloud properties including cloud particle effective radius, sensor zenith angle and solar zenith angle, which are combined to estimate optical depth as function of reflectance. This method is only reliable if it provides an unambiguous retrieval (Key 2002), where only one value of optical depth corresponds to a given reflectance value, such as shown in Figure 5 where optical depth increases continuously with increasing reflectance values.

The Atmosphere PEATE at SSEC supports the NPOESS Preparatory Project (NPP) Science Team's evaluation of data quality by providing multiyear comparisons for quantitative product validation with spaceborne and ground-based data sources including MODIS, AIRS, and IASI, and validation data from ground-based, aircraft, and satellite sources including CALIPSO and CloudSat.

MODIS measures radiances at 36 wavelengths, including infrared and solar bands, with spatial resolutions of 250 m to 1 km. Such a robust set of measurements provides the potential for improved cloud detection in the Arctic (Ackerman et al. 1998, 2008; Frey et al. 2008). NASA's Terra satellite was used for 1.6  $\mu\text{m}$  retrievals due to the 1.6  $\mu\text{m}$  channel on Aqua MODIS failing shortly after launch.

### **2.3.1. MOD06 Collection 5 & 6 Standard Cloud Product**

The MODIS Level 2 Cloud Product (MOD06) combines infrared, near-infrared and visible channels to estimate both microphysical and radiative cloud properties: cloud-particle phase (ice versus water), effective cloud-particle radius, cloud optical thickness, cloud-top temperature, height, effective emissivity and cloud fraction.

MOD06 data from MODIS Collection-5 and Collection-6 were compared. Collection-6 is the latest reprocessing of the MODIS data record that was released in late 2012 (Baum et al. 2012). The focus for Collection-6 was on calibration improvements and on cloud macrophysical properties including cloud-top pressure–temperature–height and cloud thermodynamic phase (Baum et al. 2012). Cloud phase is based entirely on infrared band measurements. New data fields are contained in Collection-6, including cloud-top height and a flag for clouds near the tropopause. Spatial resolution of cloud-top macrophysical parameters is also improved. Such parameters in Collection-5 were only provided at 5 km resolution where in Collection-6 they are available at 1 km spatial resolution.

While improvements to MODIS cloud detection have been made (Liu et al. 2004; Frey et al. 2008), there are still larger errors in nighttime Arctic cloud detection than for most other regions on Earth (Ackerman et al. 2008; Holz et al. 2008). Nighttime observations of cloud properties from MODIS require the use of infrared channels, which prove problematic in the Arctic as optically thin liquid clouds are often nearly the same temperature as the underlying snow or ice surface. Because the default cloud properties such as cloud optical depth are obtained using a two-channel visible retrieval reliant upon contrasts in brightness temperature between the cloud and the underlying surface, an alternative retrieval method

was necessary. To overcome this issue, raw  $1.6\mu\text{m}$  reflectances were used in conjunction with a look up table (LUT).

### **2.3.2. CALIPSO: CALIOP and IIR**

The Cloud-Aerosol Lidar and Infrared Pathfinder Satellite Observations (CALIPSO) satellite was launched April 28, 2006 as the first dual-polarization lidar in orbit and the first satellite designed to provide long-term continuous measurements (Winker et al. 2010). CALIPSO is part of NASA's A-Train or afternoon constellation of satellites that follow each other along the same orbital track, crossing the equator around 1:30pm local time. CALIPSO combines an active lidar instrument, CALIOP (Cloud-Aerosol Lidar with Orthogonal Polarization), with passive infrared and visible imagers to diagnose the vertical structure and properties of thin clouds and aerosols over the globe. The CALIPSO mission provided the first multiyear global dataset of lidar aerosol and cloud profiles. CALIOP is a two-wavelength polarization-sensitive lidar that provides information on the vertical distributions of clouds and aerosols and their properties.

Lidar is an active remote sensing technique that involves transmitting pulses of laser light and measuring the time of the backscattered pulse return. The time it takes for each pulse to return back to the sensor is processed to calculate the distances between and properties of various surfaces present on or above the ground. Lidar uses ultraviolet, near-infrared and visible wavelengths depending on the application. While most lidars are operated as ground-based systems, in recent years, airborne and space-borne platforms have become increasingly popular. Atmospheric applications of lidar include monitoring and studying aerosol and cloud properties at high resolution to diagnose the vertical distribution

and composition of cloud and aerosol layers. Active remote sensors are in some ways superior to passive remote sensors as they can retrieve aerosol and cloud properties in situations where passive sensors cannot, such as over snow and within multilayered cloud systems provided the layers are sufficiently optically thin. Space and airborne lidar platforms have also made it possible to create digital elevation maps of earth's surface and bathymetry of bodies of water.

CALIOP produces several high-resolution data products including both Level-1 and Level-2 data at vertical resolutions of 30 m with 335 m ground-spot spacing. Level-2 products include aerosol and cloud feature masks, aerosol subtype and optical properties such as extinction and optical depth. CALIOP signals, while high in vertical resolution, are not ideal for observing all types of cloud. For example, CALIOP saturates at an optical depth of around 3 for thin cirrus clouds (Hu et al. 2010) and around 4 to 5 for liquid clouds (Josset et al. 2012), which prevents CALIOP from being able to observe the full range of optical depths in this study.

The IIR instrument is a 3 channel imaging radiometer in the thermal infrared with channels at 8.65  $\mu\text{m}$ , 10.6  $\mu\text{m}$  and 12.05  $\mu\text{m}$ . When IIR measurements are combined with the lidar information, it enables the retrieval of the size of ice particles in semi-transparent clouds. The pairing of 10.6  $\mu\text{m}$  and 12.05  $\mu\text{m}$  channels is sensitive to small particles, while the 8.65  $\mu\text{m}$  and 12.05  $\mu\text{m}$  channels are more sensitive to large particles (Josset et al. 2012).

### **2.3.3. MODIS/CALIOP/IIR Matchups**

To overcome the sparseness of useable data from the MOD06 cloud product over the GIS, the SSEC Atmospheric PEATE provided matchups of CALIPSO and MODIS data, and

using CALIPSO cloud phase flags to screen and possibly supplement the MODIS data over the center of the GIS. The matchup data are geolocation and time matched as Aqua MODIS, CALIOP and IIR are in NASA's A-Train, the group of polar orbiting satellites with a local afternoon equator crossing time of 1:30pm. Being in the same orbit allows overlap in the ground tracks and very little time delay of the ground swaths for each satellite.

CALIOP, an active sensor, does not rely solely on reflected solar or emitted thermal radiation from the clouds and GIS surface. Its superior vertical resolution compared to MODIS or IIR enables a better determination of cloud base and cloud top height for the more optically thin clouds with optical depths of 4 – 5 or less.

The matchup process involves geolocating and overlaying the ground swaths from each instrument, in this case: MODIS, CALIOP and IIR sensors. The swaths and the respective data for each sensor are then remapped to a common grid that readily allows for comparison of data from all three instruments.

#### **2.3.4. PATMOS-x & MOD02 1.6 $\mu\text{m}$**

Early retrievals of cloud properties were plagued by deficiencies in the standard MODIS cloud products (MOD06) phase and optical depth, both of which use two visible channels for the retrieval. This proved to be problematic over the highly reflective surface of the GIS. To overcome these challenges, the PATMOS-X product (Heidinger et al. 2013) was utilized. PATMOS-X was superior to raw MODIS swath data for several reasons: data is processed to a  $0.1^\circ \times 0.1^\circ$  grid for ease of analysis and statistical calculations; all data fields can be readily compared between common days and grid points; the observation closest to nadir is used for each grid box providing one best retrieval per grid box, per day; and pre-

gridded data drastically reduced processing time. Figure 3 shows the location of Summit and the outline of the five grid boxes used to define Greenland. The PATMOS-x land/sea mask was used to exclude water pixels from the analysis.

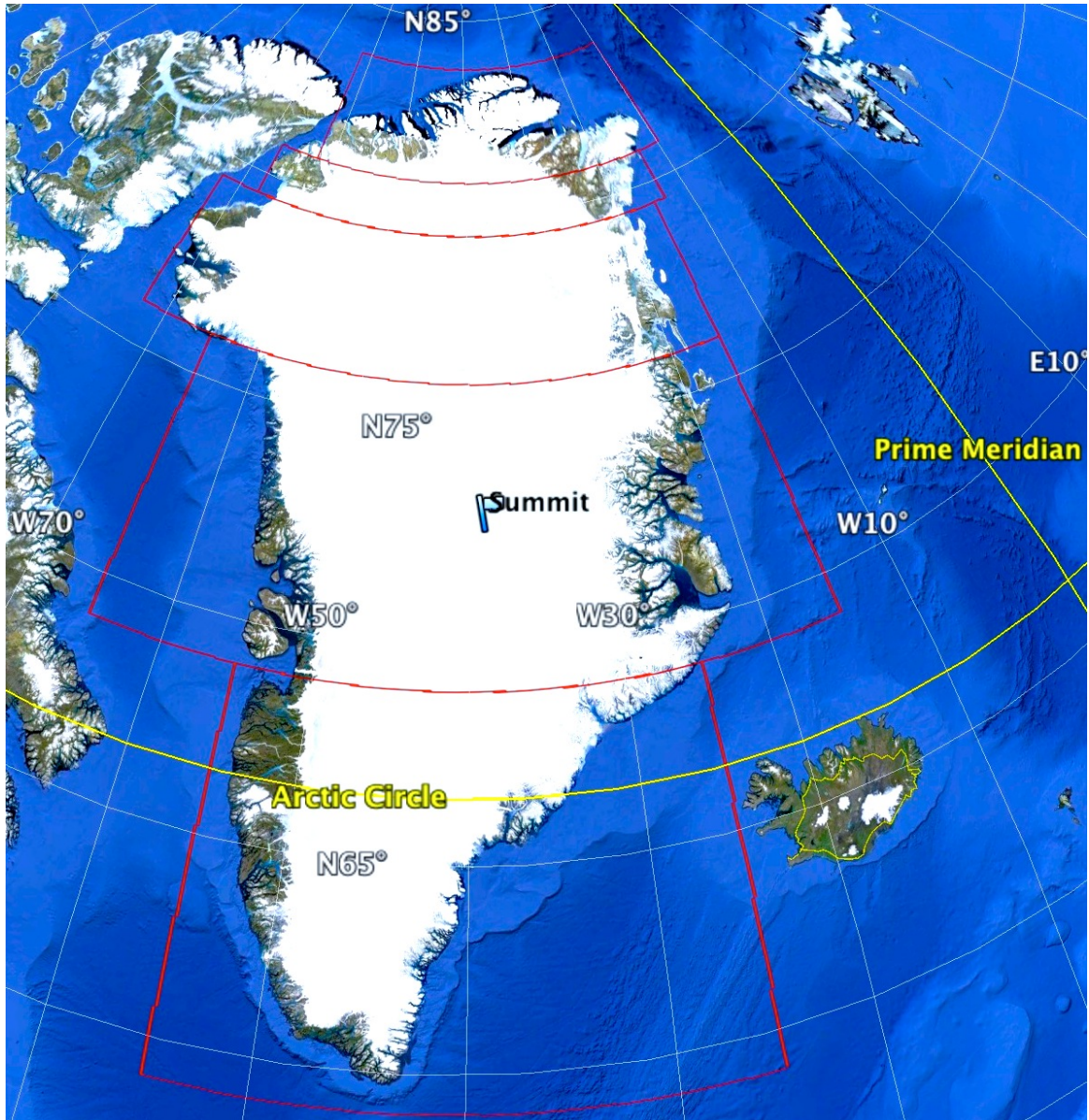


Figure 3: Google Earth plot of Greenland showing the location of Summit (blue flag) and the five gridboxes (red) used to define the GIS. The PATMOS-x land/sea mask was used to exclude water pixels from the analysis.

The optical depth retrievals were performed using raw 1.6  $\mu\text{m}$  reflectance and a corresponding Look Up Table based on radiative transfer calculations (provided by A. Heidinger and A. Walther, CIMSS). At 1.6  $\mu\text{m}$ , snow has a minimal amount of reflectance while clouds appear very bright (Figure 4), producing a strong contrast between the clouds and underlying snow/ice necessary for an accurate retrieval.

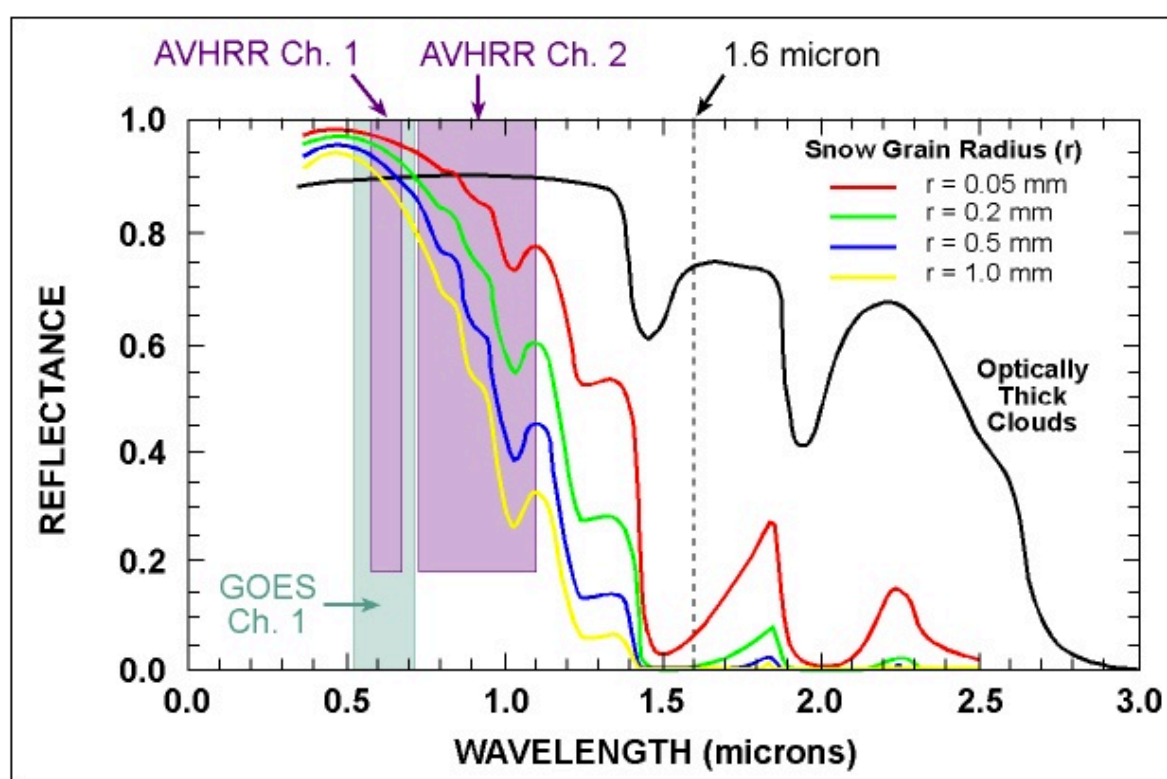


Figure 4: Satellite Channel Wavelengths in Micrometers ( $\mu\text{m}$ ), and Typical Reflectance Spectra for Snow and Clouds The 1.6 micron channel is highlighted. Note the strong reflectance from clouds (black line) when compared to minimal reflectance from snow (colored lines). (From nsidc.org)

An assumption of a 6.3  $\mu\text{m}$  particle radius was made for use with the LUT. This value is within the typical range for Arctic liquid clouds (Curry et al. 1996). Figure 5 shows a range

of optical depths and corresponding reflectances for three different cloud effective radii at 1.6  $\mu\text{m}$  using the LUT.

### **2.3.5. Cloud Phase Determination**

Given the large uncertainty in cloud particle phase in the standard MOD06 product, the MOD02 3.7  $\mu\text{m}$  reflectance was chosen as a proxy for cloud phase. This is similar to the method used by Key and Intrieri (2000) and Pavolonis and Key (2003) for determining cloud phase with AVHRR. The choice of threshold for 3.7  $\mu\text{m}$  reflectance ( $>0.07$ ) was compared with cloud top temperature ( $>243$  K) and showed good correlation in being to discriminate between ice and liquid water clouds. Figure 6 shows a range of optical depths and corresponding reflectances for three different cloud effective radii typical of arctic liquid clouds at 3.7  $\mu\text{m}$  using the LUT. Figure 7 shows a range of optical depths and corresponding reflectances for three different cloud effective radii typical of arctic ice clouds at 3.7  $\mu\text{m}$  using the LUT.

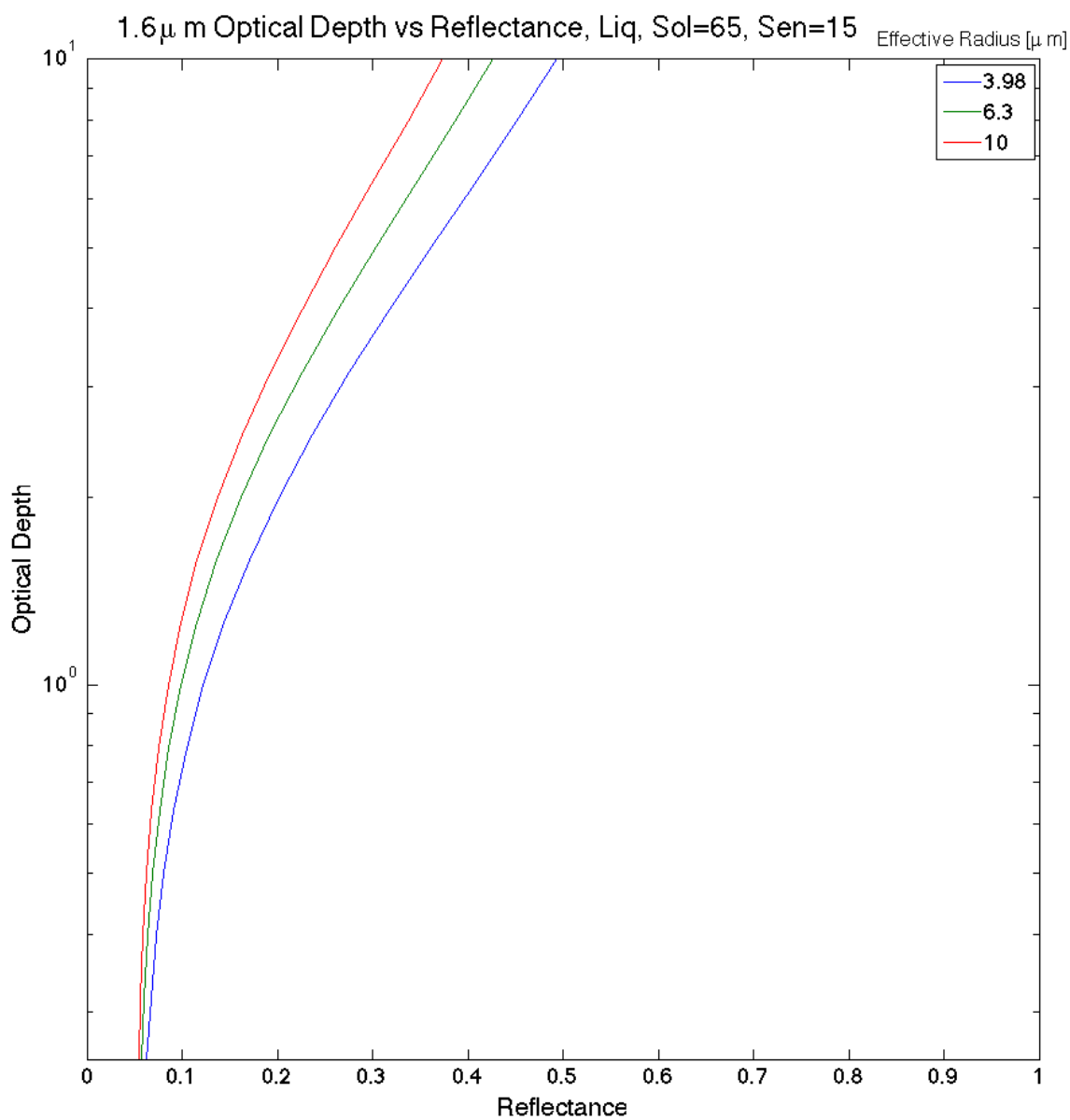


Figure 5: 1.6  $\mu$  m optical depth versus reflectance for a liquid water cloud. Solar zenith angle 65 degrees, sensor zenith angle 15 degrees. Red line: 10  $\mu$  m particle effective radius. Green line: 6.3  $\mu$  m particle effective radius. Blue line: 3.98  $\mu$  m particle effective radius. Data provided by A. Walther and A. Heidinger.

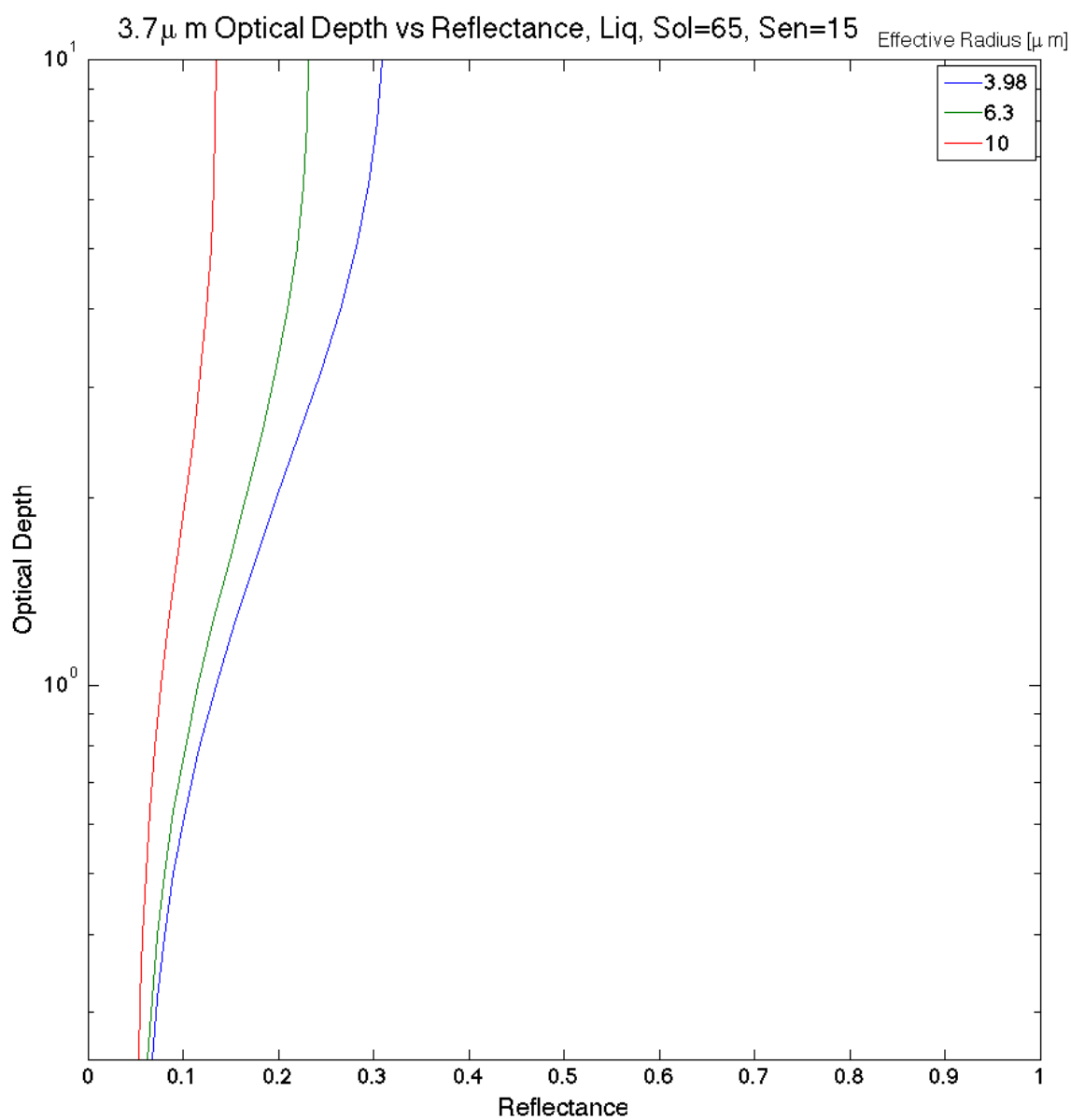


Figure 6: 3.7 $\mu$ m optical depth versus reflectance for a liquid water cloud. Solar zenith angle 65 degrees, sensor zenith angle 15 degrees. Red line: 10  $\mu$ m particle effective radius. Green line: 6.3  $\mu$ m particle effective radius. Blue line: 3.98  $\mu$ m particle effective radius. Data provided by A. Walther and A. Heidinger.

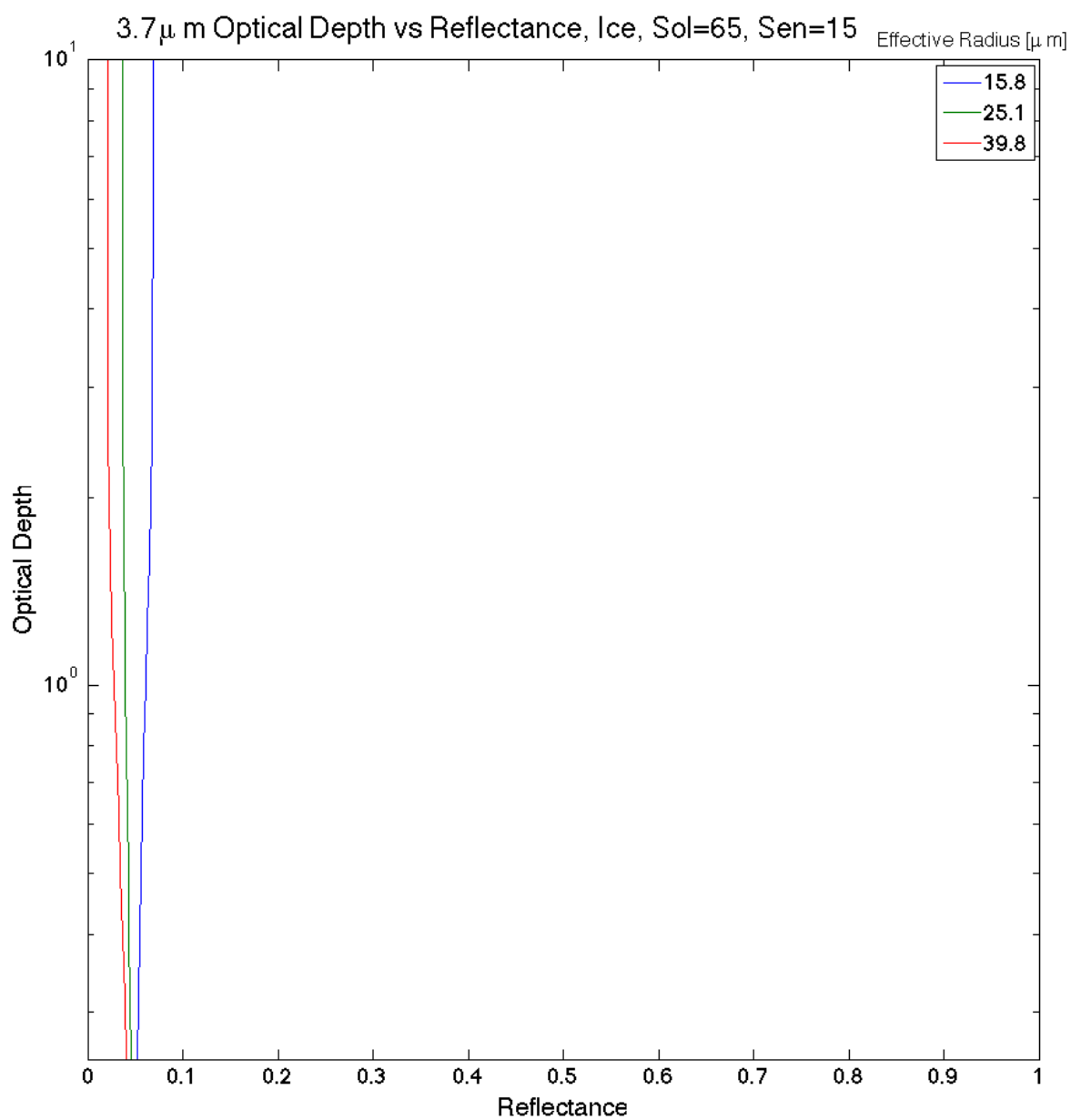


Figure 7: 3.7  $\mu$  m optical depth versus reflectance for an arctic ice cloud. Solar zenith angle 65 degrees, sensor zenith angle 15 degrees. Red line: 39.8  $\mu$  m particle effective radius. Green line: 25.1  $\mu$  m particle effective radius. Blue line: 15.8  $\mu$  m particle effective radius. Data provided by A. Walther and A. Heidinger.

## 2.4. ECMWF ERA Interim

The European Centre for Medium-Range Weather Forecasts (ECMWF) ERA-Interim data was employed to assess the general atmospheric circulation and temperature advection in the proximity of the GIS. ERA-Interim is the latest reanalysis of the global atmosphere produced by the ECMWF, covering the period from January 1979 onward and continuing forward in near-real time (Berrisford et al. 2009, Simmons et al. 2014). The ERA-Interim has a spatial resolution of  $0.7^\circ \times 0.7^\circ$  and 60 atmospheric layers. With an improved reanalysis system, performance of ERA-INTERIM has improved significantly when compared to previous reanalysis data sets such as the ERA-40 and ERA-15 (ECMWF 2007; Dee et al. 2011). Geopotential height, temperature, u-wind and v-wind were plotted at 850 hpa and 1000 hpa to qualitatively evaluate the magnitude and location of low-level temperature advection. Synoptic monthly means for each variable were plotted for July 2011 and 2012 using the ECMWF ERA-Interim web interface ([http://data-portal.ecmwf.int/data/d/interim\\_full\\_mnth/levtype=pl/](http://data-portal.ecmwf.int/data/d/interim_full_mnth/levtype=pl/)).

### 3. Results

#### 3.1. Theoretical Radiative Effects of Clouds on the Surface

Sensitivity studies were performed using the robust radiative transfer model Streamer, which demonstrated that cloud liquid water path values of 10 - 40 g/m<sup>2</sup>, observed by Bennartz, corresponding to a cloud optical thickness between 1.5 and 6.5, produce a positive surface radiative forcing for the range of typical solar zenith angles during the July 2012 melt event (Figures 8 and 9).

Model simulations also show that varying the base height of optically thin liquid clouds has a negligible effect on the magnitude of surface radiative forcing (Figure 10). This allows for the removal of the “low-level” constraint in our study.

Results show that a positive surface radiative forcing occurs over the highly reflective surface of Greenland for optically thin liquid clouds over all solar zenith angles present during the month of July and for cloud base heights from 0.5 km to 3 km. Conversely, over a very low albedo surface such as the Arctic Ocean, clouds warm the surface during winter and cool the surface in mid-summer (Stone 1997).

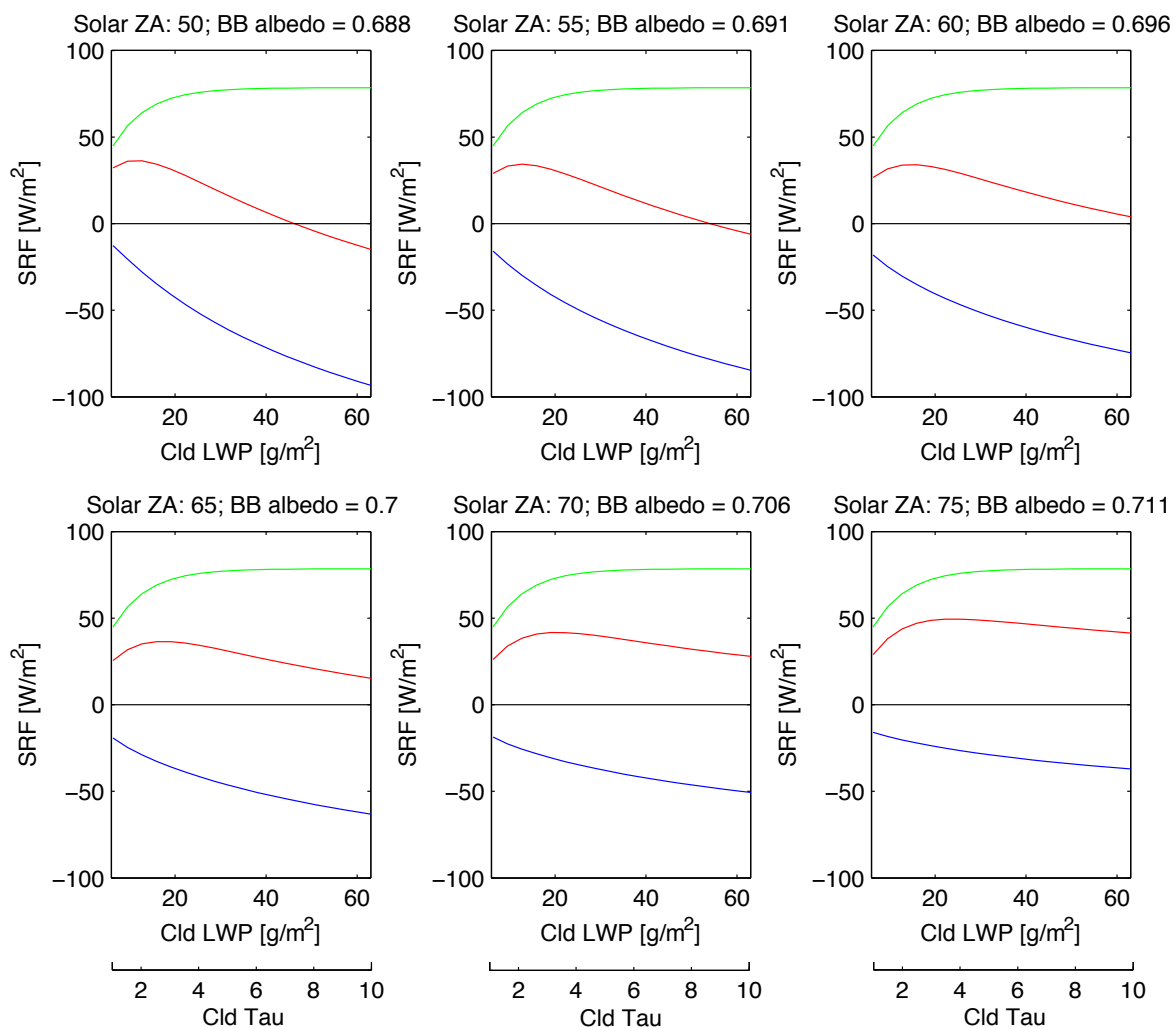


Figure 8: Surface radiative forcing (SRF) ( $\text{W/m}^2$ ) versus liquid water path (LWP) ( $\text{g/m}^2$ ) and cloud optical depth for solar zenith angles 50 degrees to 75 degrees. LWP values range from 6-64  $\text{g/m}^2$  corresponding to optical depths of 1.0 – 10.0 assuming a  $10\mu\text{m}$  effective particle radius. Single layer, liquid cloud, base height 1 km over a fresh snow surface with a visible albedo set at 0.9. Green line: LW SRF. Blue line: SW SRF. Red line: net (LW + SW) SRF. “BB alb” is broadband albedo scaled by the model based on the surface type and user-defined visible albedo.

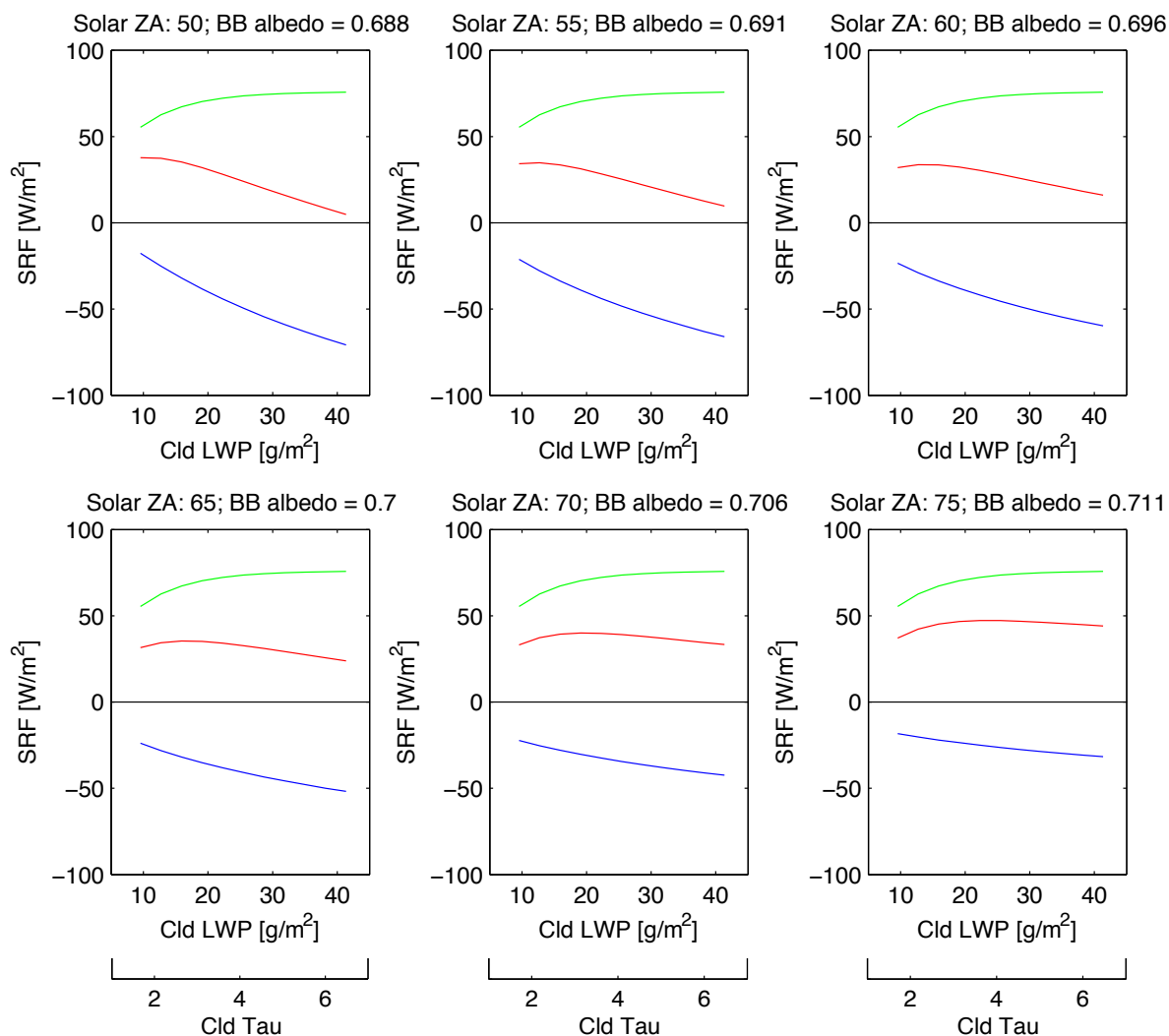


Figure 9: Surface radiative forcing (SRF) ( $W/m^2$ ) versus liquid water path (LWP) ( $g/m^2$ ) and cloud optical depth for solar zenith angles 50 degrees to 75 degrees, zoomed in to the LWP and optical depth range of interest with LWP values from 10 – 40  $g/m^2$  corresponding to optical depths of 1.5 – 6.5 assuming a  $10\mu m$  effective particle radius. Single layer, liquid cloud, base height 1 km over a fresh snow surface with a visible albedo set at 0.9. Green line: LW SRF. Blue line: SW SRF. Red line: net (LW + SW) SRF. “BB alb” is broadband albedo scaled by the model based on the surface type and user-defined visible albedo.

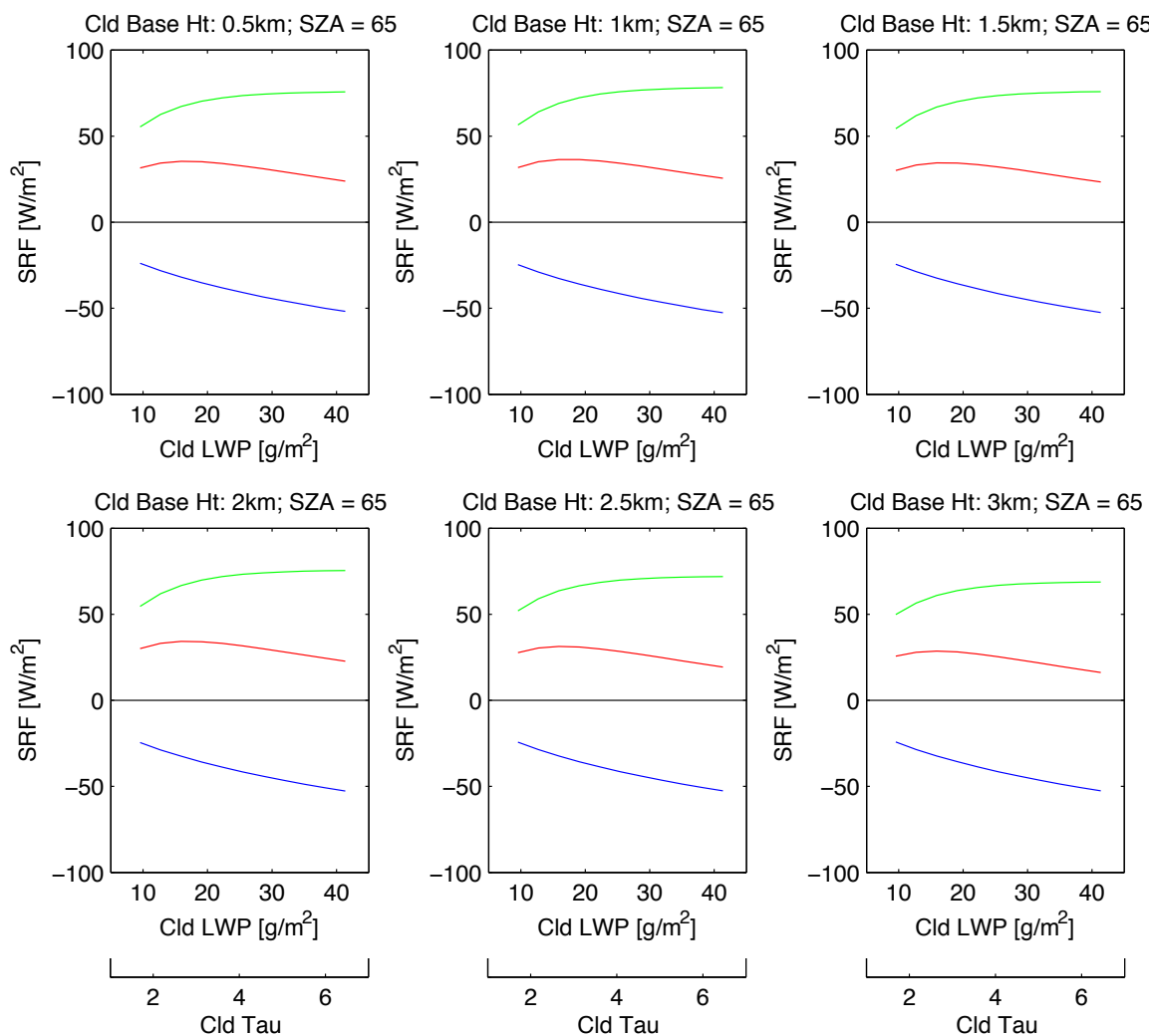


Figure 10: Surface radiative forcing (SRF) ( $\text{W/m}^2$ ) versus liquid water path (LWP) ( $\text{g/m}^2$ ) and cloud optical depth for cloud base heights of 0.5 km to 3.0 km. Solar zenith angle is fixed at 65 degrees. Single layer, liquid cloud, base height 1 km over a fresh snow surface with a visible albedo set at 0.9. Green line: LW SRF. Blue line: SW SRF. Red line: net (LW + SW) SRF.

## **3.2. Cloud Characteristics over the GIS**

With radiative transfer modeling confirming Bennartz's finding that cloud liquid water paths of 10-40 g/m<sup>2</sup> resulted in positive surface radiative forcing and further showing that cloud base height is not a significant factor in surface radiative forcing, satellite data from several sensors and platforms were then employed to determine the spatial frequency of occurrence of such clouds. Cloud properties were first retrieved using the MOD06 standard cloud product from MODIS onboard the NASA Aqua satellite. A cross-instrument comparison of cloud properties was conducted using MODIS/CALIOP/IIR matchup files. Finally, 1.6 μm and 3.7 μm reflectance data from the Terra satellite were combined with look up tables to convert 1.6 μm reflectance to optical depth and allow 3.7 μm reflectance to be used as a proxy for cloud phase.

### **3.2.1. MOD06 Collection 5 & 6 Standard Cloud Product**

Cloud properties were first retrieved using the MOD06 standard cloud product from MODIS onboard the NASA Aqua satellite. Despite the algorithm and product improvements from Collection-5 to Collection-6, no significant difference was observed. Figure 11 shows the spatial distribution of and percent of observations where liquid clouds occupied a particular pixel for July 2012 as detected by the MODIS sensor. The lack of liquid clouds away from the coastline is not consistent with the findings of Bennartz et al. (2013) which found an anomalously high amount of liquid clouds at Summit in the center of the GIS.

This highlights a key shortcoming of the MOD06 product in its lack of ability to reliably detect clouds over highly reflective surfaces such as snow and ice. The cloud detection issue becomes more apparent when using the MOD06 product to further investigate

clouds properties. Figure 12 shows the spatial distribution and percent of observations that a particular pixel was occupied by an optically thin ( $10 - 40 \text{ g/m}^2$ ) liquid cloud for July 2012 as detected by MODIS.

This lack of detection is due to the MOD06 default retrieval of cloud phase and optical depth (plus effective radius to calculate LWP) using visible and infrared channels over a highly reflective surface. Liquid water clouds in the Arctic are highly reflective and often very similar to the temperature of the underlying snow and ice surface. The two channel retrievals rely on a contrast existing between the clouds and the surface below. As a result of little or no contrast in the visible or infrared between the clouds and the GIS, MODIS standard cloud products could not reliably detect clouds over the higher elevations of the GIS away from the coastline.

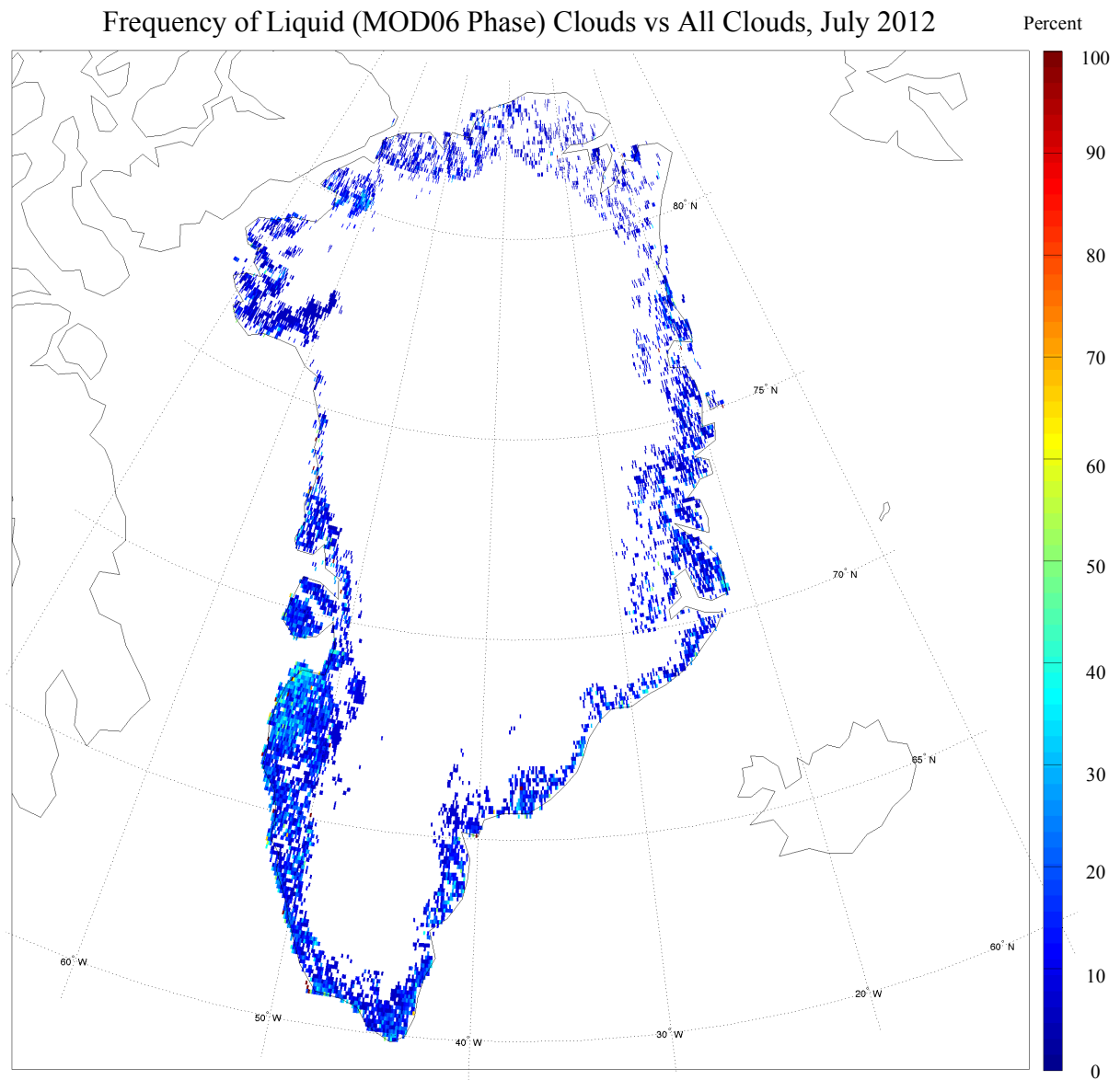


Figure 11: Frequency of liquid clouds as identified by MODIS cloud phase detection algorithm in the MOD06 product. Note the lack of detection of liquid clouds on the interior of Greenland.

## Frequency of Thin Liquid (MOD06 Phase, LWP) Clouds vs All Clouds, July 2012 Percent

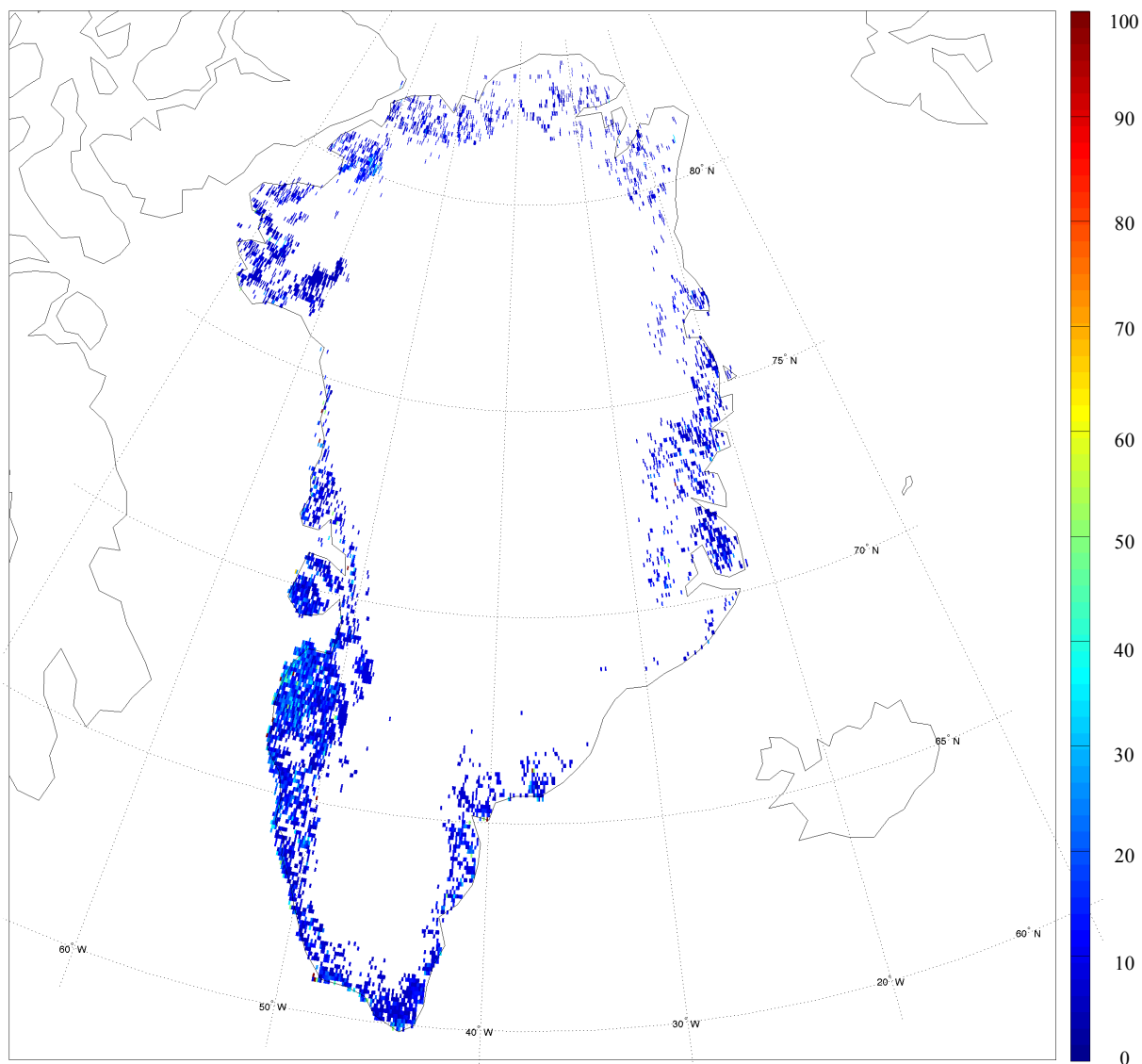


Figure 12: Frequency of optically thin ( $10 - 40 \text{ g/m}^2$ ) liquid clouds as identified by the MODIS cloud phase detection algorithm and MODIS liquid water path in the MOD06 product. Note the lack of detection of these clouds away from the coastline.

To overcome the issue with lack of contrast with the default visible and infrared retrieval method, another MOD06 product was tested that used the 1.6  $\mu\text{m}$  and 2.1  $\mu\text{m}$  channels to determine cloud optical depth. When compared with the standard retrieval method (Figure 13) the 1.6  $\mu\text{m}$  / 2.1  $\mu\text{m}$  optical depth product did not reliably detect optically thin clouds (1.5 – 6.5) and actually had a higher optical depth bias. When this distribution is plotted in terms of LWP using retrieved MODIS optical depth and cloud effective radius (Figure 14), the standard visible retrieval does a better job than the 1.6  $\mu\text{m}$  / 2.1  $\mu\text{m}$  for detecting thin clouds (10 – 40  $\text{g}/\text{m}^2$ ). However, as seen in Figures 11 and 12, these data are only valid for the sparse amount of data retrieved near the coast of the GIS.

Figures 15 and 16 show optical depth and liquid water path distribution from a 2° x 2° grid box centered over Summit for July 2012 comparing the standard and 1.6  $\mu\text{m}$  / 2.1  $\mu\text{m}$  retrievals. Retrievals are performed for all pixels regardless of cloud phase, temperature or solar zenith angle. When compared with the standard retrieval method (Figure 15), the 1.6  $\mu\text{m}$  / 2.1  $\mu\text{m}$  optical depth product detected slightly more optically thin clouds (1.5 – 6.5) and actually had a lower optical depth bias. When this distribution is plotted in terms of LWP using retrieved MODIS optical depth and cloud effective radius (Figure 16), the 1.6  $\mu\text{m}$  / 2.1  $\mu\text{m}$  retrieval does a better job than the standard visible retrieval for detecting thin clouds (10 – 40  $\text{g}/\text{m}^2$ ). Since no optically thin clouds were detected over Summit when liquid phase and cloudy constraints were in place, it was clear that another approach was needed involving other sensors or perhaps a more robust MODIS retrieval approach and cloud phase identification.

### MODIS MOD06 Tau Distribution Comparison, All GIS, July 2012, Cloudy & Liquid

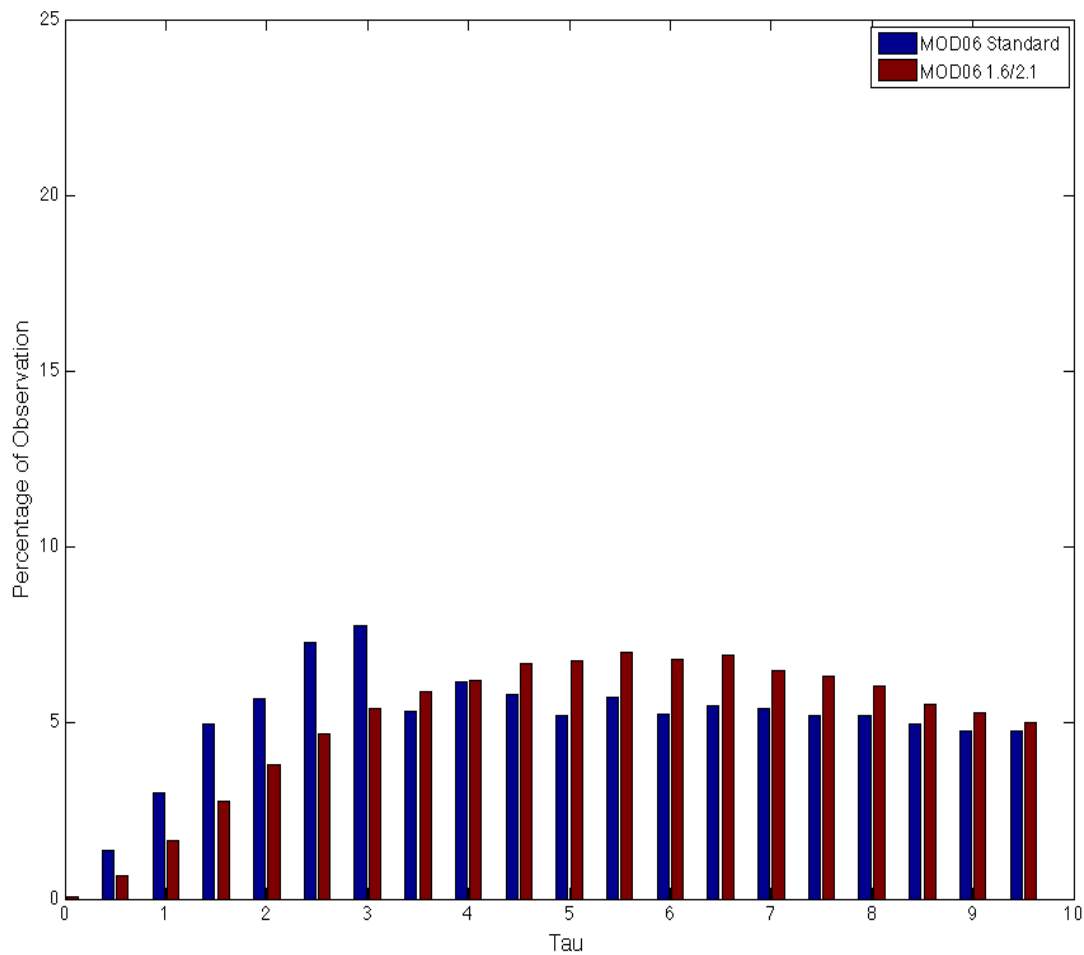


Figure 13: Distribution of MODIS cloud optical depth across the GIS for July 2012 comparing the standard and 1.6  $\mu\text{m}$  / 2.1  $\mu\text{m}$  retrievals. Data is plotted for each pixel that was determined to be cloudy, liquid phase with solar zenith angles less than 75 degrees.

## MODIS MOD06 LWP Distribution Comparison, All GIS, July 2012, Cloudy &amp; Liquid

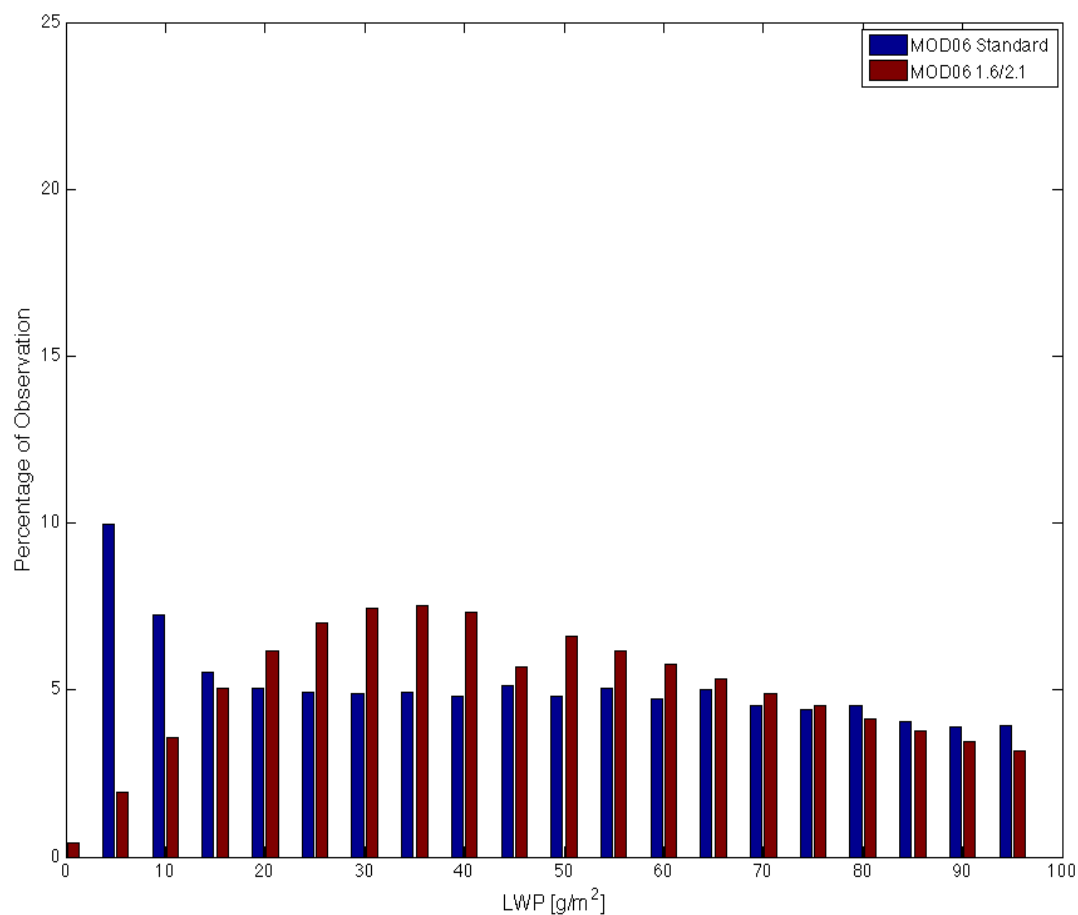


Figure 14: Distribution of MODIS liquid water path across the GIS for July 2012 comparing the standard and 1.6  $\mu\text{m}$  / 2.1  $\mu\text{m}$  retrievals. Data is plotted for each pixel that was determined to be cloudy, liquid phase with solar zenith angles less than 75 degrees.

### MODIS MOD06 Tau Distribution Comparison, 2x2 Degree Box at Summit, July 2012

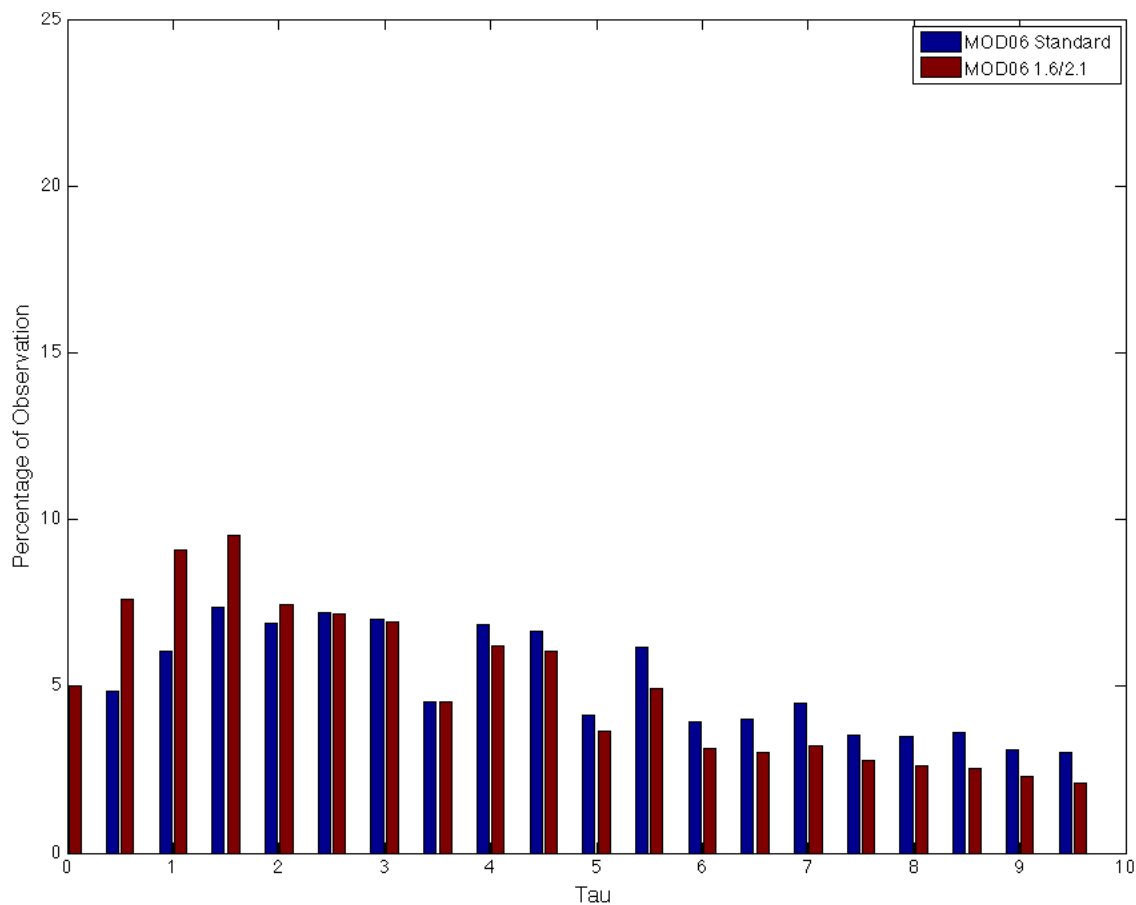


Figure 15: Distribution of MODIS cloud optical depth in a  $2^\circ \times 2^\circ$  grid box centered over Summit for July 2012 comparing the standard and  $1.6 \mu\text{m} / 2.1 \mu\text{m}$  retrievals. Data is plotted for all pixels regardless of cloud phase, temperature or solar zenith angle.

### MODIS MOD06 LWP Distribution Comparison, 2x2 Degree Box at Summit, July 2012

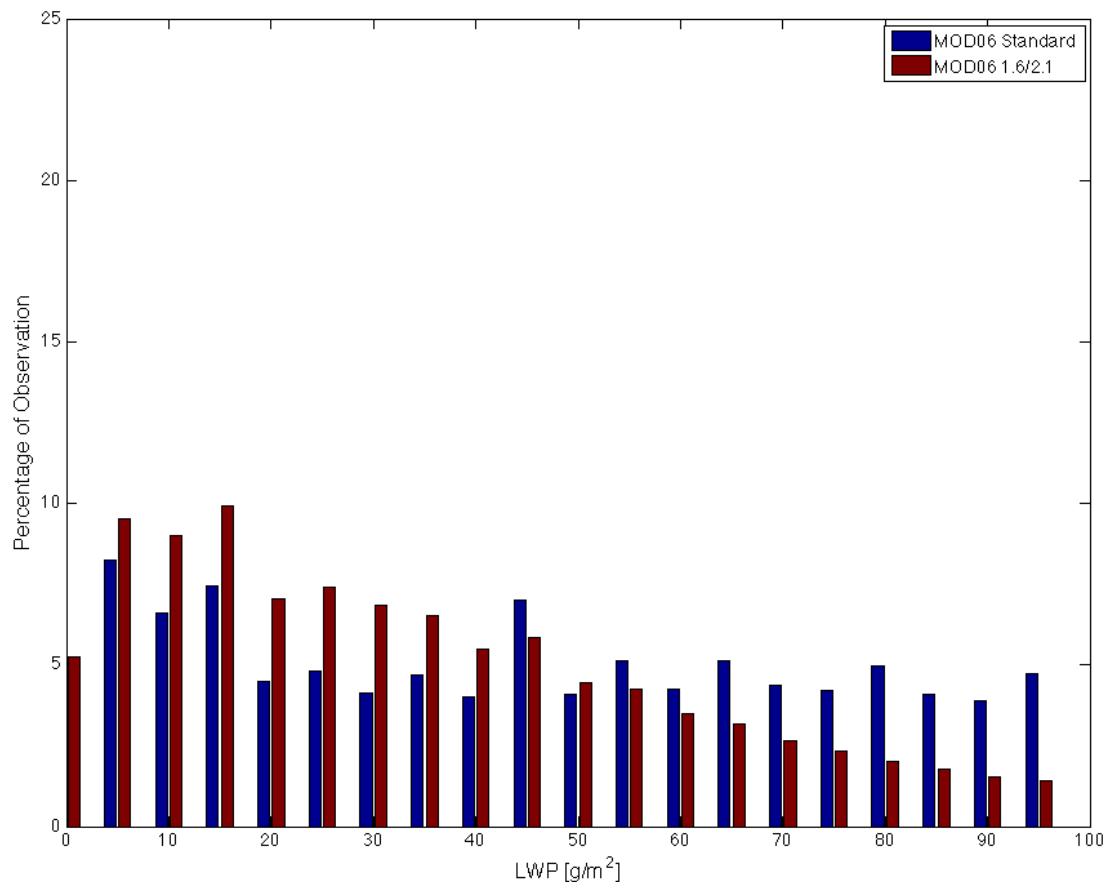


Figure 16: Distribution of MODIS liquid water path in a 2° x 2° grid box centered over Summit for July 2012 comparing the standard and 1.6 μm / 2.1 μm retrievals. Data is plotted for all pixels regardless of cloud phase, temperature or solar zenith angle.

### 3.2.2. MODIS/CALIOP/IIR Matchups

The Aqua satellite being in NASA's A-Train of satellites allowed for matching-up of data from several sensors onboard other A-Train satellites. A cross-instrument comparison of cloud optical depth was conducted using data from the MODIS, CALIOP and IIR sensors. The goal was to determine which sensor or combination of data from different sensors produced a LWP distribution plot that most closely resembled Figure 17, which shows ground based LWP observations from the microwave radiometer from Summit Station. The

first step was to plot optical depth retrievals from each sensor against each other to determine the degree of consistency between sensors.

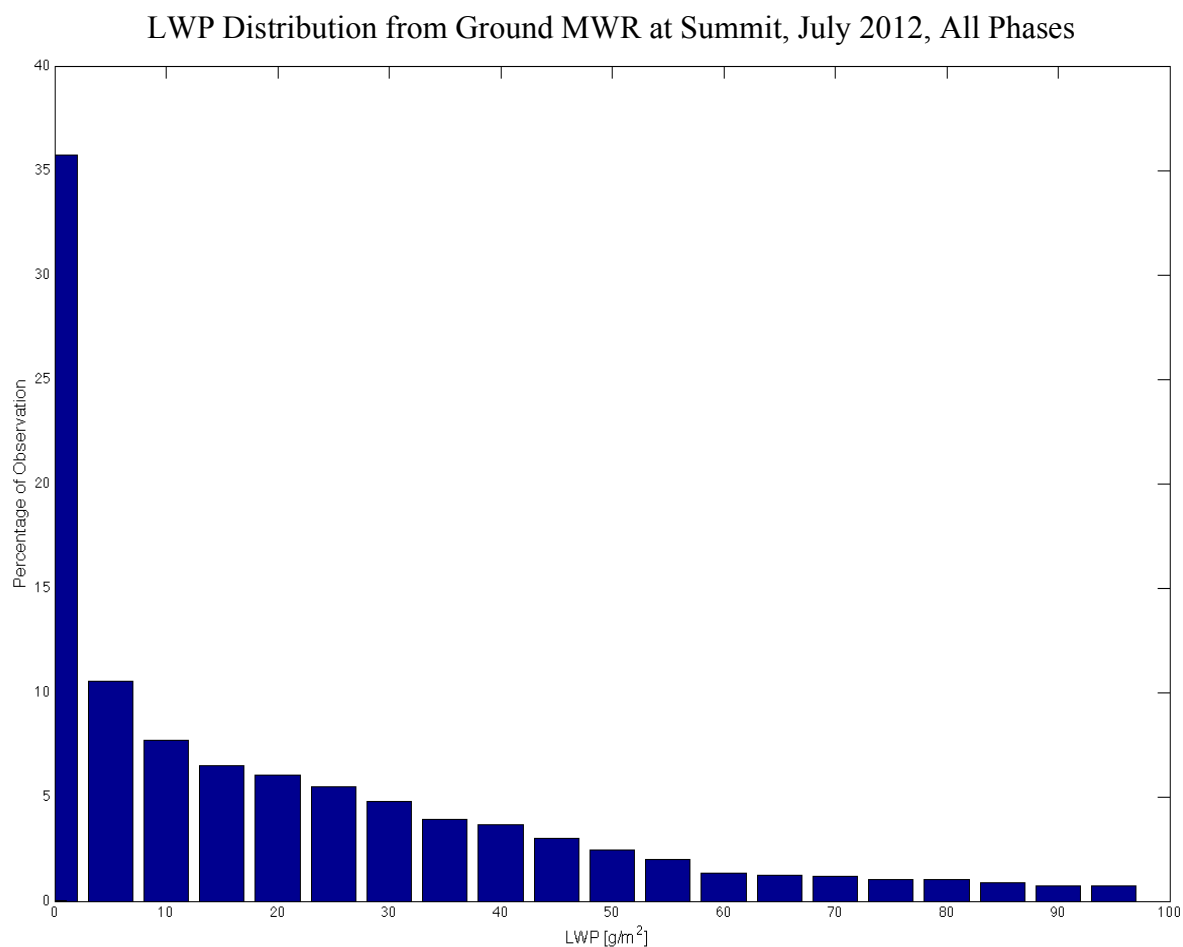


Figure 17: Distribution of observed liquid water path values for all July 2012 as observed by the microwave radiometer (MWR) at Summit Station. Data are binned every  $5 \text{ g/m}^2$ . The left-most bar is  $0 - 5 \text{ g/m}^2$ , the second  $5 - 10 \text{ g/m}^2$ , then  $10 - 15 \text{ g/m}^2$ , ending with the rightmost bar as  $95 - 100 \text{ g/m}^2$ . MWR data provided by R. Bennartz.

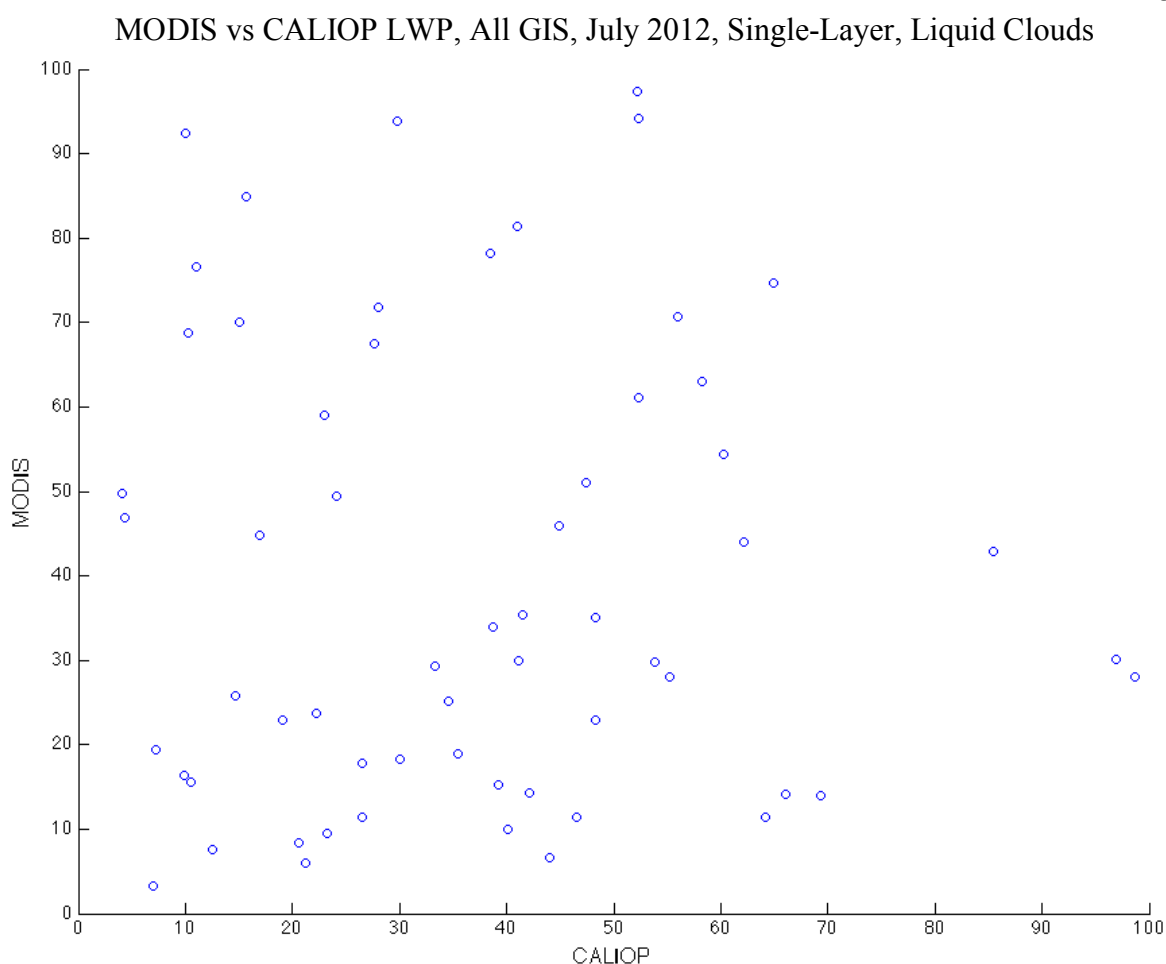


Figure 18: MODIS versus CALIOP liquid water path across the GIS for July 2012 where a pixel was determined to be cloudy, liquid phase, single-layer cloud with sensor and solar zenith angles less than 75 degrees.

Figure 18 shows a plot of MODIS versus CALIOP liquid water path for pixels identified by both CALIOP and MODIS to be cloudy with liquid phase and single layer clouds. Note the low number of data points which suggests that there is not much agreement between CALIOP and MODIS when detecting single-layer, liquid cloud pixels. Because of sensor design, CALIOP can only detect optical depths up to between 4 and 5 (CALIPSO 2013), slightly below the top of our target range of 1.5 – 6.5, corresponding to a liquid water

path of 10 – 40  $\text{g}/\text{m}^2$ . Note that the CALIOP instrument does not provide a retrieved value for cloud particle effective radius. Thus, the IIR retrieved effective radius was used when calculating LWP for the CALIOP instrument.

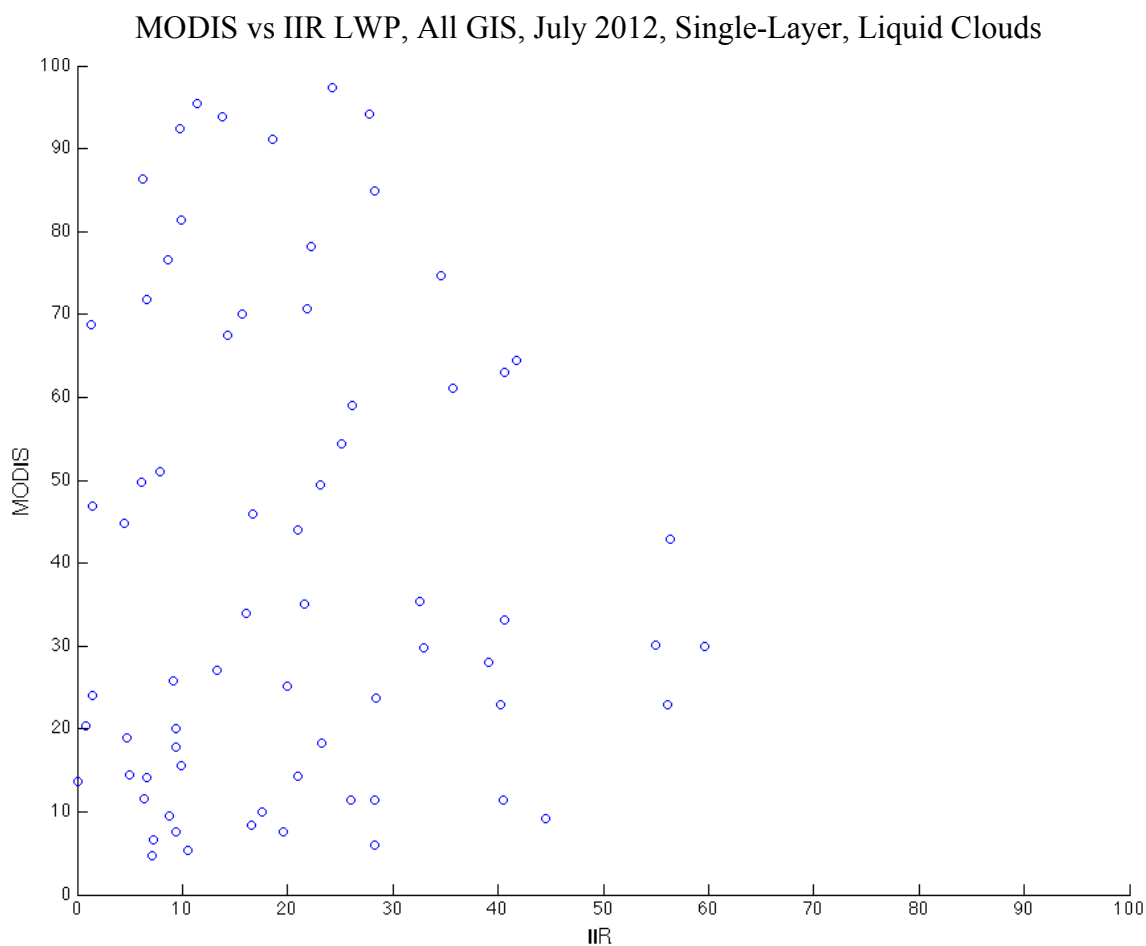


Figure 19: MODIS versus IIR liquid water path across the GIS for July 2012 where a pixel was determined to be cloudy, liquid phase, single-layer cloud with sensor and solar zenith angles less than 75 degrees.

Figure 18 shows a plot of MODIS versus IIR liquid water path for pixels identified by both IIR and MODIS to be cloudy with liquid phase and single layer clouds. LWP retrievals

from both sensors align show a clear higher optical depth bias by MODIS when compared to the MODIS/CALIOP plot.

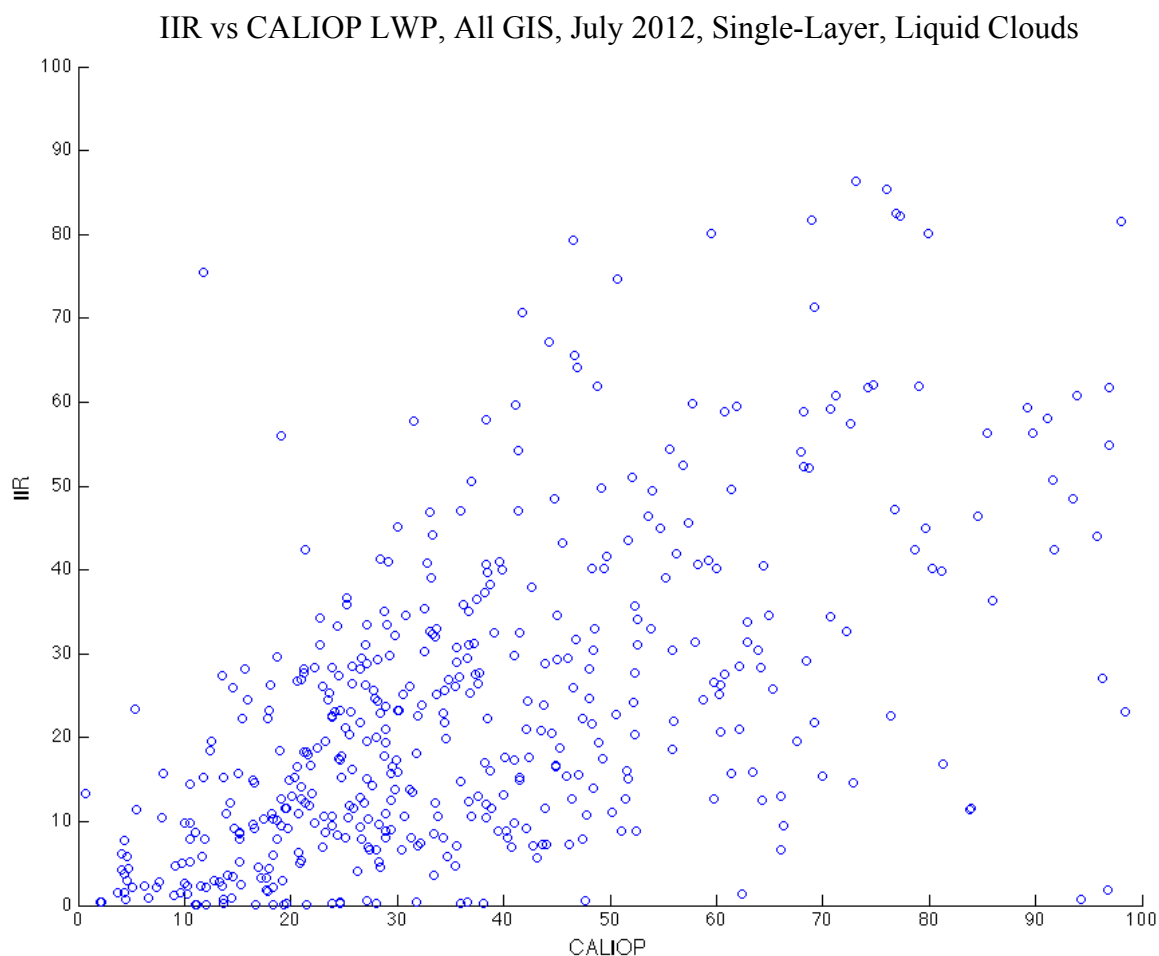


Figure 20: IIR versus CALIOP liquid water path across the GIS for July 2012 where a pixel was determined to be cloudy, liquid phase, single-layer cloud with sensor and solar zenith angles less than 75 degrees.

Figure 19 shows a plot of IIR versus CALIOP liquid water path for pixels identified by both IIR and CALIOP to be cloudy with liquid phase and single layer clouds. Liquid water path retrievals appear to show good agreement between the two sensors. Note that the

CALIOP instrument does not provide a retrieved value for cloud particle effective radius. Thus, the IIR retrieved effective radius was used when calculating LWP for the CALIOP instrument. These two sensors have the best agreement in liquid water path out of all three.

The A-Train instrument optical depth comparison plots (Figures 18 – 20) highlight the lack of consistency between the different sensors for liquid water path. Similar disagreements in observed Arctic cloud characteristics between MODIS and CALIPSO sensors was noted by Chan and Comiso (2013) and Liu et al. (2010). Figures 11 and 12 highlight a major shortcoming of the MODIS sensor. Nearly all the retrievals for July 2012 swath pixels identified to be cloudy, liquid phase and optically thin (1.5 – 6.5 optical depth) are located along the coast, not in the interior of the GIS where we wish to focus our analysis. Similar challenges in remotely sensed observations of thin liquid water clouds were noted by Turner et al. (2007). Once again, an alternate, more accurate optical depth retrieval method had to be pursued.

### **3.2.3. PATMOS-x & MOD02 1.6 $\mu\text{m}$**

The lack of consistency and spatial coverage over the GIS in the optical depth retrievals in the standard cloud products from MODIS, CALIOP and IIR sensors prompted the need for a non-standard optical depth retrieval method. MODIS was the sensor of choice and for ease of analysis, the PATMOS-x product was employed. Instead of the MODIS standard cloud products that use a two-channel retrieval method, a single channel 1.6  $\mu\text{m}$  retrieval was performed using a look up table. A visible channel was not included for the retrieval of optical depth because for thin clouds over a highly reflective snow or ice surface,

a visible channel retrieval does not provide an unambiguous optical depth solution (Key 2002).

Results for July 2011 and July 2012 are presented in Figures 21 – 32. Figures 21 and 22 show the number of cloudy days per pixel for July 2011 and 2012, respectively. Cloudy days were identified as where the PATMOS-x cloud mask classified a pixel as cloudy. All clouds (liquid & ice phase and all optical depths) are included. There is a notably higher presence of clouds along the shorelines in both years. July 2011 had a higher presence of clouds along the southern tip of the GIS while in 2012, the highest number of clouds was concentrated over the northern and central parts of the GIS.

The PATMOS-x cloud mask (Figures 21 and 22) shows a marked improvement in detection of all clouds, especially over the center of the GIS by the PATMOS-x product as compared to the standard A-Train sensor cloud products (Figures 13 – 20). Plots of daily cloud fraction using a  $2^\circ \times 2^\circ$  (400 pixel) grid box centered over Summit for July 2011 and July 2012 were created (Figures 23 and 24). The major difference in daily cloud fraction over Summit between July 2011 and 2012 is that clouds were present more consistently in July 2011 than July 2012.

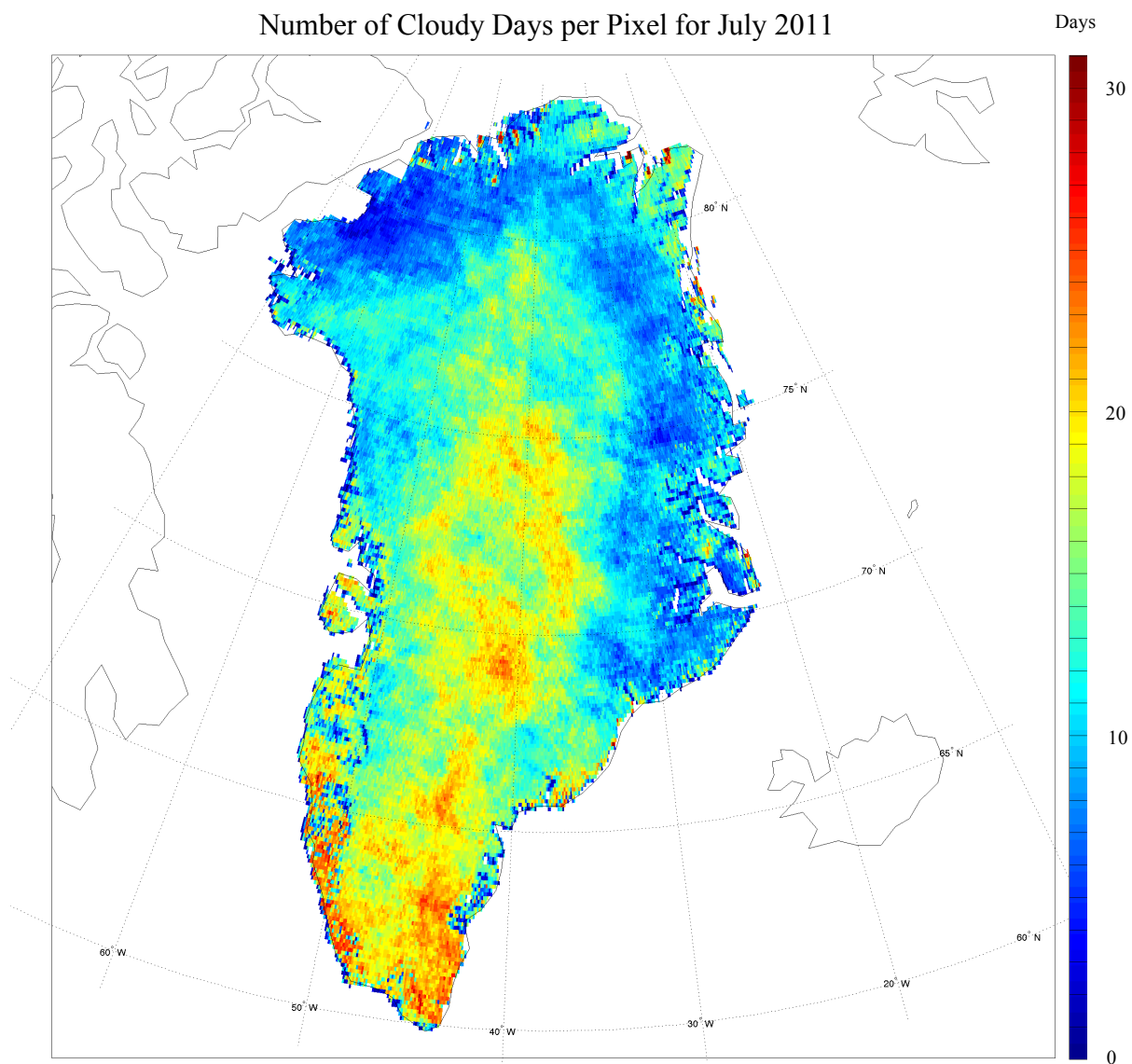


Figure 21: Total number of cloudy days per  $0.1^\circ \times 0.1^\circ$  pixel for July 2011. Cloudy days were identified as where the PATMOS-x cloud mask classified a pixel as cloudy. All clouds (liquid, ice and all thicknesses) are included.

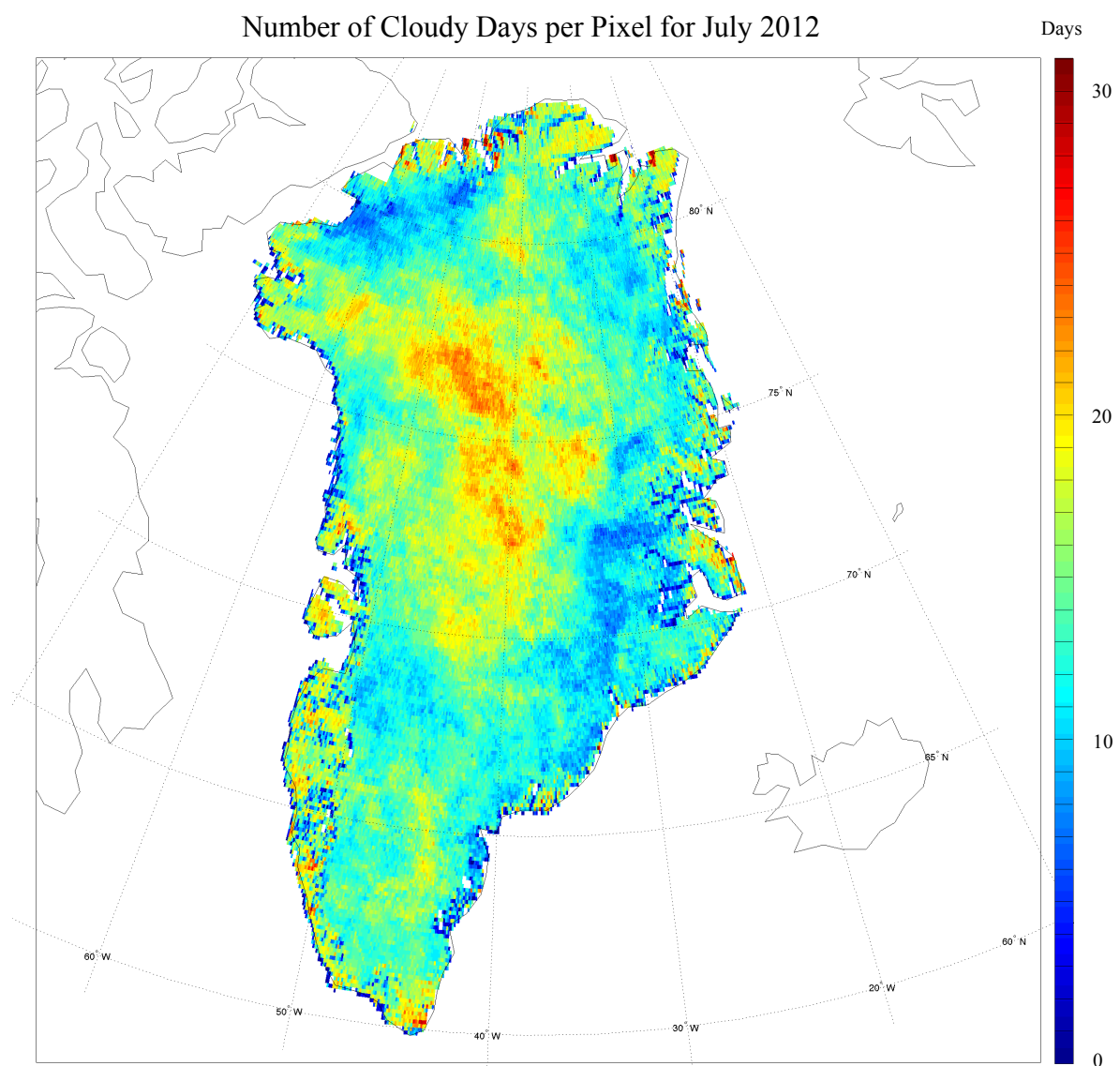


Figure 22: Total number of cloudy days per  $0.1^\circ \times 0.1^\circ$  pixel for July 2012. Cloudy days were identified as where the PATMOS-x cloud mask classified a pixel as cloudy. All clouds (liquid, ice and all thicknesses) are included.

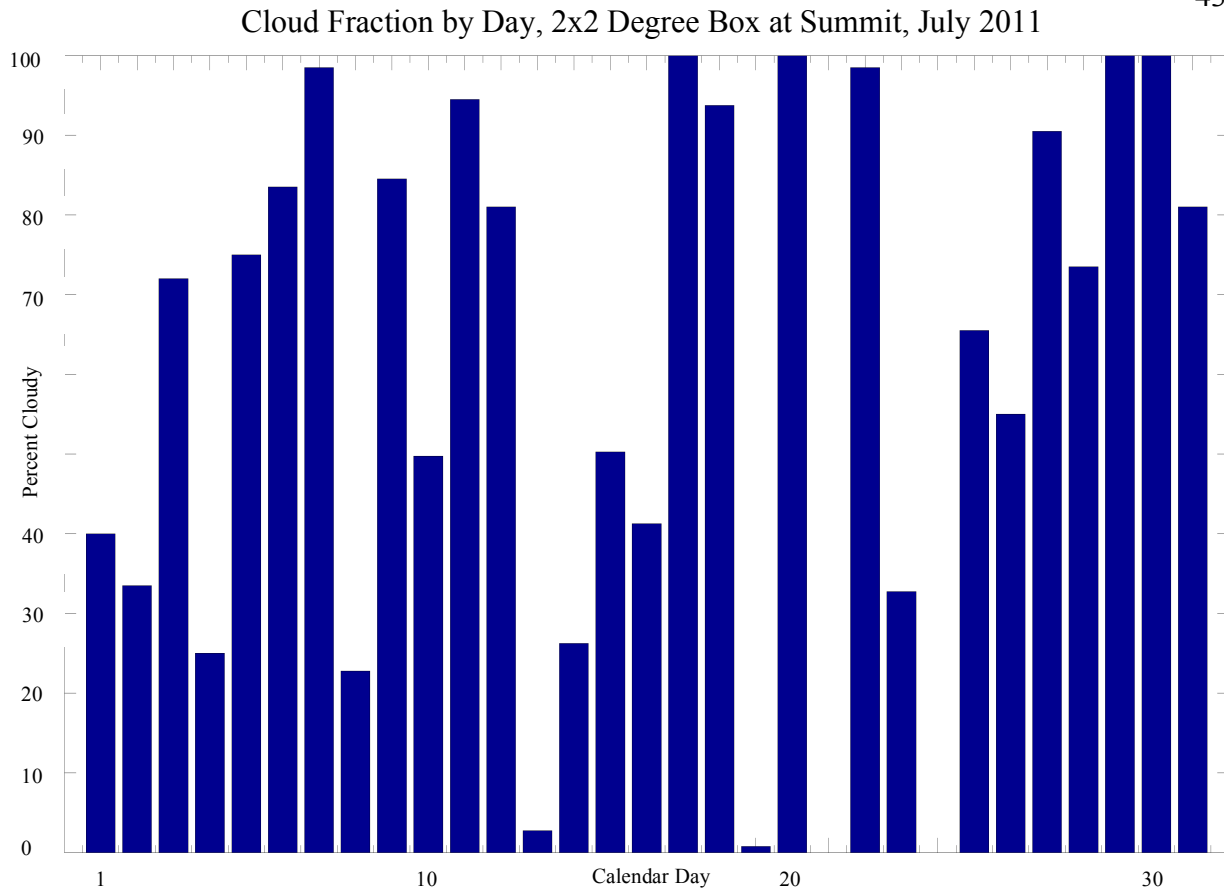


Figure 23: Percentage of cloudy pixels in a  $2^\circ \times 2^\circ$  grid box centered over Summit for July 2011.

Cloudy pixels were identified as where the PATMOS-x cloud mask classified a pixel as cloudy. All clouds (liquid, ice and all thicknesses) are included.

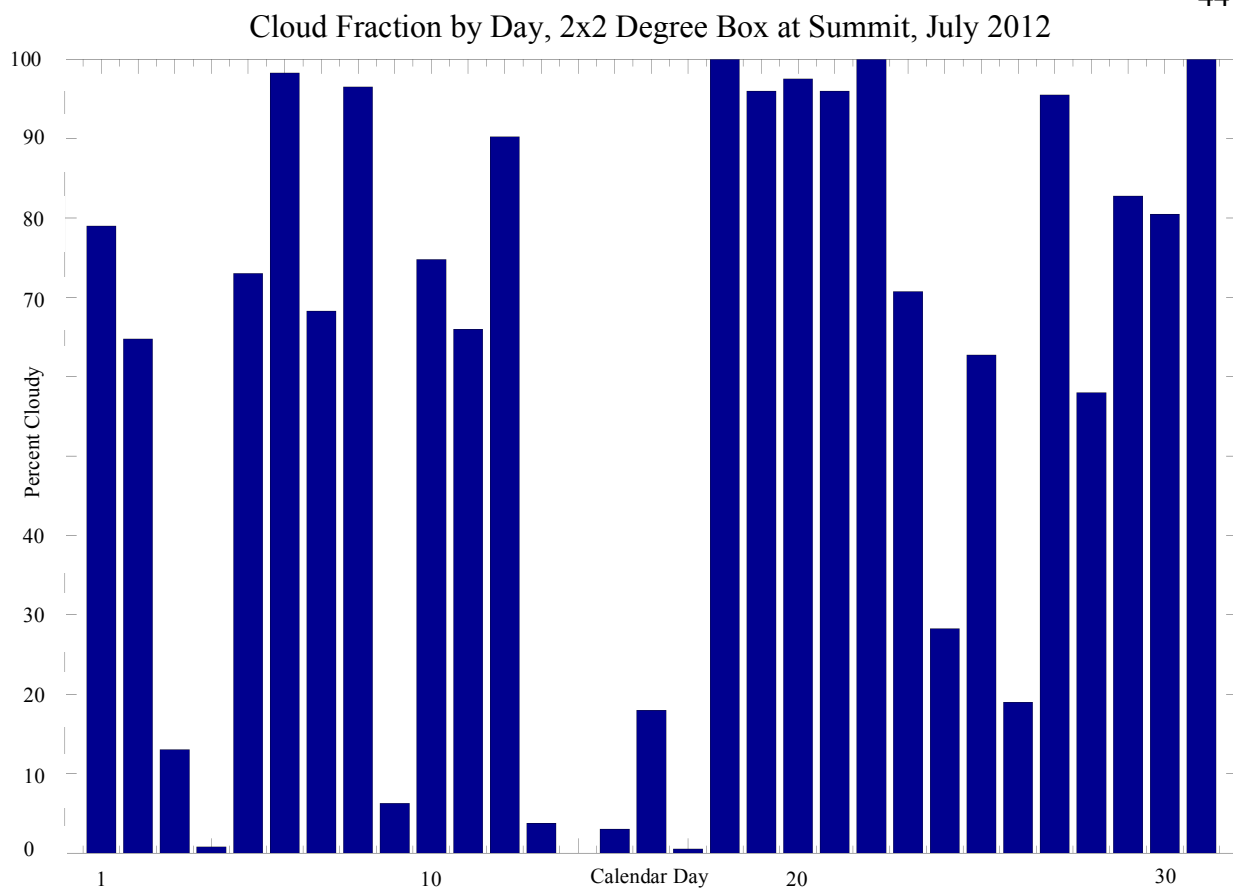


Figure 24: Percentage of cloudy pixels in a  $2^\circ \times 2^\circ$  grid box centered over Summit for July 2012.

Cloudy pixels were identified as where the PATMOS-x cloud mask classified a pixel as cloudy. All clouds (liquid, ice and all thicknesses) are included.

With the success of PATMOS-x cloud detection, improved retrievals of cloud optical depth over ice and snow was the next challenge. Using the 1.6  $\mu\text{m}$  reflectance from MODIS and a corresponding LUT, accurate cloud optical depth retrievals over ice and snow across the entire GIS were now possible. Most importantly, analysis of cloud conditions and properties in the interior of the GIS, including Summit was feasible. This allowed for investigation of the fraction of thin liquid clouds (liquid water path was between 10 and 40  $\text{g/m}^2$ ) versus all clouds over Summit in July 2011 and July 2012 using a  $2^\circ \times 2^\circ$  grid box centered over Summit (Figures 25 and 26, respectively). Cloudiness was identified as where the PATMOS-x cloud mask classified a pixel as cloudy.

Figures 25 and 26 show that the major difference in the fraction of thin liquid clouds versus all clouds over Summit between July 2011 and 2012 is that thin clouds were present more consistently and frequently in July 2011 than July 2012.

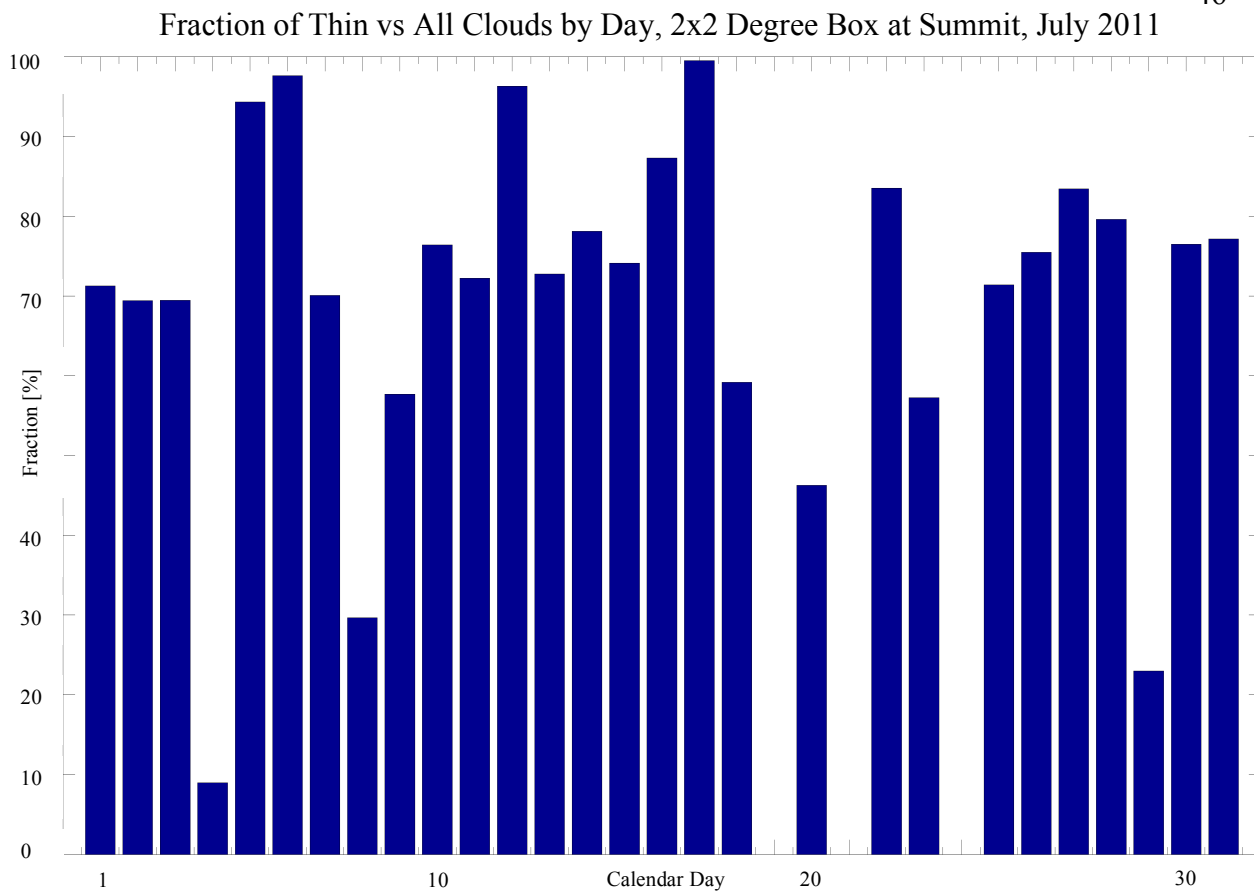


Figure 25: Percentage of pixels that were identified as having thin, liquid clouds versus any cloud in a  $2^\circ \times 2^\circ$  grid box centered over Summit for July 2011

Fraction of Thin vs All Clouds by Day, 2x2 Degree Box at Summit, July 2011

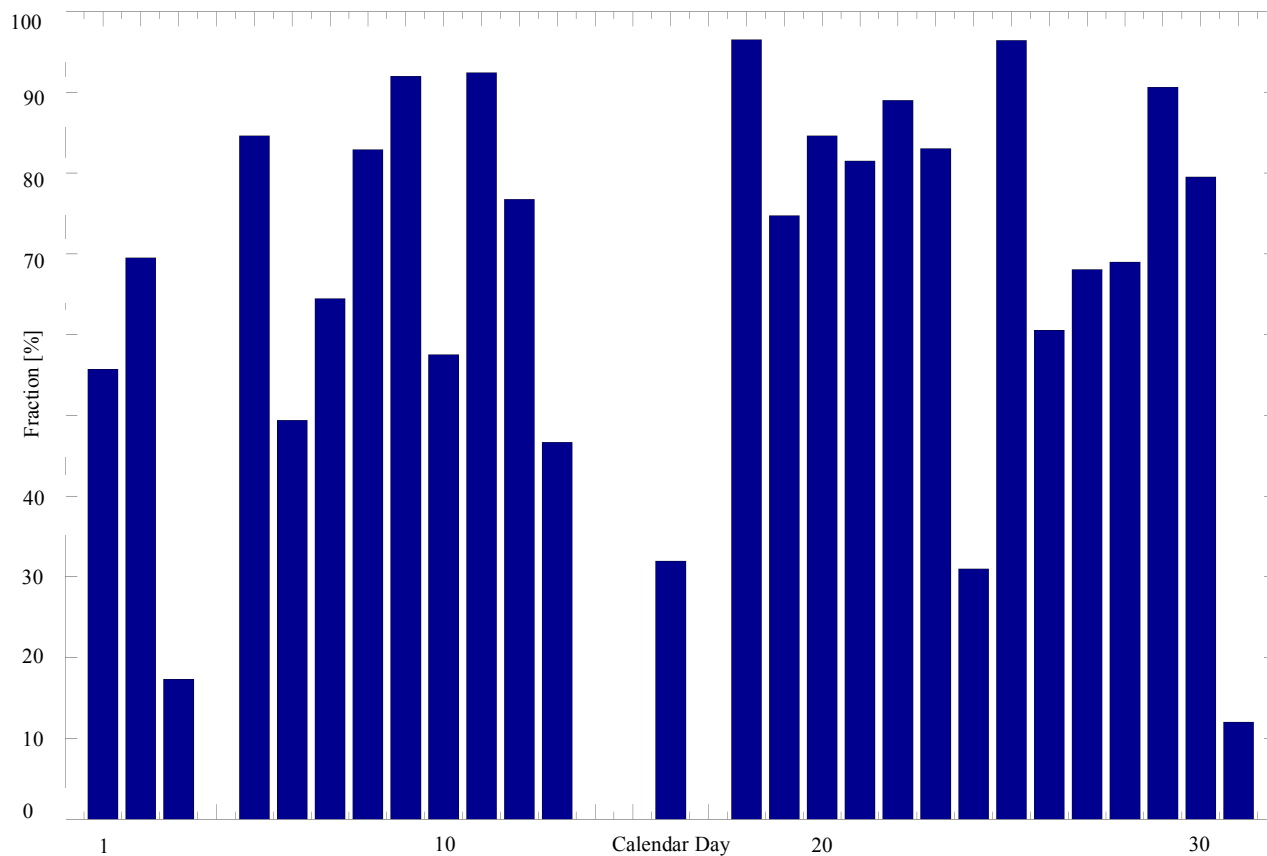


Figure 26: Percentage of pixels that were identified as having thin, liquid clouds versus any cloud in a 2° x 2° grid box centered over Summit for July 2012.

### 3.2.4. Cloud Phase Determination

Standard cloud phase detection products for MODIS proved unreliable over the GIS. Therefore, like the optical depth retrievals, a new method for discriminating cloud phase was needed. The raw 3.7  $\mu\text{m}$  reflectance from the MOD02 data was chosen as proxy for cloud phase. Liquid cloud pixels were classified as having a 3.7  $\mu\text{m}$  reflectance greater than 0.07. Figures 7 and 8 show LUT results of optical depth versus reflectance for liquid and ice clouds respectively. The 0.07 3.7  $\mu\text{m}$  reflectance separation between liquid and ice clouds does not account for mixed-phase clouds. Little is known about the frequency of mixed phase clouds over the GIS including the proportion of liquid to ice particles (Curry et al. 1996).

Even if modeling was done for a certain proportion of liquid and ice particles, satellite remote sensing of mixed phase clouds is of high uncertainty (Baum et al. 2012). In addition, the MODIS Collection-6 phase algorithm no longer classifies supercooled/mixed-phase clouds and instead classifies them as being of uncertain phase. The ability of the Collection-6 infrared-phase algorithm to infer the phase of optically thin ice clouds has improved, but phase determination for supercooled water clouds is problematic and remains as an open issue in Arctic remote sensing (Baum et al. 2012).

Figures 27 and 28 show how the 3.7  $\mu\text{m}$  reflectance threshold helped to identify the frequency and location of liquid clouds for July 2011 (Figure 27) and July 2012 (Figure 28). For increased confidence in liquid cloud detection, the PATMOS-x cloud top temperature was combined with the 3.7  $\mu\text{m}$  reflectance threshold. This process classifies pixels with a cloud top temperature greater than 243 K and 3.7  $\mu\text{m}$  reflectance greater than 0.07 as a liquid cloud. Figures 29 and 30 show the frequency and location of liquid clouds using the new classification scheme for July 2011 (Figure 29) and July 2012 (Figure 30).

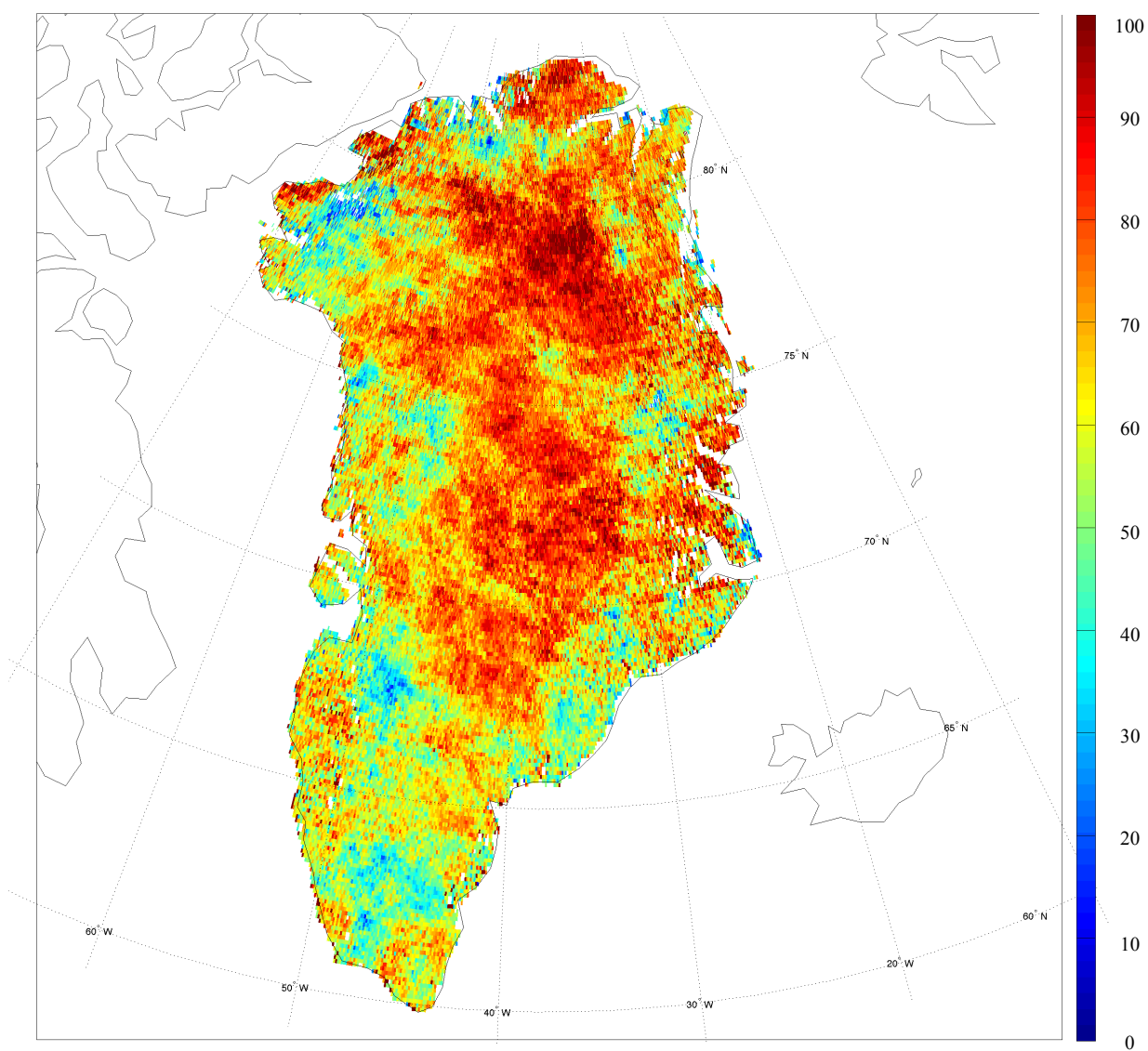
Fraction of Liquid ( $3.7 \mu\text{m} > .07$ ) vs All Clouds, July 2011

Figure 27: Frequency of liquid pixels versus cloudy pixels for July 2011. Liquid pixels were identified as where the  $3.7 \mu\text{m}$  reflectance was greater than 0.07.

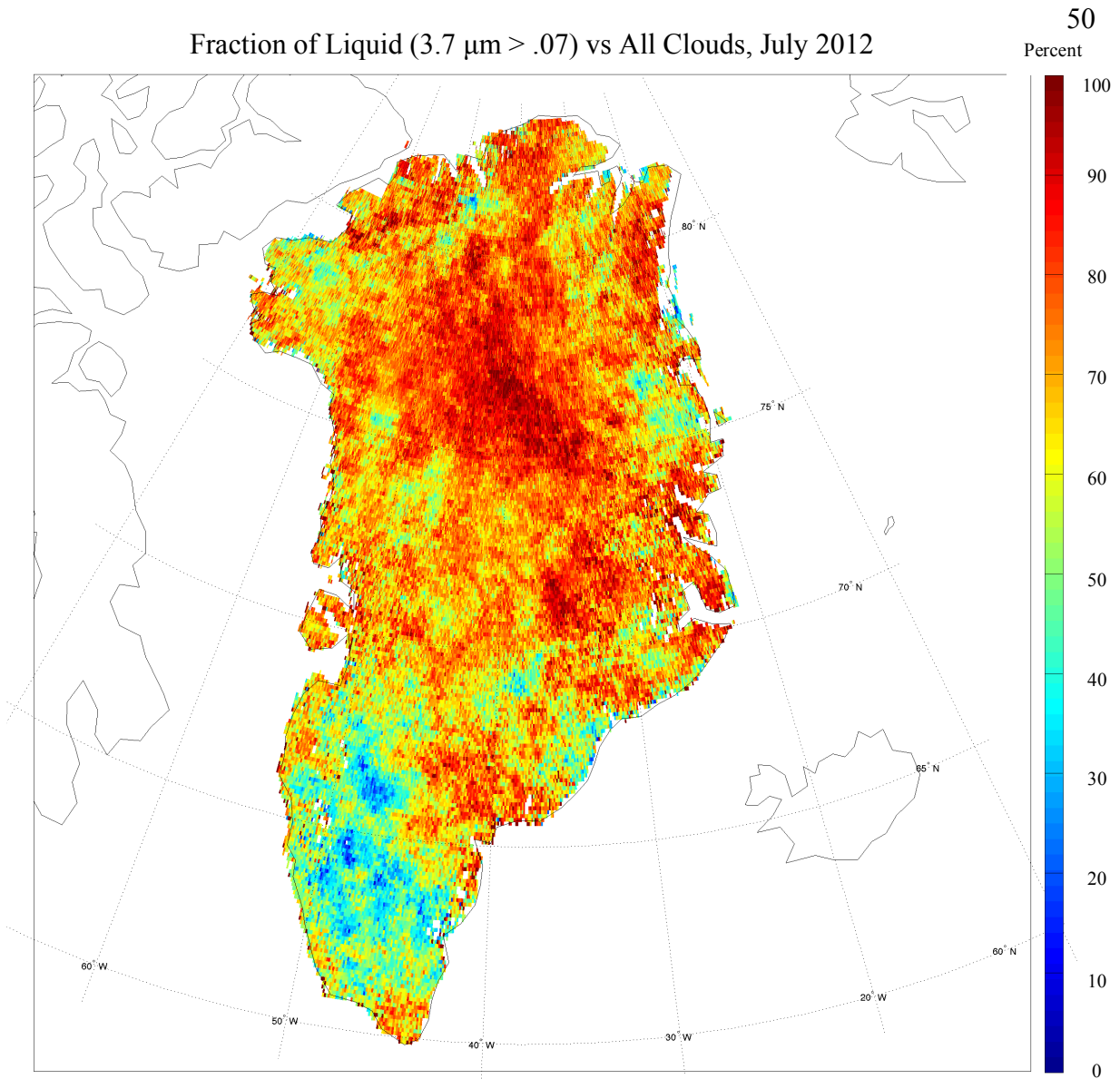


Figure 28: Frequency of liquid pixels versus cloudy pixels for July 2012. liquid pixels were identified as where the  $3.7 \mu\text{m}$  reflectance was greater than 0.07.

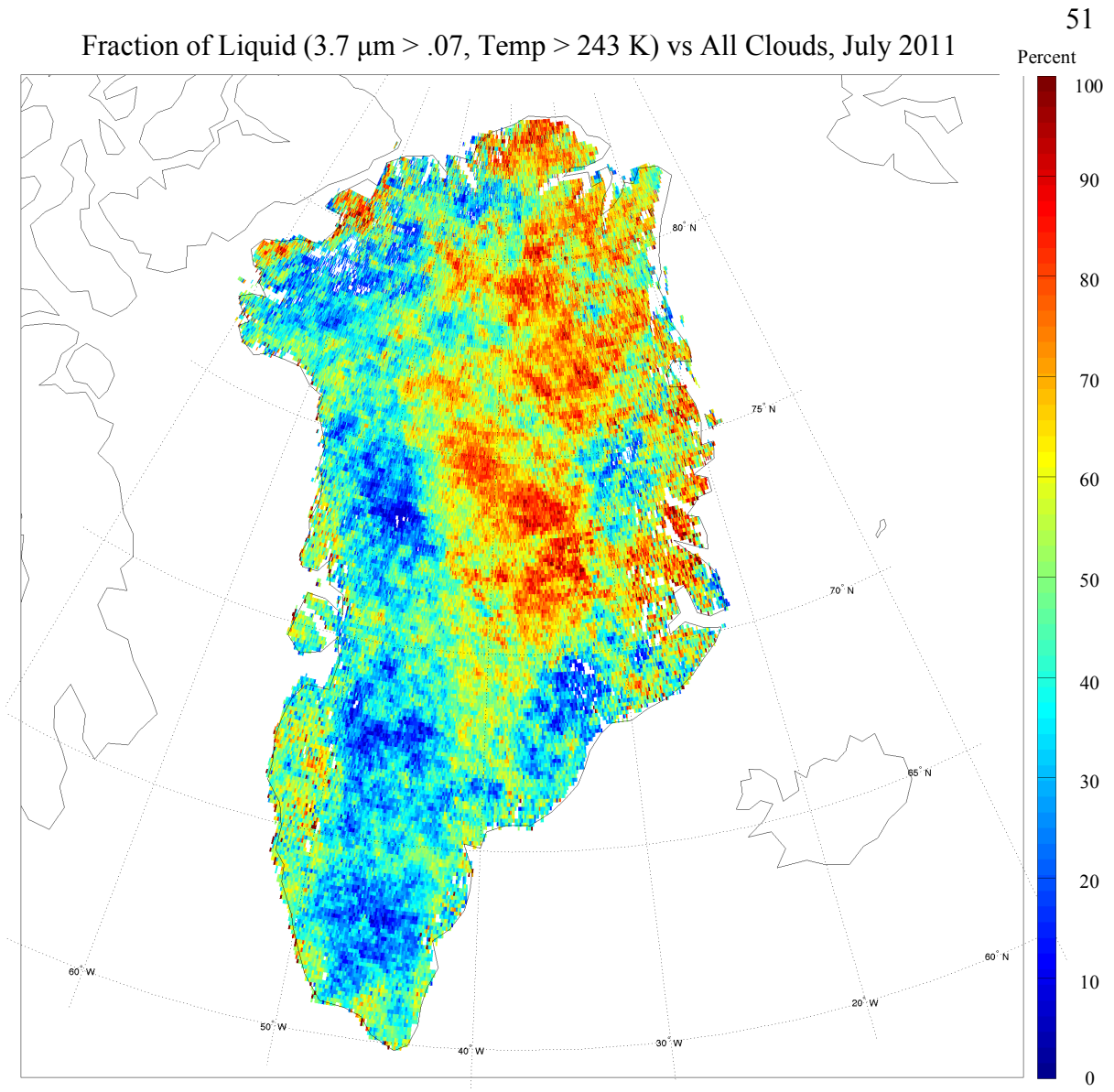


Figure 29: Frequency of liquid pixels versus cloudy pixels for July 2011. Liquid pixels were identified as where the  $3.7 \mu\text{m}$  reflectance was greater than 0.07 and cloud top temperature was greater than 243 K.

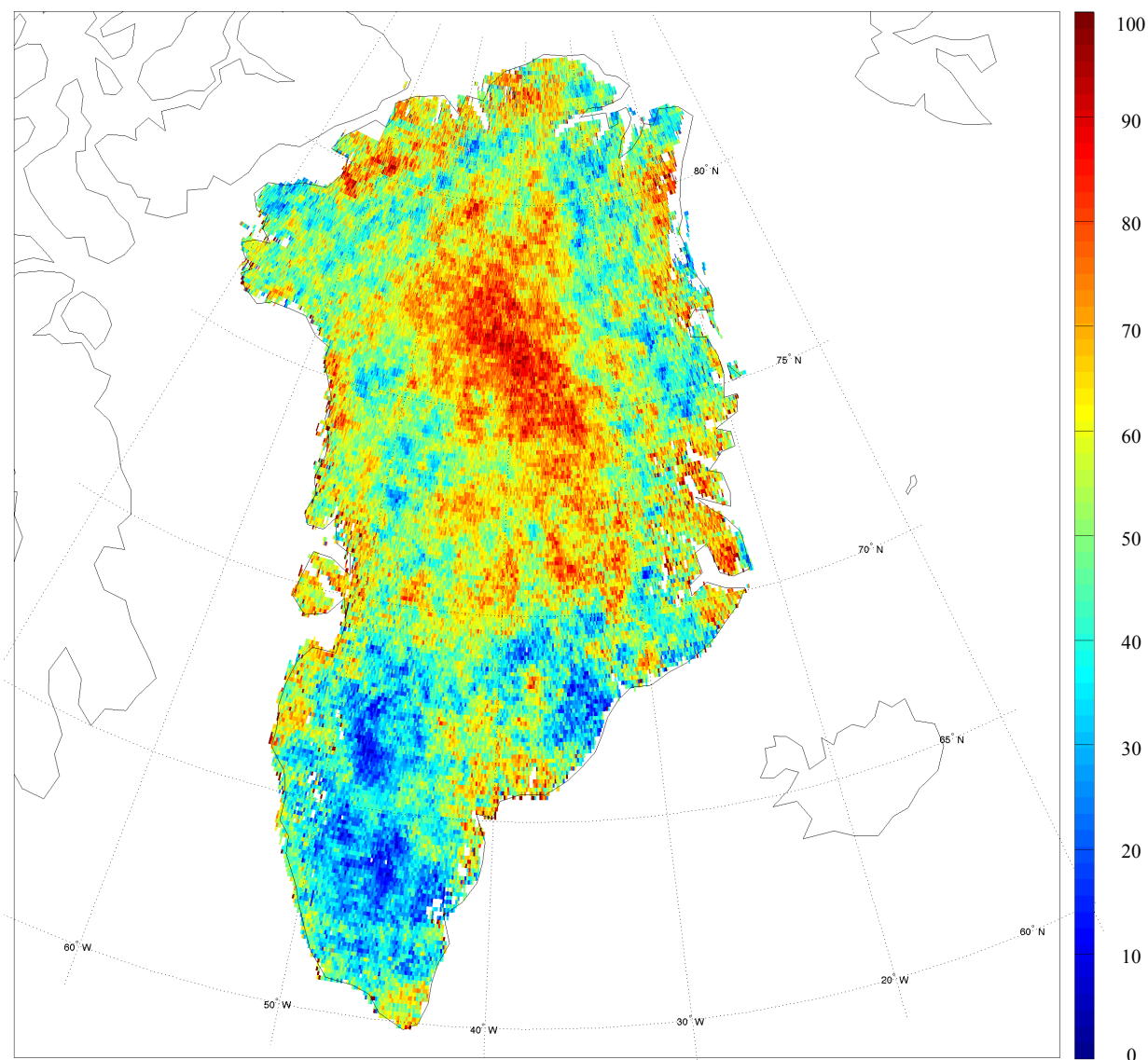
Fraction of Liquid ( $3.7 \mu\text{m} > .07$ , Temp  $> 243 \text{ K}$ ) vs All Clouds, July 2012

Figure 30: Frequency of liquid pixels versus cloudy pixels for July 2012. Liquid pixels were identified as where the  $3.7 \mu\text{m}$  reflectance was greater than 0.07 and cloud top temperature was greater than 243 K.

For July 2011, using only 3.7  $\mu\text{m}$  reflectance greater than 0.07 for liquid cloud phase determination shows that the highest frequency of liquid clouds occurs over central and northern GIS, coast to coast with the strongest signal along the innermost part of the GIS. Combining the 3.7  $\mu\text{m}$  reflectance and cloud top temperature methods puts highest frequency of liquid clouds over the highest elevations of GIS, especially the east-central and northeast, and drastically reduces their frequency of occurrence along shorelines.

For July 2012, using only 3.7  $\mu\text{m}$  reflectance greater than 0.07 for liquid cloud phase determination shows that the highest frequency of liquid clouds occurs over northern and central GIS, coast to coast with a weaker signal along shorelines and no separation in between. Combining the 3.7  $\mu\text{m}$  reflectance and cloud top temperature methods puts highest frequency of liquid clouds over the highest elevations of GIS and drastically reduces it along shorelines.

Coupling the 3.7  $\mu\text{m}$  reflectance and cloud top temperature liquid cloud identification methods with 1.6  $\mu\text{m}$  retrievals of optical depth and assumed 6.3  $\mu\text{m}$  effective particle radius, the frequency of occurrence and spatial extent of optically thin liquid clouds across the GIS can be analyzed. Figures 31 and 32 show the frequency and location of optically thin liquid clouds using the combined cloud top temperature and 3.7  $\mu\text{m}$  reflectance liquid cloud classification scheme with liquid water path calculated using 1.6  $\mu\text{m}$  optical depth with an assumed effective radius of 6.3  $\mu\text{m}$  for July 2011 (Figure 31) and July 2012 (Figure 32).

Thin Liquid ( $3.7 \mu\text{m} > .07$ ,  $\text{Temp} > 243 \text{ K}$ ,  $\text{LWP} 10 - 40 \text{ g/m}^2$ ) vs All Clouds, July 2011

54  
Percent

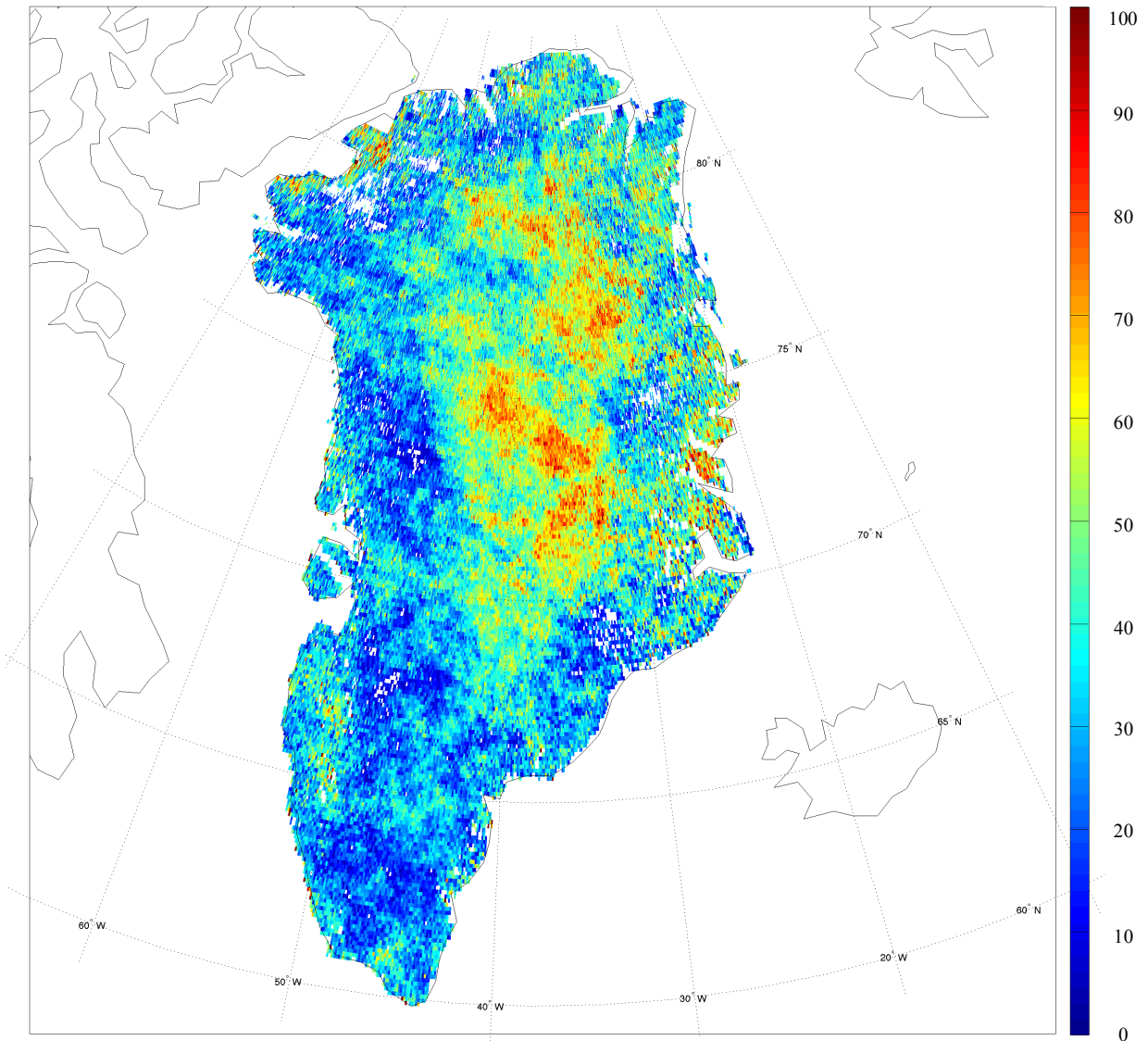


Figure 31: Frequency of thin liquid cloud pixels versus cloudy pixels for July 2011. Liquid pixels were identified as where the  $3.7 \mu\text{m}$  reflectance was greater than 0.07 and cloud top temperature was greater than 243 K. Optically thin pixels were identified where calculated LWP was between 10-40  $\text{g/m}^2$  using an assumed  $6.3 \mu\text{m}$  particle radius.

Thin Liquid ( $3.7 \mu\text{m} > .07$ ,  $\text{Temp} > 243 \text{ K}$ ,  $\text{LWP} 10 - 40 \text{ g/m}^2$ ) vs All Clouds, July 2012 Percent

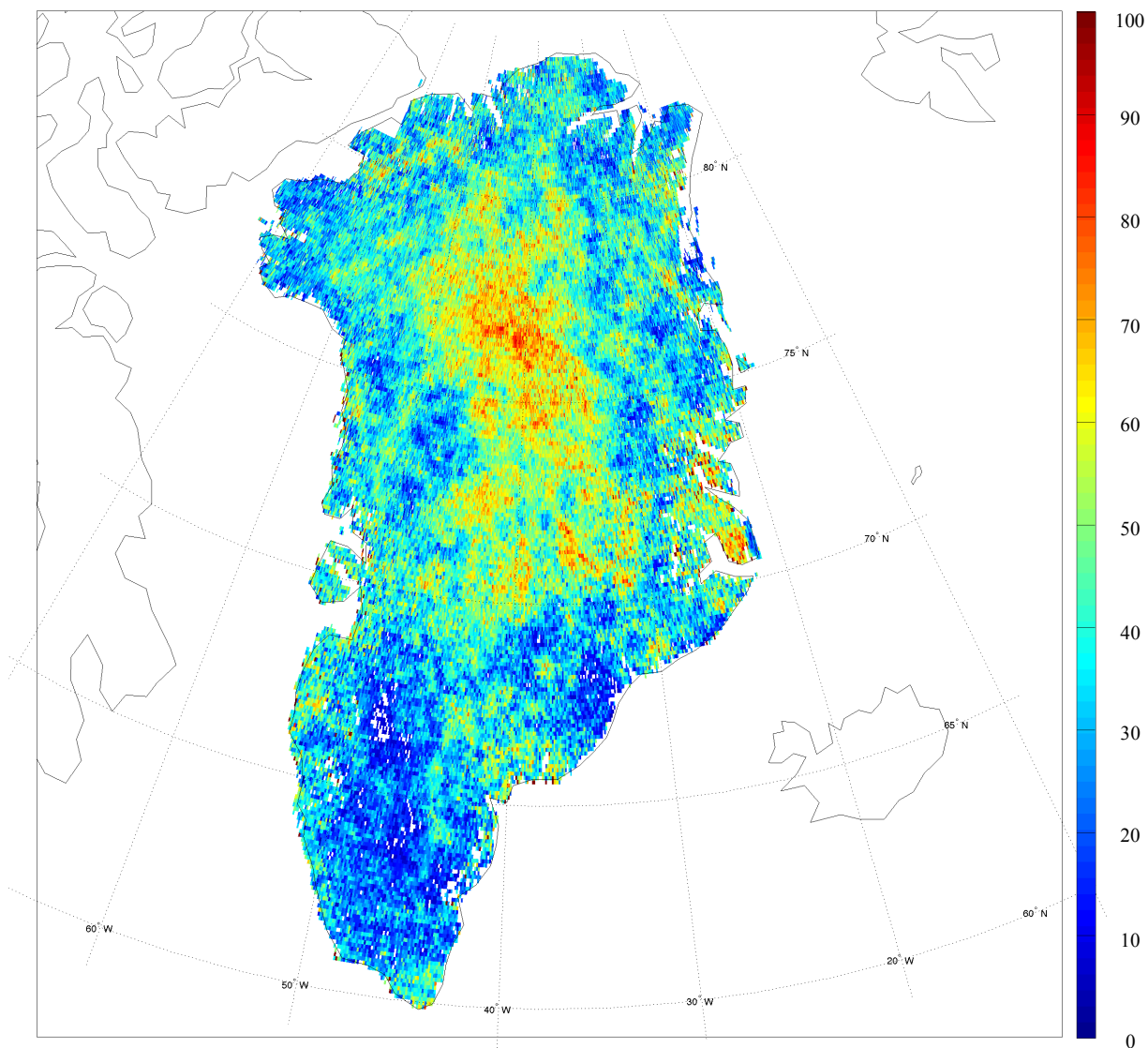


Figure 32: Frequency of thin, liquid cloudy pixels versus cloudy pixels for July 2012. Liquid pixels were identified as where the  $3.7 \mu\text{m}$  reflectance was greater than 0.07 and cloud top temperature was greater than 243 K. Optically thin pixels were identified where calculated LWP was between 10-40  $\text{g/m}^2$  using an assumed  $6.3 \mu\text{m}$  particle radius.

ICECAPS surface data (Figure 17) and PATMOS-x satellite data in Figure 32 show an anomalously high presence of optically thin, liquid clouds over the center of the Greenland ice sheet during the record melt event in July 2012. However, comparing the frequency and spatial extent of thin, liquid clouds over the Greenland ice sheet for July 2011 (Figure 31) and 2012 (Figure 32), we see that frequency of occurrence and spatial coverage of these clouds for non-melt years such as 2011 were quite similar to those in 2012, a record melt year. July 2011 had the highest frequency of occurrence of thin, liquid clouds over the central and eastern GIS, while such clouds in 2012 were more centralized with cluster of high frequency in the northern center of the GIS. There is a distinct lack of thin, liquid clouds along the shoreline of the GIS in both 2011 and 2012 as well. To explain the July 2012 melt event, another factor in addition to cloud cover amount must have influenced the surface temperature increase over the GIS to push the temperature above freezing.

### **3.3. Low Level Temperature Advection in 2011 and 2012**

To qualitatively evaluate the magnitude of large-scale circulation and specifically low-level warm air advection, ECMWF ERA-Interim reanalysis (Dee et al. 2011) plots of monthly means of temperature, geopotential height, and U and V wind components at four pressure levels were generated using the ECMWF ERA-Interim web interface ([http://data-portal.ecmwf.int/data/d/interim\\_full\\_mnth/levtype=pl/](http://data-portal.ecmwf.int/data/d/interim_full_mnth/levtype=pl/)). The ERA-Interim reanalysis was chosen because of its success when compared with other global reanalysis products in simulating near-surface surface meteorology in the high Arctic including temperature, pressure and winds (de Boer et al. 2014). From these reanalysis images generated, the effect of large-scale circulation on surface temperature over the Greenland Ice Sheet was inferred.

Figures 33 and 34 show the ECMWF reanalysis of temperature and geopotential height at 1000 hPa averaged over the month of July for 2011 and 2012, respectively. We see higher temperatures are further north along the west coast of the GIS (orange in 2012 versus yellow in 2011) in July 2012 when compared to 2011.

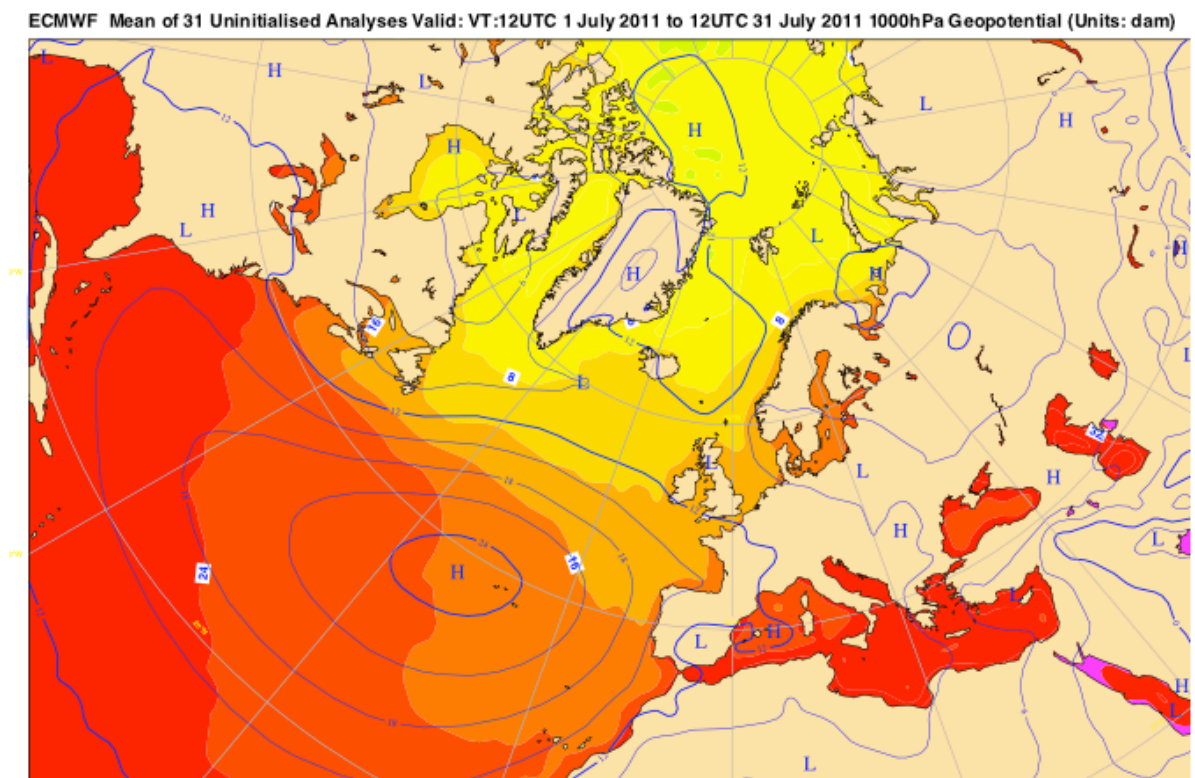


Figure 33: ECMWF reanalysis of Temperature (shaded) and Geopotential Height (blue contoured) at 1000 hPa averaged over the month of July 2011.

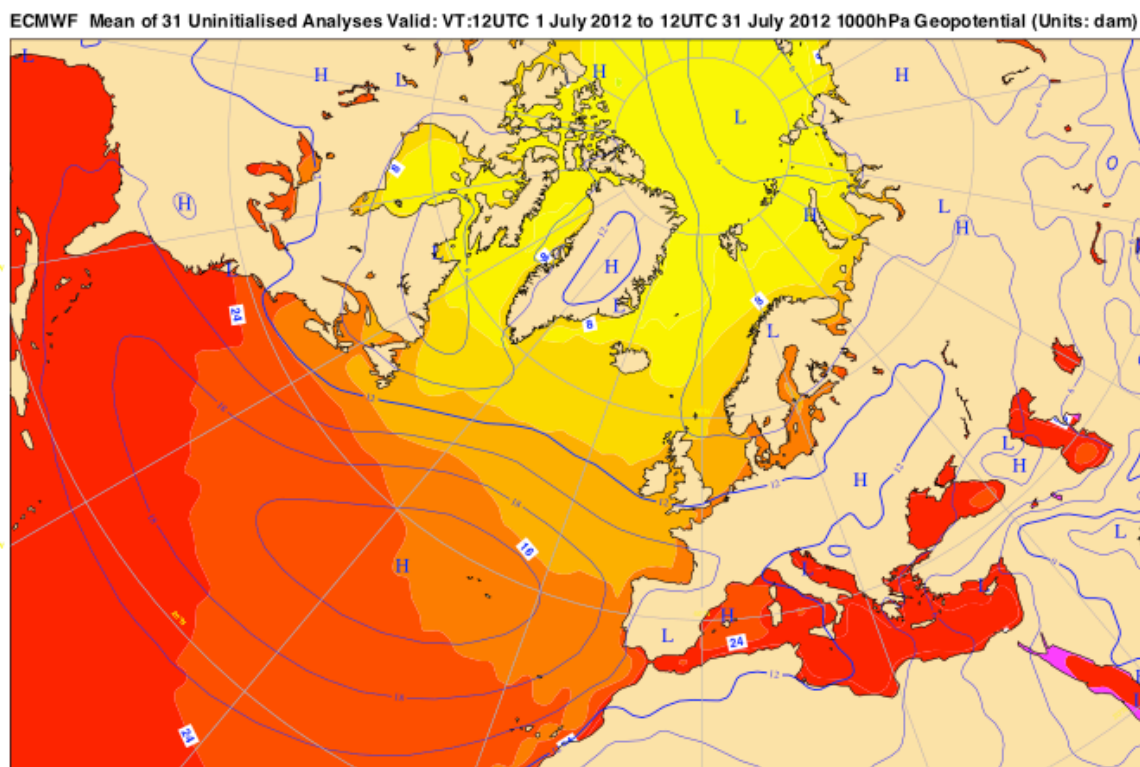


Figure 34: ECMWF reanalysis of Temperature (shaded) and Geopotential Height (blue contoured) at 1000 hPa averaged over the month of July 2012.

Figures 35 and 36 show the ECMWF reanalysis of temperature and geopotential height at 850 hPa averaged over the month of July for 2011 and 2012, respectively. As in the 1000 hPa analyses, higher temperatures are further north to the south and west of the GIS in July 2012 when compared to 2011. Combining these temperature and geopotential height analyses with plots of the u-component of the wind (Figures 37 and 38) at 850 hPa, with stronger offshore flow (yellow = westerly flow) on the east side of the GIS and stronger offshore flow on the west side of the GIS (greens = easterly flow) in 2011 than in 2012. The stronger offshore flow in July 2011, especially along the west coast of the GIS reduced the effect of low-level warm air advection on surface temperature as compared to 2012.

ECMWF Mean of 31 Uninitialised Analyses Valid: VT:12UTC 1 July 2011 to 12UTC 31 July 2011 850hPa Geopotential (Units: dam)

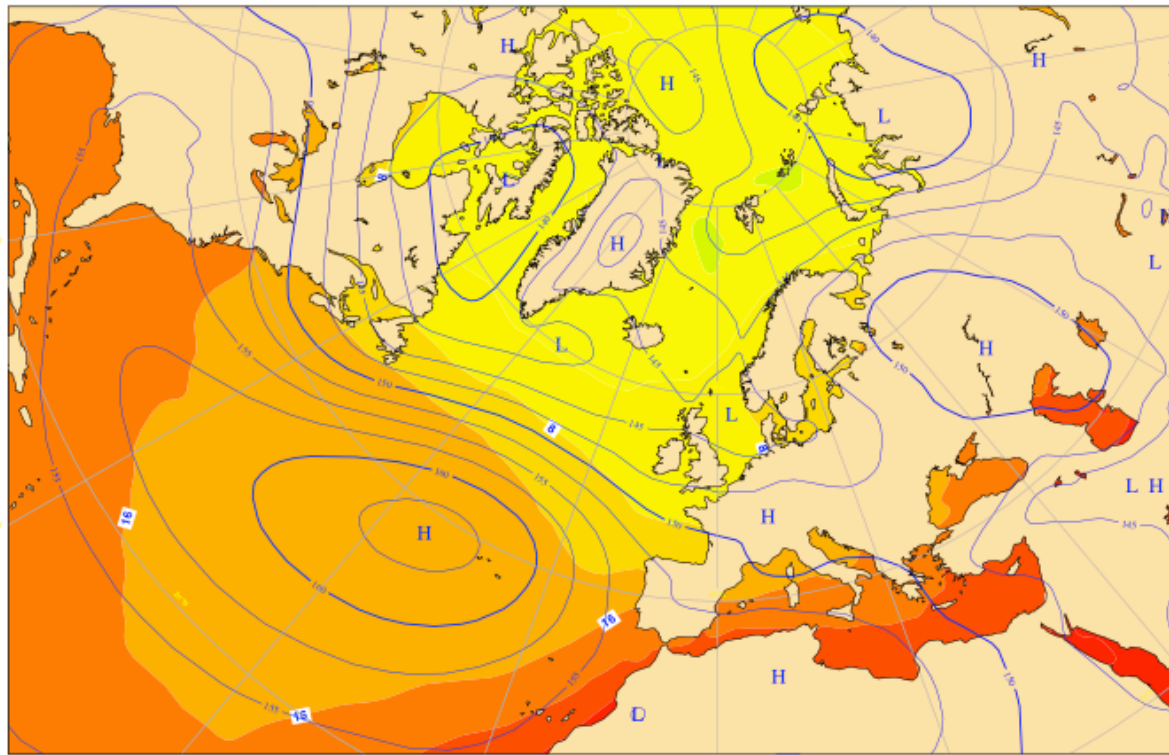


Figure 35: ECMWF reanalysis of Temperature (shaded) and Geopotential Height (blue contoured) at 850 hPa averaged over the month of July 2011.

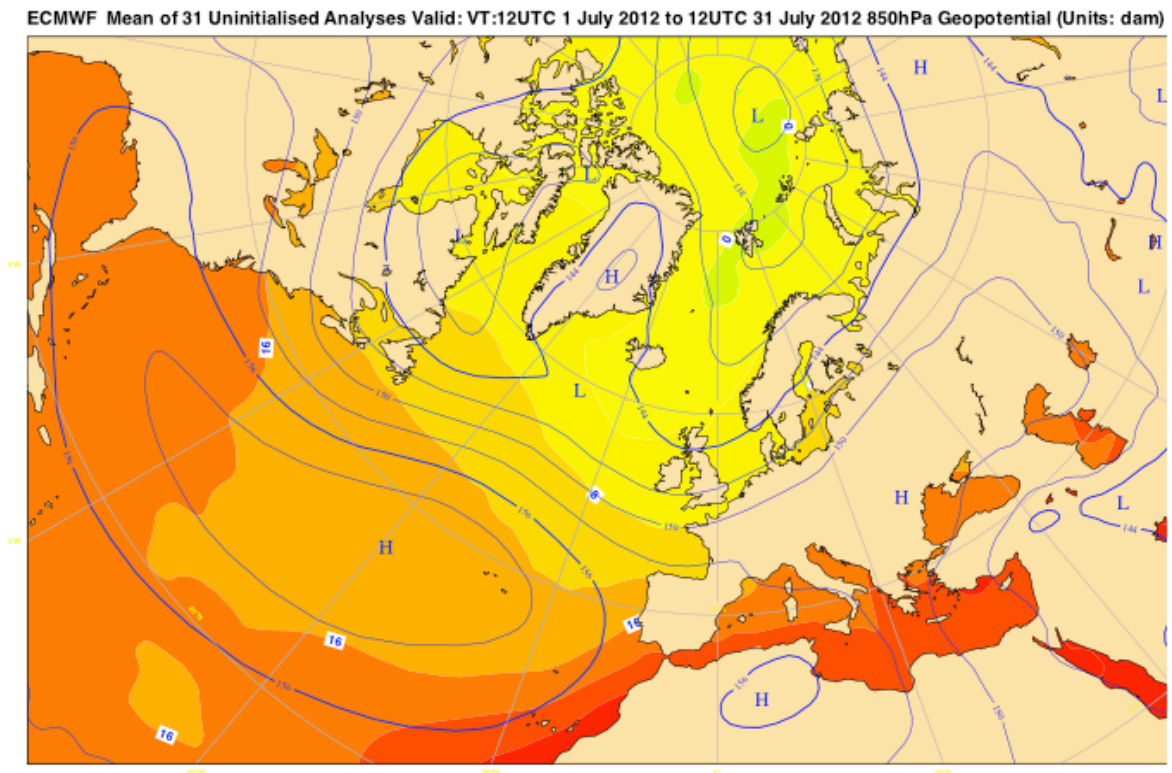


Figure 36: ECMWF reanalysis of Temperature (shaded) and Geopotential Height (blue contoured) at 850 hPa averaged over the month of July 2012.

ECMWF Mean of 31 Uninitialised Analyses Valid: VT:12UTC 1 July 2011 to 12UTC 31 July 2011 850hPa U velocity (Units: m/s)

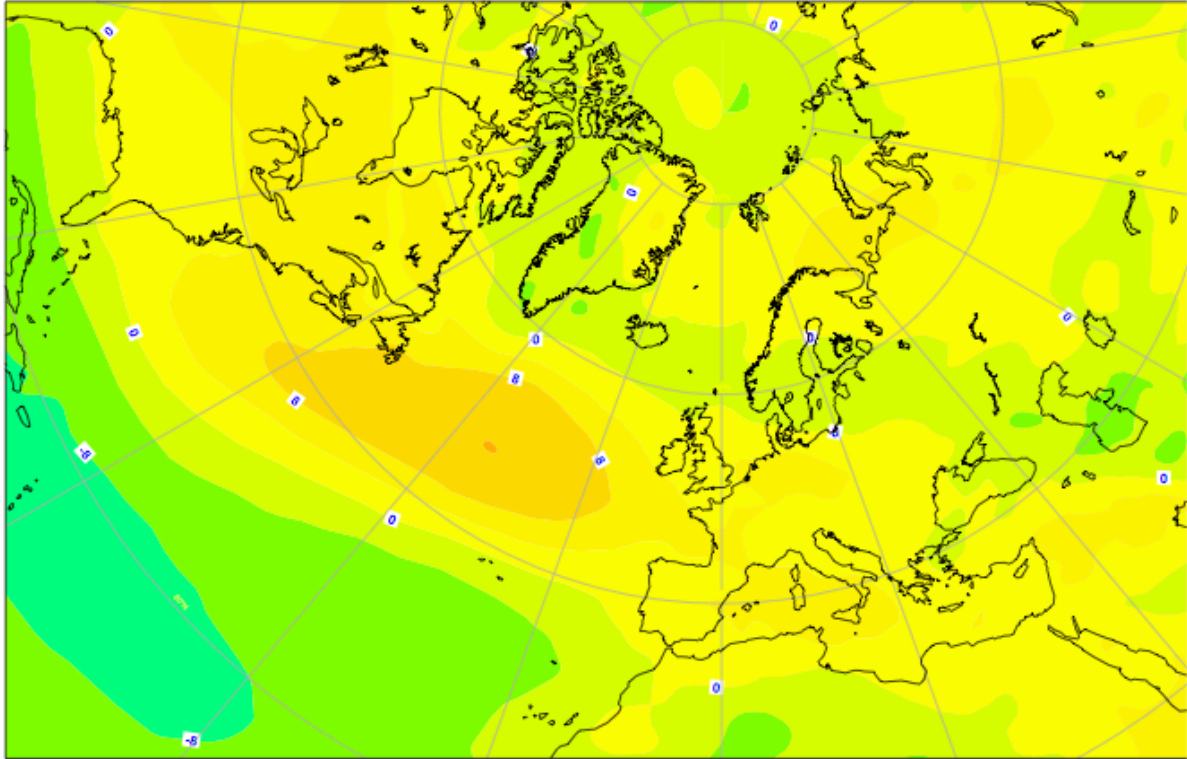


Figure 37: ECMWF reanalysis of the u wind component (shaded; warm colors are positive u, cool colors are negative u) at 850 hPa averaged over the month of July 2011.

ECMWF Mean of 31 Uninitialised Analyses Valid: VT:12UTC 1 July 2012 to 12UTC 31 July 2012 850hPa U velocity (Units: m/s)

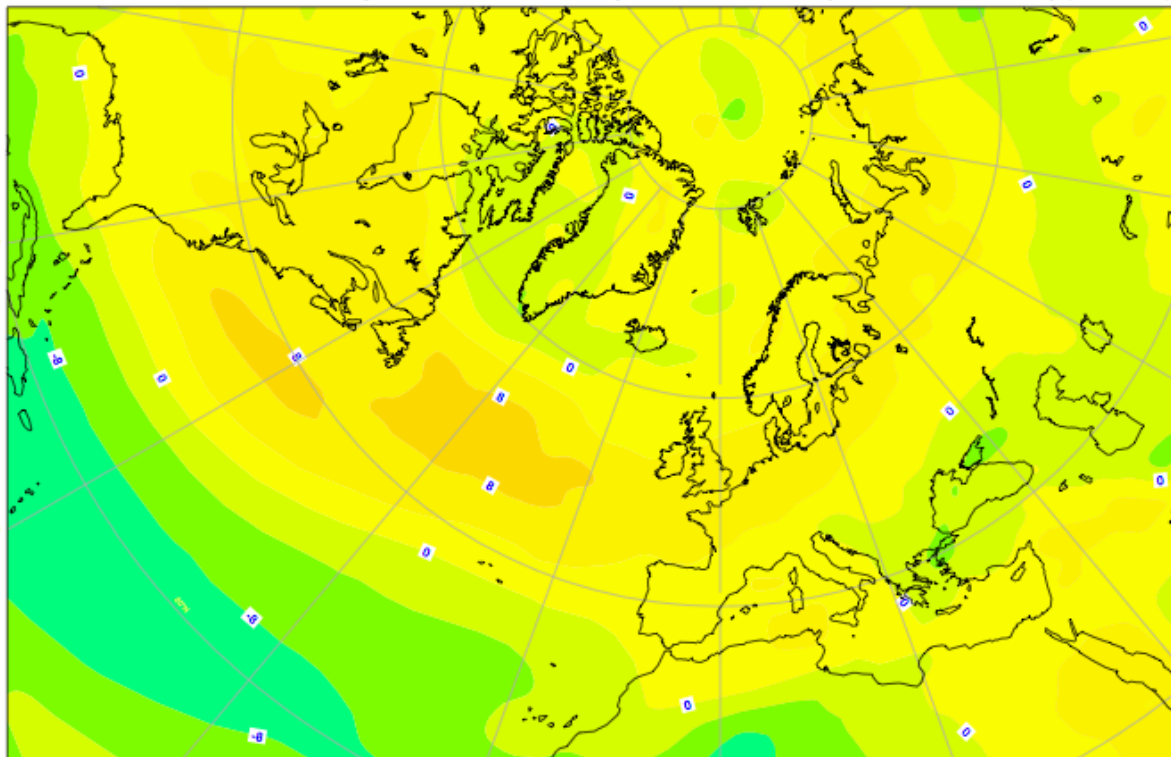


Figure 38: ECMWF reanalysis of the u wind component (shaded; warm colors are positive u, cool colors are negative u) at 850 hPa averaged over the month of July 2012.

Again combining temperature and geopotential height analyses (Figures 35 and 36) with plots of the v-component of the wind (Figures 39 and 40) at 850 hPa, there is stronger southerly flow (yellow = south-north flow) on the southwest side of the GIS in 2011 and stronger northerly flow on the east side (greens = north-south flow) in 2012. However, stronger offshore (east-west) flow along the west coast of the GIS in 2011 helped to reduce the onshore component of the stronger southerly flow in July 2011, especially along the south and west coasts. When collocated with a stronger 850 hPa high pressure over the GIS, these factors combined to limit the effectiveness of low-level warm air advection on surface temperature over the center of the GIS in 2011 as compared to 2012.

ECMWF Mean of 31 Uninitialised Analyses Valid: VT:12UTC 1 July 2011 to 12UTC 31 July 2011 850hPa V velocity (Units: m/s)

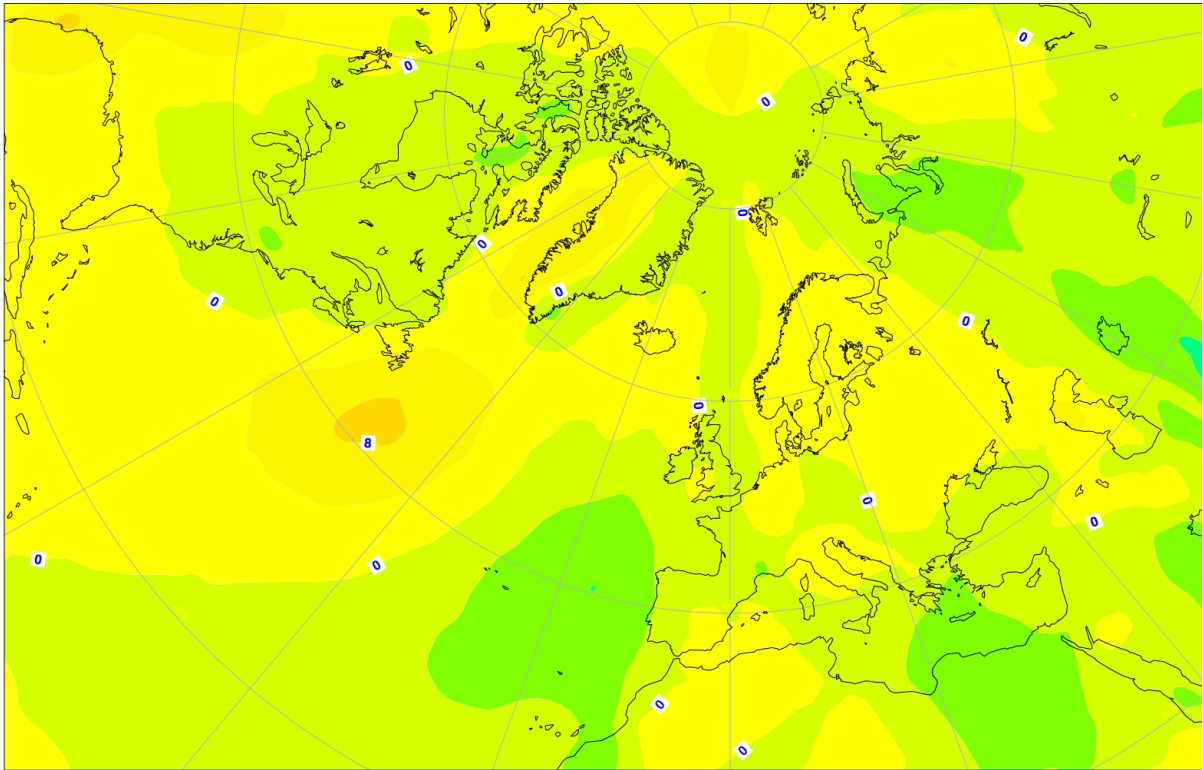


Figure 39: ECMWF reanalysis of the v wind component (shaded; warm colors are positive v, cool colors are negative v) at 850 hPa averaged over the month of July 2011.

ECMWF Mean of 31 Uninitialised Analyses Valid: VT:12UTC 1 July 2012 to 12UTC 31 July 2012 850hPa V velocity (Units: m/s)

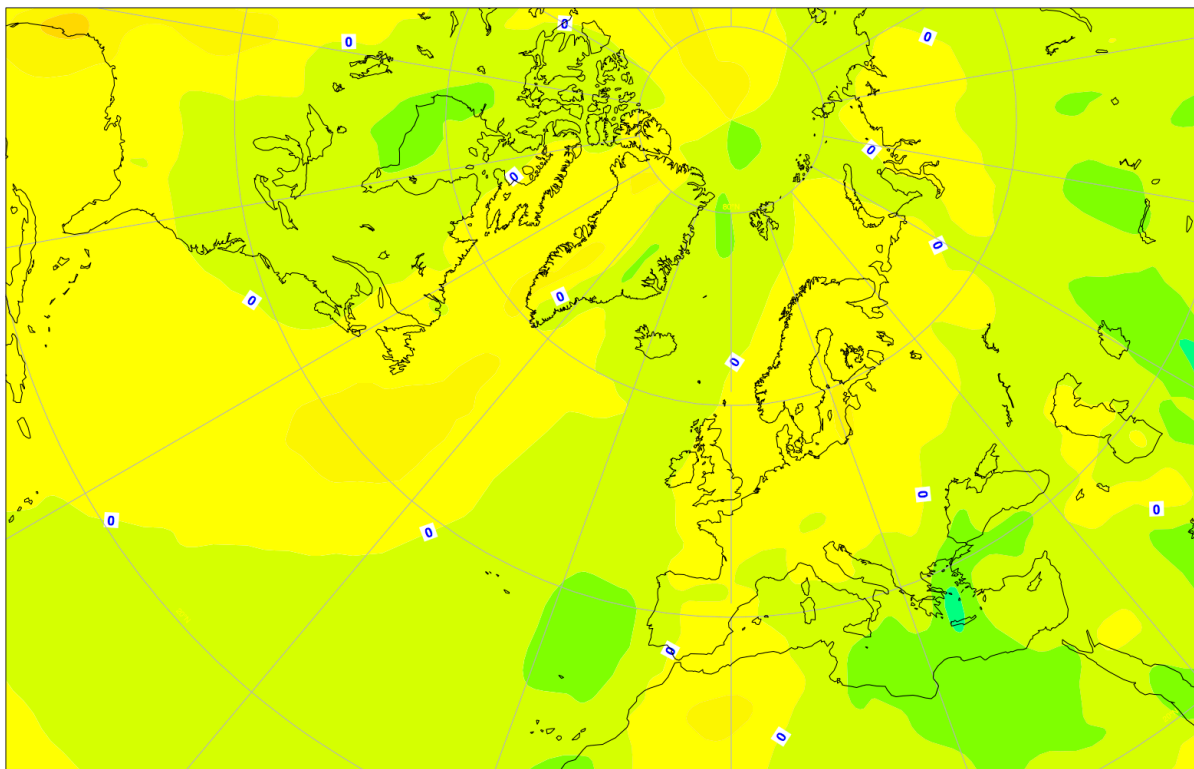


Figure 40: ECMWF reanalysis of the v wind component (shaded; warm colors are positive v, cool colors are negative v) at 850 hPa averaged over the month of July 2012.

#### 4. Summary and Conclusions

In July 2012, a new record for surface melt extent was set, with melting observed across almost the entire Greenland Ice Sheet (GIS). This alarming melt episode raised questions about the frequency and spatial extent of such events. How common are they? What are the contributing factors?

Here it was demonstrated that optically thin liquid clouds (LWP 10-40 g/m<sup>2</sup>), regardless of cloud base height, played a key role in the 2012 and 2011 melt events by increasing surface temperatures across the entire Greenland Ice Sheet (GIS). This study incorporated a radiative transfer model, remote sensing data from several satellite platforms and instruments, and climate reanalysis products. We extended the work of Bennartz et al. (2013) by expanding the study domain from a point observation in the center of the GIS to the entirety of Greenland by leveraging satellite data products.

We confirmed the findings of Bennartz et al. (2013) that showed that low-level, thin, liquid water clouds played a key role in the extended surface melting of the central GIS in July 2012. Radiative transfer modeling showed that these optically thin clouds warm the surface during the day for clouds of any base height between 0.5 and 3 km. This allowed the removal of the low-level constraint when identifying these optically thin, liquid clouds.

When using satellite sensors to identify such clouds, standard cloud products from the MODIS, CALIOP and IIR sensors did not provide reliable retrievals of optical depth over ice and snow. To sense optically thin liquid clouds over the GIS, the PATMOS-x product was employed along with a lookup table (LUT) to estimate cloud optical depth using only the 1.6  $\mu\text{m}$  channel. At 1.6  $\mu\text{m}$ , the underlying snow and ice surface on the GIS has a minimal

reflectance when compared to liquid clouds above it. This enabled a retrieval of cloud optical depth using an assumed particle radius of  $6.3 \mu\text{m}$ .

Cloud phase determination using standard satellite products was also problematic as the IR temperature of the clouds was often very similar to that of the snow and ice underneath. Cloud phase detection was achieved using the  $3.7 \mu\text{m}$  reflectance channel as a proxy. When combined with a LUT, comparing optical depths calculated using typical radii for liquid and ice clouds, a reflectance threshold of 0.07 was established as the  $3.7 \mu\text{m}$  reflectance boundary between ice and liquid cloud.

Frequency of occurrence and geospatial location of optically thin liquid clouds over the GIS was found to be nearly identical between July 2011 (Figure 31) and July 2012 (Figure 30). With observed melting over almost the entire GIS in July 2012 but not in 2011 (Nghiem 2012), warm air advection was likely the dominant contributor. This agrees with the findings of Bennartz et al. (2013) and Neff et al. (2014). In order to fully diagnose and explain the 2012 record melt event in terms of the many components and processes that affect surface temperature, the influence of warm air advection on the surface energy budget (and other factors) must be analyzed quantitatively.

## 5. Future Work

Results presented here may indirectly help to improve climate model simulations of Arctic cloud properties and surface energy budget, which are vital to fully account for temperature feedbacks in the warming Arctic regions. A first step in extending this work is to repeat this study over the Arctic Ocean to determine the role of thin, liquid clouds on the surface energy budget of sea ice. Additionally, expanding the time domain to the entire MODIS satellite record would be valuable in establishing a 15+ year climatology of location and frequency of occurrence of these optically thin liquid clouds in the Arctic. A second step would include direct comparisons of ICECAPS surface data and PATMOS-x satellite data for several months to determine the effectiveness of the PATMOS-x 1.6  $\mu\text{m}$  optical depth retrieval over the Greenland Ice Sheet year round.

While this study focused primarily on the surface radiative effects of single-layer liquid clouds, modeling of surface radiative effects of mixed phase and ice clouds would be helpful for quantifying their relative contributions to the surface energy budget. For example, it would be interesting to examine the sensitivity of cloud surface radiative forcing to the presence of ice clouds of various optical thicknesses, variations in surface emissivity due to snow and ice melting, and varying the cloud particle size and shape.

Neff et al (2013) suggests that for the 2012 record melt event, key factors in the summer melt episode were a combination of 1) Central North American drought and heat wave, 2) amplification of a polar trough-ridge pattern, 3) a positive excursion of the Atlantic Multi-Decadal Oscillation (AMO), and 4) advection of warm moist air northward along the west coast of Greenland and thence over the ice sheet as an elevated thin liquid cloud layer.

Further research may help quantify the contribution of each of these factors to the warming of the GIS above freezing in July 2012.

An analysis of daily meteorological data, advection and cloud properties over the Greenland Ice Sheet would be beneficial to address what conditions were present in the days preceding the July 11 melt event. This would include using atmospheric sounding data from Summit, Greenland in the radiative transfer modeling for a more accurate determination of daily cloud radiative forcing.

This study also highlights the dire need to improve satellite retrievals of cloud optical depth over highly reflective and cold surfaces such as snow and ice. Several satellite platforms with both active and passive sensors were shown to be inconsistent with one another when attempting to detect optically thin, liquid clouds over highly reflective and cold surfaces in polar regions.

## References

- Ackerman, S., K. Strabala, W. Menzel, R. Frey, C. Moeller, and L. Gumley (1998): Discriminating clear sky from clouds with MODIS, *J. Geophys. Res.*, 103(D24), 32,141–32,157, doi: 10.1029/1998JD200032.
- Ackerman, S., R. Holz, R. Frey, E. Eloranta, B. Maddux, and M. McGill (2008): Cloud detection with MODIS. Part II: Validation, *J. Atmos. Oceanic Technol.*, 25, 1073–1086, doi: 10.1175/2007JTECHA1053.1.
- Baum, B., W. Menzel, R. Frey, D. Tobin, R. Holz, S. Ackerman, A. Heidinger and P. Yang (2012): MODIS Cloud-Top Property Refinements for Collection 6. *J. Appl. Meteor. Climatol.*, **51**, 1145–1163. doi: 10.1175/JAMC-D-11-0203.1
- Bennartz, R. et al. (2013): July 2012 Greenland melt extent enhanced by low-level liquid clouds. *Nature* Vol. 496, 83-86, doi: 10.1038/nature12002.
- Berrisford P, D. Dee, K. Fielding, M. Fuentes, P. Kallberg, S. Kobayashi and S. Uppala (2009): The ERA-INTERIM archive. European Centre for Medium-range Weather Forecasting, Shinfield Park, Reading
- Bintanja, R. and M. van den Broeke. (1996): The influence of clouds on the radiation budget of ice and snow surfaces in Antarctica and Greenland in summer. *Int. J. Climatol.* 16, 1281–1296.
- Buis, A. and S. Cole (2012): Satellites see unprecedented Greenland Ice Sheet melt. (NASA/JPL press release, 24 July 2012), <http://www.jpl.nasa.gov/news/news.cfm?release=2012-217>

CALIPSO: The Cloud-Aerosol Lidar and Infrared Pathfinder Satellite Observations, January 10, 2013, Accessed May 6, 2014, <http://www-calipso.larc.nasa.gov/>

Cesana, G., J. E. Kay, H. Chepfer, J. M. English and G. de Boer (2012): Ubiquitous low-level liquid-containing Arctic clouds: new observations and climate model constraints from CALIPSO-GOCCP. *Geophys. Res. Lett.* **39**, L20804, <http://dx.doi.org/10.1029/2012GL053385>

Chan, M. and J. Comiso (2013): Arctic Cloud Characteristics as Derived from MODIS, CALIPSO, and CloudSat. *J. Climate*, **26**, 3285–3306. doi: 10.1175/JCLI-D-12-00204.1

de Boer, G., M. D. Shupe, P. M. Caldwell, S. E. Bauer, O. Persson, J. S. Boyle, M. Kelley, S. A. Klein, and M. Tjernström (2014): Near-surface meteorology during the Arctic Summer Cloud Ocean Study (ASCOS): evaluation of reanalyses and global climate models. *Atmos. Chem. Phys.*, **14**, 427-445, doi:10.5194/acp-14-427-2014.

Curry, J., J. Schramm, W. Rossow and D. Randall, 1996: Overview of Arctic Cloud and Radiation Characteristics. *J. Climate*, **9**, 1731–1764. doi: 10.1175/1520-0442(1996)009<1731:OOACAR>2.0.CO;2

Dee D., S. Uppala, A. Simmons, P. Berrisford, P. Poli, S. Kobayashi, U. Andrae, M. Balmaseda, G. Balsamo, P. Bauer, P. Bechtold, A. Beljaars, L. van de Berg, J. Bidlot, N. Bormann, C. Delsol, R. Dragani, M. Fuentes, A. Geer, L. Haimberger, S. Healy, H. Hersbach, E. Hólm, L. Isaksen, P. Kållberg, M. Köhler, M. Matricardi, A. McNally, B. Monge-Sanz, J. Morcrette, B. Park, C. Peubey, P. de Rosnay, C. Tavolato, J. Thépaut and F. Vitart (2011): The ERA-Interim reanalysis: configuration and performance of the data assimilation system. *Q. J. R. Meteorol. Soc.* **137**: 553 – 597. doi: 10.1002/qj.828.

- European Centre for Medium-range Weather Forecasting (2007): ERA-Interim: new ECMWF reanalysis products from 1989 onwards. *ECMWF Newsletter*, 110, 25–35.
- Frey, R., S. Ackerman, Y. Liu, K. Strabala, H. Zhang, J. Key and X. Wang (2008): Cloud detection with MODIS. Part I: Improvements in the MODIS cloud mask for Collection 5. *J. Atmos. Oceanic Technol.*, **25**, 1057–1072. doi: 10.1175/2008JTECHA1052.1
- Heidinger, A. et al. (2013): The Pathfinder Atmospheres Extended (PATMOS-X) AVHRR Climate Data Set. *BAMS*, doi: 10.1175/BAMS-D-12-00246.1 (in press).
- Holz, R., S. Ackerman, F. Nagle, R. Frey, S. Dutcher, R. Kuehn, M. Vaughan and B. Baum (2008): Global Moderate Resolution Imaging Spectroradiometer (MODIS) cloud detection and height evaluation using CALIOP. *J. Geophys. Res.* 113 D00A19
- Hu, Y., S. Rodier, K. Xu, W. Sun, J. Huang, B. Lin, P. Zhai, and D. Josset (2010): Occurrence, liquid water content, and fraction of supercooled water clouds from combined CALIOP/IIR/MODIS measurements. *J. Geophys. Res.*, **115**, D00H34, doi:10.1029/2009JD012384.
- Intrieri J., C. Fairall, M. Shupe, P. Persson, E. Andreas, P. Guest and R. Moritz (2002): An annual cycle of Arctic surface cloud forcing at SHEBA. *J. Geophys. Res.* 107 8039
- Josset, D., J. Pelon, A. Garnier, Y. Hu, M. Vaughan, P.-W. Zhai, R. Kuehn, and P. Lucker (2012): Cirrus optical depth and lidar ratio retrieval from combined CALIPSO-CloudSat observations using ocean surface echo. *J. Geophys. Res.*, **117**, D05207, doi:10.1029/2011JD016959
- Key, J. and A. Schweiger (1998): Tools for atmospheric radiative transfer: Streamer and FluxNet. *Computers and Geosciences*, 24(5), 443-451.

- Key, J. and J. Intrieri (2000): Cloud particle phase determination with the AVHRR. *J. Appl. Meteorol.*, 39(10), 1797-1805.
- Key, J. R. (2002): The cloud and surface parameter retrieval (CASPR) system for polar AVHRR. Cooperative institute for Meteorological Satellite Studies, University of Wisconsin-Madison, 59 pp. [Available online at <http://stratus.ssec.wisc.edu/caspr/documentation.html>]
- Liu, Y., S. Ackerman, B. Maddux, J. Key and R. Frey (2010): Errors in Cloud Detection over the Arctic Using a Satellite Imager and Implications for Observing Feedback Mechanisms. *J. Climate*, **23**, 1894-1907. doi: 10.1175/2009JCLI3386.1
- Liu, Y., J. Key, R. Frey, S. Ackerman and W. Menzel (2004): Nighttime polar cloud detection with MODIS. *Remote Sens. Environ.*, **92**, 181–194. doi: 10.1016/j.rse.2004.06.004
- Meier, W., G. Hovelsrud, B. van Oort, J. Key, K. Kovacs, C. Michel, C. Haas, M. Granskog, S. Gerland, D. Perovich, A. Makshtas, and J. Reist, (2014): Arctic sea ice in transformation: A review of recent observed changes and impacts on biology and human activity, *Rev. Geophys.*, 51, doi: 10.1002/2013RG000431.
- Neff, W. D. et al. (2013): Continental heat anomalies and the extreme melting of the Greenland ice surface in 2012 and 1889. *J. Geophys. Res. Atmospheres*. doi: 10.1002/2014JD021470 (in press).
- Nghiem, S. V. et al. (2012): The extreme melt across the Greenland Ice Sheet in 2012. *Geophys. Res. Lett.* **39**, L20502, doi: 10.1029/2012GL053611.

- Pavolonis, M. and J. Key. (2003): Antarctic cloud radiative forcing at the surface estimated from the AVHRR Polar Pathfinder and ISCCP D1 data sets, 1985-1993, *J. Appl. Meteorol.*, 42(6), 827-840.
- Platnick, S., M. King, S. Ackerman, W. Menzel, B. Baum, J. Riedi, and R. Frey (2003): The MODIS cloud products: algorithms and examples from Terra, *IEEE Transactions, Geoscience and Remote Sensing*, 41(2), 459-473, doi: 10.1109/TGRS.2002.808301
- Schweiger A and J. Key (1994): Arctic Ocean radiative fluxes and cloud forcing estimates from the ISCCP C2 cloud dataset *J. Appl. Meteorol.* 33, 948–63
- Shupe, M. D. et al. (2013): High and Dry: New Observations of Tropospheric and Cloud Properties above the Greenland Ice Sheet. *Bull. Amer. Meteor. Soc.*, 94, 169–186. doi: 10.1175/BAMS-D-11-00249.1
- Shupe, M. D. and J. Intrieri (2004): Cloud radiative forcing of the Arctic surface: the influence of cloud properties, surface albedo, and solar zenith angle. *J. Clim.* 17, 616–628.
- Simmons A. J., P. Poli, D. Dee, P. Berrisford, H. Hersbach, S. Kobayashi and C. Puebey (2014): Estimating low-frequency variability and trends in atmospheric temperature using ERA-Interim (Revised 2014). European Centre for Medium-range Weather Forecasting, Shinfield Park, Reading
- Stone, R.S. (1997): Variations in western Arctic temperature in response to cloud radiative and synoptic-scale influences, *J. Geophys. Res.*, 102(D18), 21769-21776.
- Turner D. D. et al. (2007): Thin liquid water clouds: Their importance and our challenge. *Bull. Amer. Meteor. Soc.*, 88, 177–190, doi: 10.1175/BAMS-88-2-177.

- Wang, X., J. R. Key (2005): Arctic Surface, Cloud, and Radiation Properties Based on the AVHRR Polar Pathfinder Dataset. Part I: Spatial and Temporal Characteristics. *J. Climate*, **18**, 2558–2574. doi: <http://dx.doi.org/10.1175/JCLI3438.1>
- Winker, D.M. et al. (2010): The CALIPSO Mission: A Global 3D View of Aerosols and Clouds. *BAMS*, 1211-1229, doi: 10.1175/2010BAMS3009.1.